Title

Photonic Integrated Circuits for Remote Sensing Lidar

Author

Fridlander, Joseph

Publication Date

2021

UNIVERSITY OF CALIFORNIA

Santa Barbara

Photonic Integrated Circuits for Remote Sensing Lidar

A dissertation submitted in partial satisfaction of the
requirements for the degree Doctor of Philosophy
in Electrical and Computer Engineering

by

Joseph Martin Fridlander

Committee in charge:
Professor Jonathan Klamkin, Chair
Professor Larry Coldren
Professor John Bowers
Dr. Mark Stephen

June 2021

The dissertation of Joseph Martin Fridlander is approved.

Larry Coldren

John Bowers

Mark Stephen

Jonathan Klamkin, Committee Chair

June 2021

Photonic Integrated Circuits for Remote Sensing Lidar

This dissertation is dedicated to my parents,

Aaron and Sofia Fridlander,

for their love and support

ACKNOWLEDGEMENTS

During my time at UCSB, I have had the tremendous benefit of working beside experts in the field of semiconductor lasers and integrated photonics. First, I would like to thank my adviser Prof. Jonathan Klamkin for offering me the opportunity to join iPL and his mentorship throughout my studies. Jonathan has successfully managed a large group that conducts research all across the photonics spectrum. I have learned so much during my time at iPL and UCSB, but I have not figured out how he manages all those projects. Photonics is such a broad and rich field and has the potential to transform technological capabilities in communication and sensing. I am grateful to have had the opportunity to research and develop photonic technologies and am excited about the future of this field.

I would also like to thank Prof. Larry Coldren for his valuable input and insight during group meetings and with lab experiments. I also spent many hours reading his textbook on laser diodes, which I liked to refer to as “the Bible”. His input was always consequential to our research and measurements. It was a pleasure to have him on the team.

I first met Prof. John Bowers in an optoelectronics class. His lectures were terrific, and he devised a final project that I enjoyed and was motivated to work on. The project covered many aspects of a complete fiber-optic communication network. I found my research project to be similar in nature. It was a real challenge to have all parts cohesively working together as a complete system, requiring knowledge in control theory, electronics, and photonics.

I have learned a great deal during my time at UCSB while working on a complex PIC lidar. For that, I must thank our NASA collaborators whose work was the inspiration behind our project, especially Dr. Mark Stephen who was regularly involved in technical discussions, provided terrific input, and helped obtain much of the necessary specialized equipment required for testing. I would also like to thank his colleagues Stephan Kawa, Jeffrey Chen and Kenji Numata who guided me through many technical details. They are all truly remarkable in their breadth and depth of knowledge in physics, optics, and photonics.

I am greatly thankful to my two closest collaborators on the IMPRESS project, my fellow PhD students, Victoria Rosborough and Fengqiao Sang. I learned a great deal from their own experiences, technical contributions, and great questions they posed. I was lucky to have had such hard-working team members on the project.

I also want to thank the rest of the iPL team. They are a very talented bunch. Their group updates were a glimpse into the breadth of work our team is involved in, ranging from device design, laser integration on silicon, and PICs. I learned so much from them, including material growth, fabrication, and photonic device design.

I want to thank the ECE administrative assistants and the shop staff who were always willing to help me out when the soldering was too challenging.

I'd like to also thank the cleanroom staff, who trained me on the tools and provided valuable input on processing for a very confused cleanroom newbie. At UCSB we not only design and test but also fabricate our devices. It requires a dedicated and knowledgeable staff to have the tools running smoothly.

Finally, I want to thank my parents, Aaron and Sofia, for their support throughout this rewarding, long, and challenging endeavor. I would also like to thank my sister Fania and her extended family, Jeff, Tsila, and Daniel, and of course the cutest bundle of joy that has brought us all so much happiness, my niece Julia.

VITA OF JOSEPH MARTIN FRIDALNDER

EDUCATION

2012	Bachelor of Science in Electrical and Computer Engineering, Cornell University, Ithaca, New York
2013	Master of Engineering, Electrical and Computer Engineering, Cornell University, Ithaca, New York.
2021	Doctor of Philosophy in Electronics and Photonics, University of California, Santa Barbara.

PROFESSIONAL EMPLOYMENT

2013-2016	RF Microwave Engineer, Jet Propulsion Laboratory, Pasadena, CA

AWARDS

2020	Herb Kroemer Dissertation Fellowship

PUBLICATIONS

1. J. Fridlander *et al.*, "Dual Laser Indium Phosphide Photonic Integrated Circuit for Integrated Path Differential Absorption Lidar," in *IEEE Journal of Selected Topics in Quantum Electronics*, vol. 28, no. 1, pp. 1-8, Jan.-Feb. 2022, Art no. 6100208, doi: 10.1109/JSTQE.2021.3091662.
2. P. A. Verrinder *et al.*, "Gallium Arsenide Photonic Integrated Circuit Platform for Tunable Laser Applications," in *IEEE Journal of Selected Topics in Quantum Electronics*, vol. 28, no. 1, pp. 1-9, Jan.-Feb. 2022, Art no. 6100109, doi: 10.1109/JSTQE.2021.3086074.
3. J. Fridlander, F. Sang, V. Rosborough, S. Brunelli, J. Chen, K. Numata, S. Kawa, M. Stephen, L. Coldren, J. Klamkin, “Monolithic Indium Phosphide Dual Laser Photonic Integrated Circuit for Remote Sensing Lidar,” in Conference on Lasers and Electro-Optics, OSA Technical Digest (Optical Society of America, 2021), paper JTu3A.89.
4. J. Fridlander, V. Rosborough, F. Sang, M. Nickerson, J. Chen, K. Numata, P. Verrinder, F. Gambini, S. Pinna, S. Kawa, M. Stephen, L. Coldren, and J. Klamkin, "Photonic Integrated Circuits for Precision Spectroscopy," in Conference on Lasers and Electro-Optics, OSA Technical Digest (Optical Society of America, 2020), paper SF3O.3.
5. V. Rosborough, F. Sang, J. Fridlander, H. Zhao, B. Song, S. T. Š. Brunelli, J. R. Chen, M. A. Stephen, L. Coldren, and J. Klamkin, "Monolithic Integration of

Widely-Tunable DBR and DFB Lasers with One-Step Grating Formation," in *OSA Advanced Photonics Congress (AP) 2019 (IPR, Networks, NOMA, SPPCom, PVLED)*, OSA Technical Digest (Optical Society of America, 2019), paper IM2A.5.

6. M. Stephen *et al*., "Integrated Micro-Photonics for Remote Earth Science Sensing (Impress) Lidar," *IGARSS 2019 - 2019 IEEE International Geoscience and Remote Sensing Symposium*, Yokohama, Japan, 2019, pp. 4853-4856, doi: 10.1109/IGARSS.2019.8899145.
7. Joseph Fridlander, *et al*, "High-speed RZ-DPSK photonic integrated transmitter for space optical communications," Proc. SPIE 11133, Laser Communication and Propagation through the Atmosphere and Oceans VIII, 1113309 (6 September 2019)
8. Joseph Fridlander, *et al*, "Photonic integrated transmitter for space optical communications," Proc. SPIE 10910, Free-Space Laser Communications XXXI, 1091026 (20 March 2019).
9. Joseph Fridlander, *et al*, "RZ-DPSK photonic integrated transmitter for space optical communications," Proc. SPIE 10524, Free-Space Laser Communication and Atmospheric Propagation XXX, 105240Y (15 February 2018);
10. J. Fridlander, *et al*, "Direct Pulse Position Modulation of a 410 nm Semipolar GaN Laser Diode for Space Optical Communications," in Conference on Lasers and Electro-Optics, OSA Technical Digest (online) (Optical Society of America, 2018), paper STu4Q.3.

ABSTRACT

Photonic Integrated Circuits for Remote Sensing Lidar

by

Joseph Martin Fridlander

To quantify and model current and future atmospheric compositions and to better understand tropospheric carbon dioxide (CO_2) exchange with the land and oceans, accurate and precise measurements are required. Active sensing of CO_2 can be accomplished with light detection and ranging (lidar). Unlike passive spectrometers that rely on sunlight, an active lidar provides significantly better wavelength and spatial resolution and can perform sensing continuously during the day, night, and over the ocean.

Lidar instruments are extremely complex optical systems, costly, bulky, and power hungry. Photonic integrated circuits (PICs) on the other hand allow integration of all the required optical functions of a lidar on a single chip. Furthermore, a variety of integration platforms, materials, and devices exist that allow a high degree of flexibility to meet the required stringent specifications.

In this work, an integrated path differential absorption lidar seed laser PIC is designed for active sensing of CO_2. All optical functions, with exception of a gas cell reference, are integrated onto a chip approximately 10 mm^2. First, using an integrated phase modulator, a master widely tunable SG-DBR laser is stabilized to a gas cell reference using a frequency

modulation technique. Using an optical phase locked loop, a slave laser is locked to the master laser and stepped across multiple sampling points to map a CO_2 absorption line at 1572 nm at offsets up to ±15 GHz. Before processing by the optical phase locked loop, the offset frequency between the lasers is detected with an on-chip high-speed photodiode in the form of a beat note. Finally, a pulse carver generates high extinction ratio pulses for transmission.

Using this PIC, we demonstrated a factor of 235 improvement in the master laser frequency stability over a 1-hr period using 1-second gate times. We also demonstrated slave laser locking to the master laser at offsets up to ±15 GHz, albeit we relied on an off-chip detector. Also demonstrated were pulses with more than 40 dB extinction ratio. Finally, we successfully demonstrated continuous wave sensing of the 1572 nm CO_2 absorption line. The work illustrated here shows that PICs are a very promising technology for earth science and sensing lidar at significantly reduced cost, size, weight, and power.

TABLE OF CONTENTS

Chapter 1. Introduction

1.1 Trace Gas Monitoring: Carbon Dioxide

I don't want to alarm anyone but severe consequences of rapid climate change due to human activity include global rise in surface temperatures, warming oceans, shrinking ice sheets, glacial retreat, sea level rise, extreme events, and ocean acidification [1].

Greenhouse gases such as carbon dioxide (CO_2) trap heat near the surface of the earth resulting in increased surface temperatures. CO_2 concentration levels have risen by as much as 48% since the pre-industrial age level found in 1850 [2]. Various carbon sinks such as the oceans and plants absorb carbon and help reduce the amount of CO_2 in the atmosphere. Plants, for example, absorb CO_2 during the process of photosynthesis to make food. Furthermore, elevated concentrations of CO_2 cause an increase in photosynthesis and plant growth. This is referred to as the CO_2 fertilization effect and helps mitigate the effects of climate change. Studies nevertheless show that terrestrial ecosystems are becoming less reliable [3,4].

To quantify and model current and future atmospheric compositions and to better understand tropospheric CO_2 exchange with the land and oceans, accurate and precise measurements are required. Subsequent scientific studies will inform on policies regarding emissions and renewable energy and help better understand near and long-term climate change impacts on our societies.

Currently satellites such as the Greenhouse Gas Observing Satellite (GOSAT) and the Orbiting Carbon Observatory–2 (OCO-2) measure the total column absorption of CO_2 in sunlight reflected from Earth's surface [5]. However, measurements from passive spectrometers have several drawbacks; the sun angle limits measurement to daytime primarily over mid-latitudes while scattering from thin clouds modifies the optical path length and the total CO_2 absorption measured and hence can limit the accuracy.

To address these limitations, the US National Research Council's Decadal Survey for Earth Science recommended a space-based mission to provide global atmospheric CO_2 measurements with much smaller seasonal, latitudinal, and diurnal biases by using the laser absorption spectroscopy measurement approach. The mission's goals are to quantify global spatial distribution of atmospheric CO_2 with 1–2 ppm accuracy and quantify the global spatial distribution of terrestrial and oceanic sources and sinks of CO_2 on 1-degree grids with 2 or 3-week time resolution [6].

To meet these requirements, a candidate integrated path differential absorption (IPDA) lidar was developed at NASA Goddard [7].

1.2 LIDAR

Light detection and ranging (lidar) systems use light for remote sensing. There are several lidar types, some of which will be described [8]. Direct detection lidars, which rely on the time of flight of a pulse, are used for range finding and topographic mapping. By making use of both spatial and temporal coherence properties of light, lidar detection can provide both range and velocity information. Applications of coherent lidars include environmental wind sensing, as well as self-driving cars, and gaming.

Integrated path differential absorption (IPDA) lidars are commonly used for absorption spectroscopy. The lidar instrument relies on a laser with linewidth significantly narrower than the absorption line. The path integrated gas absorption ratio of an on-line and off-line pulsed laser is then used to determine column integrated or range resolved concentrations. IPDA lidar scattering targets include surfaces such as the ground, ocean, and clouds. Cloud slicing can be used to determine the range resolved CO_2 concentrations between the source and clouds as well as the clouds and ground [9,10]. Because CO_2 has diurnal vertical transport, the absorption line can be sampled at the sides of the line where the absorption is due to pressure broadened CO_2 molecules. This helps maintain uniform measurement sensitivity in the lower troposphere. Furthermore, atmospheric weighting functions can be calculated at two to three heights by sampling the absorption line at the sides of the line [6]. Finally, instrument wavelength offsets can also be solved for by using a line fitting process. Key parameters for a CO_2 spaceborne IPDA lidar are illustrated in Tab. 1-1 [6].

CO_2 line center wavelength	1572.335 nm
Laser wavelength steps across the line	~ 10-20
Laser min and max wavelengths	1572.29, 1572.39
Wavelength change / step	~ 5-10 pm
Laser peak power, pulse width	2.5 kW, 1 μsec
Pulse energy	2.5 mJ
Laser linewidth	< 15 MHz
Scan rate	~ 1 msec

Table 1-1 Key parameters of a spaceborne IPDA lidar.

1.3 Photonic Integrated Circuits for Lidar

Highly coherent sources have many useful applications, including spectroscopy, optical communications, frequency metrology, and lidar. Initially, coherent frequency synthesis systems relied on narrow linewidth lasers and were constructed in the lab [11]. Large path delays limited optical phase locked loop (OPLL) performances but were sufficient due to the narrow linewidth of the laser. These efforts utilized narrow linewidth gas and solid-state lasers.

Semiconductor lasers are an attractive technology for coherent frequency systems but suffer from linewidths that may be a few megahertz broad. Consequently, significantly reduced path delays to accommodate high loop bandwidths were required. Such laser diode-based systems were not possible using bulk optics without introducing line narrowing techniques such as external cavities [12]. Results improved further with the introduction of micro-optics.

The availability of photonic integration then allowed placement of photonic and electronic functions beside the laser which reduced delays to sub-nanosecond. Consequently, highly coherent systems with loop bandwidths hundreds of megahertz wide were demonstrated [13,14]. For example, in [15], an indium phosphide monolithic photonic integrated circuit (PIC) with dual integrated SG-DBR lasers, semiconductor optical amplifiers, modulators, and photodetectors with 300 MHz loop bandwidth was demonstrated for coherent amplitude and phase modulated carrier generation, limited by the bandwidth of the detecting medium and modulation speed limited by on-chip modulator bandwidths. In [16], the integrated linewidth of a tunable SG-DBR laser was reduced from 19 MHz to 570 kHz using negative feedback from a Mach-Zehnder frequency discriminator integrated on the same chip. The frequency noise PSD was suppressed to approximately $2 * 10^{15}\ Hz^2/Hz$ with a loop bandwidth of 630 MHz.

Integrated coherent frequency synthesis demonstrations thus far have not focused on the accuracy of the laser wavelengths but rather the relative stability between a master and slave laser. Semiconductor lasers can have thermal tuning sensitivities of 0.1 nm / °C and so require thermal control, but this is insufficient for active sensing lidars for trace gas monitoring that require both accuracy and precision for characterization of gas absorption lines. Thus, frequency locking of lasers to integrated references such as asymmetric Mach-Zehnder modulators are not sufficient [17]. Instead, athermal frequency discriminator cavities in TiO_2 [18] or integrated gas cells and atomic cladding waveguides [19,20] may be more appropriate.

1.4 Preview of Dissertation

To quantify and model current and future atmospheric compositions and to better understand tropospheric CO_2 exchange with the land and oceans, accurate and precise measurements are required. Active sensing of CO_2 can be accomplished with lidar. Unlike passive spectrometers that rely on sunlight, an active lidar provides significantly better wavelength and spatial resolution and can perform sensing during the day, night, and over the ocean.

Lidar instruments are extremely complex optical systems, costly, bulky, and power hungry. Photonic integrated circuits on the other hand allow integration of all the required optical functions of a lidar on a single chip. Furthermore, a variety of integration platforms, materials, and devices exist that allow a high degree of flexibility to meet the required stringent specifications.

In this work an integrated path differential absorption (IPDA) lidar seed laser PIC is designed for active sensing of CO_2. All optical functions, with exception to a gas cell reference, are integrated onto a PIC approximately 10 mm^2. First, using an integrated phase modulator, a master widely tunable SG-DBR laser is stabilized to a gas cell reference using a frequency modulation technique. A factor of 235 improvement in the master laser frequency stability over a 1-hr period using 1-second gate times was demonstrated. Using an OPLL, a slave laser is stepped across multiple sampling points along a CO_2 absorption line at 1572 nm at offsets up to ±15 GHz. Before being processed by the OPLL, the offset frequency is detected with an on-chip high-speed photodiode in the form of a beat note. Finally, a pulse carver generates high extinction ratio pulses for transmission.

In this dissertation, we first discuss in Ch. 2, laser diode wavelength stabilization using frequency modulation techniques and dual laser locking using optical phase locked loops, including calculations. Ch. 3 covers PIC fabrication using the offset quantum well integration platform. Ch. 4 covers individual device performances and the relevance to overall system performance. Ch. 5 and 6 cover the subsystems and overall system operation of the IPDA PIC, including the stability of the lasers, offset frequency locking, and CO_2 sensing measurements. Comparison to the NASA IPDA lidar constructed using L-band telecom components will also be discussed. Ch. 7 will summarize this work's accomplishments, discuss PIC measurement challenges in the lab and how to improve testing, and look forward to future opportunities that can build on the work demonstrated here.

While much work has been done to demonstrate the lidar technology on a PIC, much work still remains. Furthermore, unanswered questions must be addressed. The laser stability was an order of magnitude worse that the lidar developed at NASA. Pulse generation perturbed the frequency stability of the lasers. Switching speeds in the lab was not fast enough to meet specifications either. To meet specifications for deployment in miniature satellite platforms, these issues must be investigated and resolved. Where appropriate, these issues are brought up and an attempt to explain them is made. Remedies and improvements are also provided.

References

1. USGCRP, 2017: *Climate Science Special Report: Fourth National Climate Assessment, Volume I* [Wuebbles, D.J., D.W. Fahey, K.A. Hibbard, D.J. Dokken, B.C. Stewart, and T.K. Maycock (eds.)]. U.S. Global Change Research Program, Washington, DC, USA, 470 pp, doi: 10.7930/J0J964J6.
2. NASA. (2021, February 19). Carbon Dioxide Concentration. NASA. https://climate.nasa.gov/vital-signs/carbon-dioxide/.
3. Ballantyne, A., Alden, C., Miller, J. *et al.* Increase in observed net carbon dioxide uptake by land and oceans during the past 50 years. *Nature* 488, 70–72 (2012). https://doi.org/10.1038/nature11299
4. Wang, S., Zhang, Y., Ju, W., Chen, J. M., Ciais, P., Cescatti, A., Sardans, J., Janssens, I. A., Wu, M., Berry, J. A., Campbell, E., Fernández-Martínez, M., Alkama, R., Sitch, S., Friedlingstein, P., Smith, W. K., Yuan, W., He, W., Lombardozzi, D., Peñuelas, J. (2020). Recent global decline of CO2 fertilization effects on vegetation photosynthesis. *Science*, *370*(6522), 1295–1300. https://doi.org/10.1126/science.abb7772
5. Eldering, A., Wennberg, P. O., Crisp, D., Schimel, D. S., Gunson, M. R., Chatterjee, A., Liu, J., Schwandner, F. M., Sun, Y., O'Dell, C. W., Frankenberg, C., Taylor, T., Fisher, B., Osterman, G. B., Wunch, D., Hakkarainen, J., Tamminen, J., & Weir, B. (2017). The Orbiting Carbon Observatory-2 early science investigations of regional carbon dioxide fluxes. *Science*, *358*(6360). https://doi.org/10.1126/science.aam5745
6. Abshire, J. B., Riris, H., Allan, G. R., Weaver, C. J., Mao, J., Sun, X., Hasselbrack, W. E., Kawa, S. R., & Biraud, S. (2010). Pulsed airborne lidar measurements of atmospheric CO2 column absorption. *Tellus, Series B: Chemical and Physical Meteorology*, *62*(5), 770–783. https://doi.org/10.1111/j.1600-0889.2010.00502.x
7. Numata, K., Chen, J. R., Wu, S. T., Abshire, J. B., & Krainak, M. A. (2011). Frequency stabilization of distributed-feedback laser diodes at 1572 nm for lidar measurements of atmospheric carbon dioxide. *Applied Optics*, *50*(7), 1047–1056. https://doi.org/10.1364/AO.50.001047
8. Molebny, V., McManamon, P., Steinvall, O., Kobayashi, T., & Chen, W. (2016). Laser radar: historical prospective—from the East to the West. *Optical Engineering*, *56*(3), 031220. https://doi.org/10.1117/1.oe.56.3.031220
9. Mao, J., Ramanathan, A., Abshire, J. B., Kawa, S. R., Riris, H., Allan, G. R., Rodriguez, M., Hasselbrack, W. E., Sun, X., Numata, K., Chen, J., Choi, Y., & Ying Melissa Yang, M. (2018). Measurement of atmospheric CO2 column concentrations to cloud tops with a pulsed multi-wavelength airborne lidar. *Atmospheric Measurement Techniques*, *11*(1), 127–140. https://doi.org/10.5194/amt-11-127-2018
10. Ramanathan, A. K., Mao, J., Abshire, J. B., & Allan, G. R. (2015). Remote sensing measurements of the CO2 mixing ratio in the planetary boundary layer using cloud

slicing with airborne lidar. *Geophysical Research Letters*, *42*(6), 2055–2062. https://doi.org/10.1002/2014GL062749

11. Enloe, L. H., & Rodda, J. L. (1965). *Laser phase-locked loop*. *50*, 23–25.
12. N. Satyan, W. Liang, A. Kewitsch, G. Rakuljic and A. Yariv, "Coherent Power Combination of Semiconductor Lasers Using Optical Phase-Lock Loops," in *IEEE Journal of Selected Topics in Quantum Electronics*, vol. 15, no. 2, pp. 240-247, March-april 2009, doi: 10.1109/JSTQE.2008.2011490.
13. K. Balakier, L. Ponnampalam, M. J. Fice, C. C. Renaud and A. J. Seeds, "Integrated Semiconductor Laser Optical Phase Lock Loops," in *IEEE Journal of Selected Topics in Quantum Electronics*, vol. 24, no. 1, pp. 1-12, Jan.-Feb. 2018, Art no. 1500112, doi: 10.1109/JSTQE.2017.2711581.
14. S. Ristic, A. Bhardwaj, M. J. Rodwell, L. A. Coldren and L. A. Johansson, "An Optical Phase-Locked Loop Photonic Integrated Circuit," in *Journal of Lightwave Technology*, vol. 28, no. 4, pp. 526-538, Feb.15, 2010, doi: 10.1109/JLT.2009.2030341.
15. Ristic, S., Bhardwaj, A., Rodwell, M. J., Coldren, L. A., & Johansson, L. A. (2009). *Integrated Optical Phase-Locked Loop*. 2–4.
16. A. Sivananthan *et al*., "Integrated linewidth reduction of a tunable SG-DBR laser," *CLEO: 2013*, 2013, pp. 1-2, doi: 10.1364/CLEO_SI.2013.CTu1L.2.
17. Idjadi, M. H., & Aflatouni, F. (2017). Integrated Pound-Drever-Hall laser stabilization system in silicon. *Nature Communications*, *8*(1), 1–9. https://doi.org/10.1038/s41467-017-01303-y
18. Magden, E. S., Peng, M. Y., Bradley, J. D. B., Leake, G., Coolbaugh, D. D., Kolodziejski, L. A., Kartner, F. X., & Watts, M. R. (2016). Laser frequency stabilization using pound-drever-hall technique with an integrated TiO2 athermal resonator. *2016 Conference on Lasers and Electro-Optics, CLEO 2016*, 20–21. https://doi.org/10.1364/cleo_si.2016.stu1h.3
19. Hänsel, A., & Heck, M. J. R. (2020). Opportunities for photonic integrated circuits in optical gas sensors. *JPhys Photonics*, *2*(1). https://doi.org/10.1088/2515-7647/ab6742
20. Popa, D., & Udrea, F. (2019). Towards integrated mid-infrared gas sensors. *Sensors (Switzerland)*, *19*(9), 1–15. https://doi.org/10.3390/s19092076

Chapter 2. Optical Frequency Stabilization

2.1 Laser Power and Frequency Characterization

2.1.1 Linewidth, Frequency Noise, and Relative Intensity Noise

Linewidth is a measure of the spectral width of a laser. SG-DBR lasers such as those used in this work have linewidths typically around a few megahertz. Recent works have demonstrated that using external ring resonators, semiconductor-based laser linewidths can be lowered to 10’s of kHz [1] or even sub-Hz using stimulated Brillouin scattering [2]. The modified Schawlow-Townes linewidth of a laser can be described according to Eq. 2.1,

$$\Delta\nu = \frac{\Gamma R'_{sp}}{4\pi N_p} \tag{2.1}$$

where Γ is the optical confinement factor, R'_{sp} is the spontaneous emission rate into an optical mode, and N_p is the photon density [3]. The Schawlow-Townes linewidth of a laser considers only spontaneous emission noise and as such is only a fundamental lower limit. To account for other sources of noise we rely on Eq. 2.2, where α is an enhancement factor typically about 2 to 6 [4-6].

$$\Delta\nu = \frac{\Gamma R'_{sp}}{4\pi N_p}(1+\alpha^2) \tag{2.2}$$

The enhancement factor accounts for the carrier noises in the laser. Because the refractive index in the laser depends on the carrier density, there is coupling between the gain intensity and phase noises. This results in a broadening of the laser linewidth given by the enhancement factor.

Fig. 2.1 shows the test setup for the SG-DBR self-heterodyne linewidth measurement technique. To improve measurement sensitivity, a 107 MHz optical frequency shifter is used. Because of their relatively broad linewidth, fairly short interferometer delay mismatches in the arms can be used (~ 1 km) to ensure incoherence of the interferometer paths. For long path delays, flicker noise sources in the laser will impact the measurement and will result in broadening of the laser linewidth [7]. In this setup, a 25 km fiber spool available in the lab was used to obtain the path mismatch. It is also important to use an isolator after the laser as the linewidth can be affected by the optical feedback into the laser. Typical SG-DBR linewidths are reported to be 1-10 MHz.

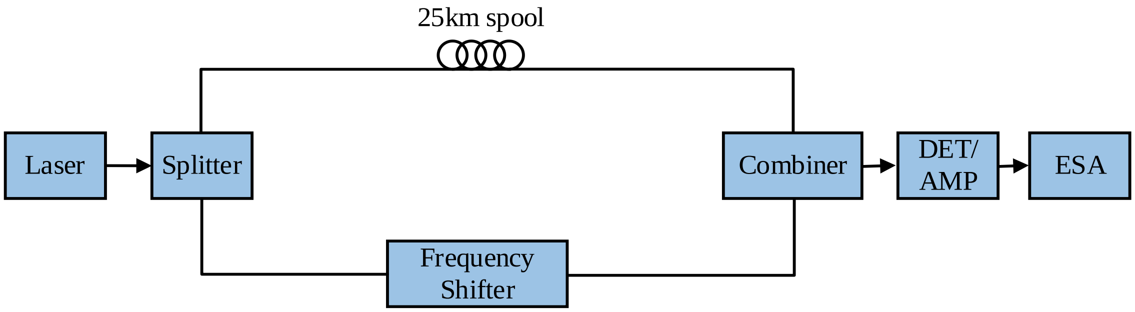

Figure 2.1 SG-DBR laser linewidth measurement.

The frequency noise of a laser can be approximated by introducing Langevin noise sources for the carrier and photon densities into the respective differential rate equations. The rate equations themselves yield an expression for the laser frequency shift as a function of change in the carrier density. If a Langevin phase noise source is introduced into this equation as well, the frequency noise of a laser diode can be expressed in Eq. 2.3.

$$S_{\nu}(\omega) = \frac{1}{2\pi}(\Delta\nu)_{ST}(1 + \alpha^2|H(\omega)|^2) \tag{2.3}$$

The modulation transfer function $|H(\omega)|$ has the form of a second order low pass filter. Its behavior is shaped by the laser resonance frequency ω_R and damping factor γ which together determine the carrier and photon steady state settling times. We can conclude from 2.3 that at high frequencies, beyond the relaxation resonance frequency of the laser, the frequency noise is dominated by a background flat component due to spontaneous emission phase noise. At lower frequencies, the frequency noise is determined by carrier noise that is shaped by the modulation transfer function [8].

To obtain a more complete picture of the laser frequency noise, measurement is required. Fig. 2.2 illustrates the setup for this. A Mach-Zehnder interferometer (MZI) is biased at the quadrature point corresponding to the laser emission frequency. The quadrature controller maintains the MZI at quadrature, where frequency fluctuations in the laser are approximately proportionally converted to amplitude fluctuations. A narrower free spectral range (FSR) can generate a greater frequency-to-amplitude conversion signal. The amplitude fluctuations are then photo-detected, and finally observed on a spectrum analyzer.

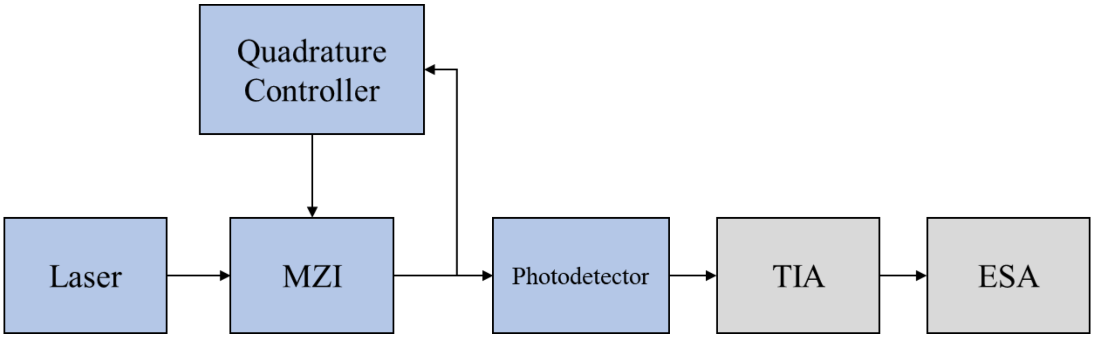

Figure 2.2 Laser diode frequency noise measurement.

Measurements will show that on top of the frequency noise obtained according to Eq. 2.3 for uniform noise sources, the laser frequency noise spectrum of an SG-DBR will be dominated by f^{-1} flicker frequency noise at low offset frequencies. In [9] the flicker noise of an SG-DBR dominates up to offsets of 200 MHz and is independent of the gain current. It is essential to attenuate noise within the system and of the laser to an acceptable level which is suitable for the application. For this purpose, the IPDA lidar master laser relies on a reference gas cell and CO_2 absorption line and a feedback frequency locking loop to enhance the coherence of the laser.

The relative intensity noise (RIN) of the laser is a measure of the average power contained in the amplitude fluctuations of the laser relative to the average signal power of the laser. This measure is quantified using Eq. 2.4.

$$RIN = \frac{<\delta P(t)^2>}{P_0^2} \tag{2.4}$$

One can also obtain RIN by integrating the spectral noise power over the system bandwidth of interest and dividing by the signal power.

2.1.2 Time Domain Variances

There are several useful time domain statistical representations of the frequency of a laser. Time domain characterization can be done using an electronic frequency counter. For laser frequencies some sort of optical-to-electronic conversion technique is required. In much of this work a bench-top external cavity laser (ECL) is utilized as a gold standard frequency reference. Without appropriate characterization of the ECL, there can be significant limitations on the interpretation of the statistics obtained. A more accurate picture could also be obtained using two sets of equivalent experiments. Due to limited yield, lab space, and equipment, we relied on an ECL which had a linewidth of 100 kHz and drift performance that was significantly better than our own free running laser diodes.

The classical variance can be used to characterize the frequency of a laser but includes a bias that grows with measurement time. This can be due to systematic sources of error in the lab such as thermal or mechanical drift [10]. Eq. 2.5 shows the classical variance where $\bar{y}_k$ represents the average frequency obtained over an interval τ and $\langle \bar{y} \rangle_N$ represents the average of N of those values.

$$\sigma_y^2(\tau) = \frac{1}{N-1} \sum_{k=1}^{N} [\bar{y}_k - \langle \bar{y} \rangle_N]^2 \qquad (2.5)$$

We later make use of the standard deviation because we are interested in the long-term accuracy of our laser which will be periodically pulsed. Averaging over multiple pulses will be required to meet the lidar accuracy specifications.

Allan variance is more commonly used in cases where bias due to systematic sources of error need to be eliminated. Instead, the frequency stability due to noise processes is estimated.

This also levels the playing field across devices that are tested under various environmental conditions that can differ from suppliers. The Allan variance is provided in Eq. 2.6 where once more the measurement interval is over a period τ. It is also known as the 2-sample variance since statistically it is the expectation of two contiguous samples.

$$\sigma_y^2(\tau) = \frac{1}{2(N-1)} \sum_{k=1}^{N-1} [\bar{y}_{k+1} - \bar{y}_k]^2 \qquad (2.6)$$

An Allan deviation plot, which is the square root of the variance, provides the tester with a breakdown of the noise processes that dominate over a test interval time and hence are typically plotted as the absolute or fractional frequency deviation as a function of the averaging time. The results parallel those that can be obtained from measurements of the frequency noise spectral density as a function of frequency offset from the carrier.

Fig. 2.3 shows the relationship between the frequency noise spectral density and the Allan variance plots and labels the dominant noise processes in the appropriate interval [10]. The plots show that frequency flicker and white noise, with *1/f* and flat spectral densities respectively, translate to flat and *1/τ* Allan variance responses respectively. In general, it is easier to measure frequency noise at higher offsets using the spectral density of the noise on a spectrum analyzer while it is easier to measure the Allan variance at longer time scales for estimation of the slower frequency noise components.

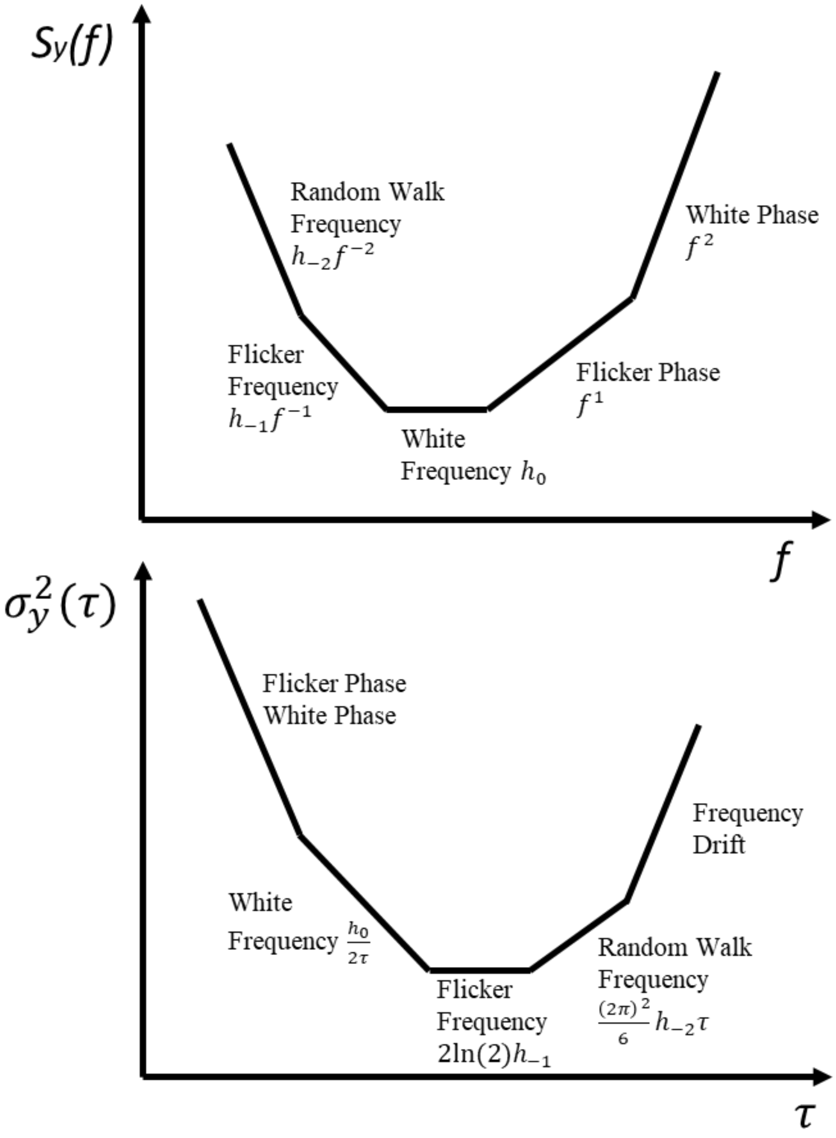

Figure 2.3 Frequency noise spectral density, Allan variance, and their relationship.

2.2 Frequency Modulation Stabilization

2.2.1 Introduction

Many applications require highly coherent lasing sources that are precise and accurate. Applications that benefit from such sources include spectroscopy, coherent communications, lidar, and optical clocks [11-14]. There exist several techniques for laser stabilization. The most well-known is the Pound-Drever-Hall (PDH) stabilization technique [15]. PDH stabilization relies on rapid modulation of the laser frequency to detect frequency deviations from a stable cavity resonance. While the reflected sidebands off the cavity do not see a phase shift, a non-zero phase shift is imposed on the carrier. The mixing products on a detector can no longer cancel out and produce an amplitude modulation. The high frequency phase modulation provides immunity over low frequency amplitude modulation as the detection occurs at a frequency that is shot noise limited. This is in contrary to the case of side locking to a resonance where the frequency and amplitude modulation of the laser are indistinguishable. PDH is so widely used because it allows utilization of loop bandwidths far greater than the cavity photon storage time [16].

In this work a frequency modulation technique was utilized due to the complexity associated with cavity stabilization for flight applications. Frequency modulation stabilization is derived from frequency modulation laser spectroscopy which was developed for characterization of weak absorption and dispersion of spectral features [17]. The technique uses a laser and external phase modulator to generate weak side bands (modulation index << 1) at frequencies that are large compared to the spectral feature linewidth. A sideband can then probe the spectral feature by either sweeping the carrier wavelength or modulation frequency. For the more general case, a set of modulation frequency and index conditions can generate line shapes with opposite polarity for both the dispersion and the absorption that can be utilized for laser frequency locking applications [18].

There are several examples in the literature that rely on gas molecular lines for laser stabilization in the short-wave infrared region. In [19], frequency stability at the kHz level is accomplished by locking to rubidium sub-Doppler lines at the 780 nm second harmonic of a laser diode.

In this work we relied on the CO_2 absorption line at 1572.335 nm that we are studying to serve as a frequency reference. We utilized a Herriott gas cell with 10-m equivalent path length, and CO_2 pressure of 40 mBar. We relied on this line since other common wavelength references such as C_2H_2, CO, $H^{13}C^{14}N$, and ^{87}Rb, do not have strong absorption lines near 1572.335 nm [11]. Spectroscopy systems based on these lines must therefore rely on increased system complexity to probe our CO_2 line. For example, in [20], a laser diode second harmonic is locked to a rubidium atomic transition and then a frequency comb spanning 45 nm is used for probing the 1.56-μm spectral region.

2.2.2 Theory of Frequency Modulation Spectroscopy

The most complete derivations of frequency modulation spectroscopy are for the special case of small modulation index (M<<1) and modulation frequencies that are large compared to the spectral feature linewidth [17]. While these were not the conditions realized in this work, it is nevertheless informative to study this analysis. In the next section, line shapes that can be used in frequency modulation stabilization for a variety of modulation indices and frequencies will be introduced for different system parameters. A numerical analysis of the line shape over a variety of conditions can then be performed for arbitrary values of the modulation index and frequency to optimize the line shape response. A general expression for arbitrary values is provided in [21].

When the modulation frequency is large compared to the spectral feature, both the absorption and dispersion can be measured by monitoring the phase and amplitude of a heterodyne beat note. The beat note is generated upon detection, after passing through a sample with spectral feature of interest that distorts the frequency modulated spectrum. Equation 2.7 provides an expression for a frequency modulated laser with M<<1 before interacting with the spectral feature. Only the first order side bands are considered.

$$E(t) = \frac{E_0}{2}\left\{-\frac{M}{2}\exp[i(\omega_c - \omega_m)t] + \exp(i\omega_c t) + \frac{M}{2}\exp[i(\omega_c + \omega_m)t]\right\} \qquad (2.7)$$

The beam passes through a sample of length L with the spectral feature of interest. The absorption coefficient α and the refractive index n are functions of the laser frequency. The attenuation and phase shift for each spectral component can be defined according to Eq. 2.8, Eq. 2.9, and Eq. 2.10 where j = 0, ±1 represents the carrier and sidebands respectively.

$$T_j = \exp\left(-\delta_j - i\varphi_j\right) \qquad (2.8)$$

$$\delta_j = \alpha_j \frac{L}{2} \qquad (2.9)$$

$$\varphi_j = \frac{2\pi n_j L(f_c - j f_m)}{c} \qquad (2.10)$$

The transmitted field though the sample is given by Eq. 2.11.

$$E_T = \frac{E_0}{2}\left\{-T_{-1}\frac{M}{2}\exp[i(\omega_c - \omega_m)t] + T_0\exp(i\omega_c t) + T_1\frac{M}{2}\exp[i(\omega_c + \omega_m)t]\right\} \quad (2.11)$$

Eq. 2.12 shows the intensity detected on a photodiode after dropping M^2 terms and assuming that $|\delta_0 - \delta_1|, |\delta_0 - \delta_{-1}|, |\varphi_0 - \varphi_1|, |\varphi_0 - \varphi_{-1}|$, are << 1. An electrical signal will thus be detected if the absorptions of the sidebands are different or if the average phase shift experienced by the sidebands is different than that of the carrier.

$$I(t) = \frac{cE_0^2}{8\pi}e^{-2\delta_0}[1 + (\delta_{-1} - \delta_1)Mcos(\omega_m t) + (\varphi_1 + \varphi_{-1} - 2\varphi_0)Msin(\omega_m t)] \quad (2.12)$$

It is worth noting again this is the case for small M and large modulation frequencies. If the modulation frequency is small, the in-phase and quadrature component values will vary.

Since we want the absorption feature to be probed by a single sideband in this case, while the carrier and other sideband experience identical background intensity and phase changes, Eq. 2.12 can be simplified according to Eq. 2.13, which shows the detected intensity as a side band is swept across a spectral feature under these conditions.

$$I(t) = \frac{cE_0^2}{8\pi}e^{-2\bar{\delta}}[1 - \Delta\delta Mcos\omega_m t + \Delta\varphi Msin\omega_m t],\ \Delta\delta = \delta_1 - \bar{\delta},\ \Delta\varphi = \varphi_1 - \bar{\varphi} \quad (2.13)$$

Eq. 2.13 indicates that the in-phase component is proportional to the absorption while the quadrature component is proportional to the dispersion induced by the spectral feature.

It is also important to note that this beat note can be detected with a high degree of sensitivity since the modulation frequency can be selected so that the laser frequency noise is not a factor. In the case of a purely absorptive feature and shot noise limited detection, the minimal detectable absorption with a unity signal-to-noise ratio and receiver bandwidth of Δf increases with laser power and modulation index according to Eq. 2.15 where η is the quantum efficiency of the detector.

$$\Delta\delta_{min} = 2[\eta M^2 \left(\frac{P_0}{\hbar\omega_c}\right)\left(\frac{1}{\Delta f}\right)]^{-\frac{1}{2}} \tag{2.15}$$

2.2.3 Parameter Dependence of Line Shapes

The more generalized analysis of frequency modulation absorption spectroscopy in terms of the modulation index M and modulation frequency ω_m is summarized in [21], Fig. 2. Assuming a Lorentzian spectral feature the figure shows the effect of changing M and ω_m. In that figure, ω_m is normalized to the Lorentzian width Γ which is set to 1. The key takeaway is that there is a range of modulation frequencies and indices over which a spectral feature can be probed to generate a suitable frequency discriminating error signal. For normalized ω_m, there is a range of settings where for $0.01 \leq \omega_m \leq 1$, and $1 \leq M \leq 100$, the strongest error signals can be obtained. We initially examine the case for small M and large ω_m, which yields inverse copies of the spectral features separated by twice the modulation frequency and so is not appropriate for stabilization. This is also the case for large M and large ω_m as well since the large M simply shifts the signal to higher order side bands. A weak M does not generate a strong signal, especially at low ω_m.

In our work we have relied on the dispersion spectroscopy which is not as strongly affected by strong deterministic sources of residual amplitude modulation in the phase modulator. The frequency discriminating error signal obtained is illustrated in Fig. 5.1. The SG-DBR laser on our PIC was modulated at 125 MHz and a modulation index of π radians to obtain a suitable frequency discriminating error signal for laser wavelength locking. The FWHM linewidth of our CO_2 reference was 500 MHz.

2.2.4 Frequency Stabilization Feedback Loop Design

The SG-DBR-in-PIC frequency stabilization system is demonstrated in Fig. 2.4. A phase modulator following the SG-DBR frequency modulates the master laser. The PIC output is collected with a lensed fiber and directed to the Herriott gas cell reference. Coherent detection of a beat note generates a frequency discriminating error signal that can be used for SG-DBR stabilization. That error is filtered by the servo and converted to a modulation current that is fed back to the PIC master SG-DBR phase section. To analyze the frequency stabilization feedback loop, we note that the purpose of the entire portion of the frequency stabilization system of Fig. 2.4 that is enclosed in the rectangle with dashed outline, is to generate a frequency discriminating error signal when the SG-DBR master laser is perturbed with respect to a reference. Thus, the feedback loop can be modeled according to Fig. 2.5 as a frequency locked loop.

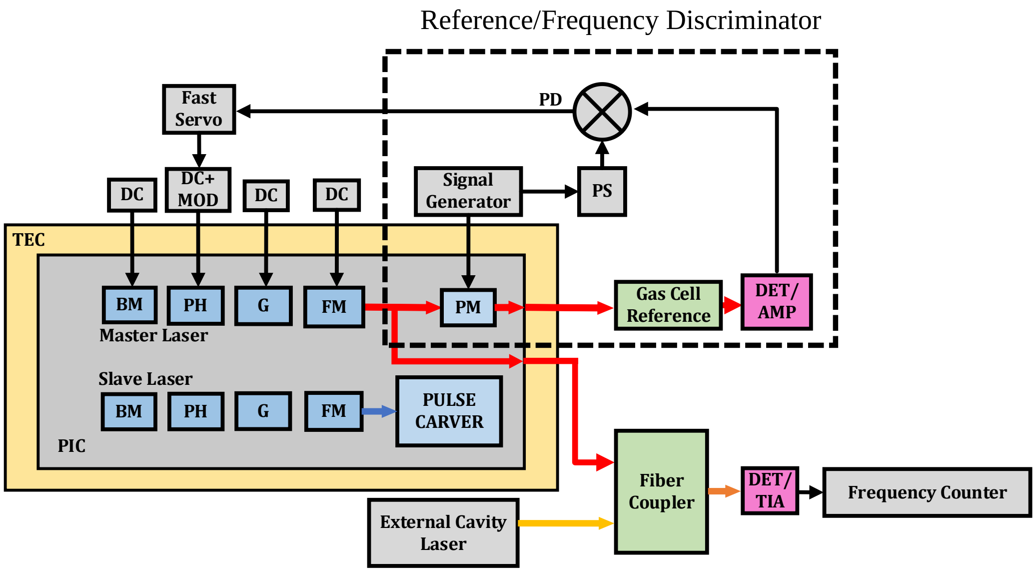

Figure 2.4 PIC SG-DBR frequency stabilization. For feedback analysis, the components in the dashed rectangle can be simplified to a frequency discriminator.

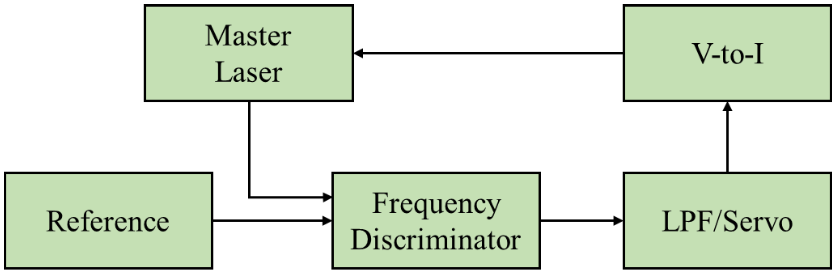

Figure 2.5 Simplified frequency stabilization feedback loop model.

The key elements of this feedback loop are the master laser phase section tuning sensitivity K_{LAS}, the frequency discriminator gain K_D, the V-to-I tuning sensitivity K_{VI}, and the loop filter generated using a servo and low pass filter (LPF). For simplicity it is assumed that all the key elements have transfer functions that are frequency independent with exception of the LPF/servo. This assumption is valid for narrow band electronic feedback loops with bandwidths that are tens of kilohertz. Otherwise, the loop delay in the lab must be considered.

K_{LAS} has units of rad/sec/mA, K_{VI} has units of mA/V, K_D has units of Vsec/rad and the LPF/Servo has units of V/V. The values of each were estimated from measurements obtained in the lab and are summarized in Tab. 2.1. The mathematical abstraction for our loop analysis is in the Laplace domain.

The proper specifications for the LPF and servo must be determined to maintain good stability. An expression for a first order LPF is provided in Eq. 2.16, where ω_p is the pole frequency in units of rad/sec. We can now note that using the servo we can add an ideal integrator to the system open loop response to generate a feedback loop with second order behavior. The ideal integrator is expressed in Eq. 2.17. The circuit to accomplish this, along with the low pass filter, is demonstrated in Fig. 2.6.

Specification	Symbol	Value	Unit
Frequency Discriminator Gain	K_D	$\frac{0.45\,V}{2\pi * 250\,MHz}$	secV/rad
Phase Section Tuning Sensitivity	K_{LAS}	$2\pi * 8 * 10^9$	rad/sec/mA
V-to-I Sensitivity	K_{VI}	-2.5	mA/V
Low Pass Filter Pole	f_p	75	kHz
Servo Gain	f_1	100	Hz
Natural Frequency	f_n	10	kHz
Damping Ratio	ζ	3.6	

Table 2.1 Frequency locked loop design parameters.

$$H_{LPF}(s) = \frac{1}{1+s/\omega_p} \tag{2.16}$$

$$H_I(s) = -\frac{1}{sR_1C_1} = -\frac{\omega_1}{s} \tag{2.17}$$

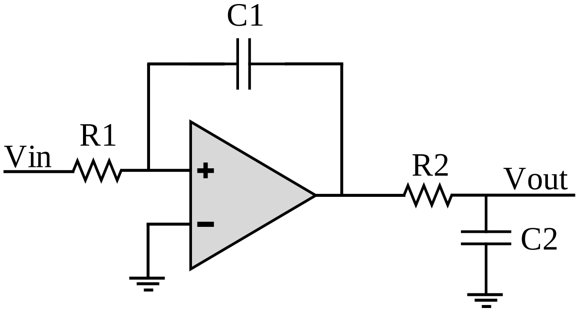

Figure 2.6 Equivalent circuit of servo and low pass filter used in feedback loop.

We can now specify the loop gain G(s) and closed loop response H(s) according to Eq. 2.18 and 2.19 respectively where $K=K_{LAS}K_DK_{VI}\omega_1$.

$$G(s) = K_{LAS}K_DK_{VI}H_{LPF}H_I \tag{2.18}$$

$$H(s) = \frac{G(s)}{1+G(s)} = \frac{K}{R_2C_2s^2+s+K} \tag{2.19}$$

The denominator can now be written in standard form as in Eq. 2.20 where ζ is the damping factor and ω_n is the natural frequency according to Eq. 2.21 and Eq. 2.22 respectively.

$$s^2 + 2\zeta\omega_n s + \omega_n^2 \tag{2.20}$$

$$\zeta = \frac{1}{2}\sqrt{\frac{\omega_p}{K}} \tag{2.21}$$

$$\omega_n = \sqrt{K\omega_p} \tag{2.22}$$

Fig. 2.7 shows the open loop gain response. The phase margin at the crossover frequency is 89°. Fig. 2.8 and Fig. 2.9 show the closed loop response and step response respectively. Note that the feedback loop behaves as a low pass filter as expected. The slow variations in frequency are closely followed while the fast changes are attenuated. The high damping ratio obtained in this design and narrow bandwidth generate a slow loop response to a step frequency change. The step response shows that about 0.5 msec is required for the loop to settle.

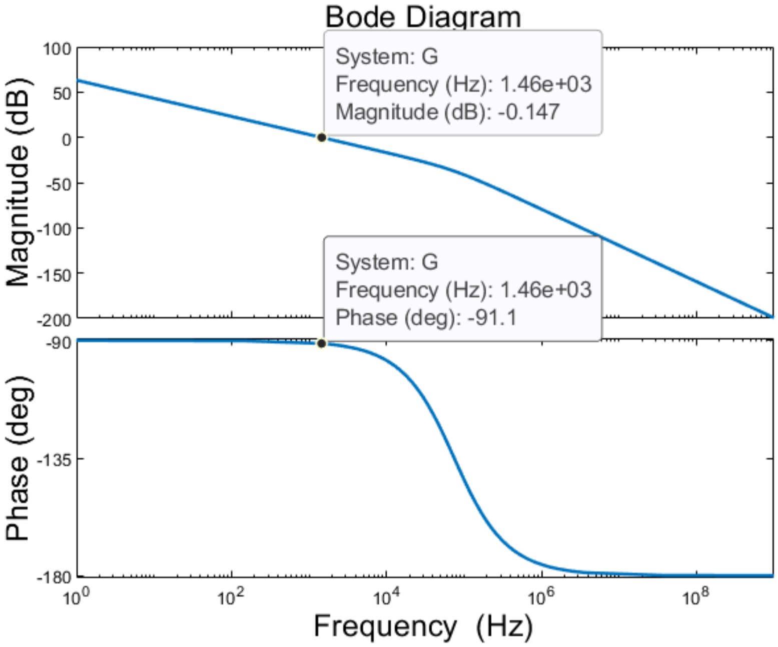

Figure 2.7 Loop gain and phase margin of the frequency locked loop.

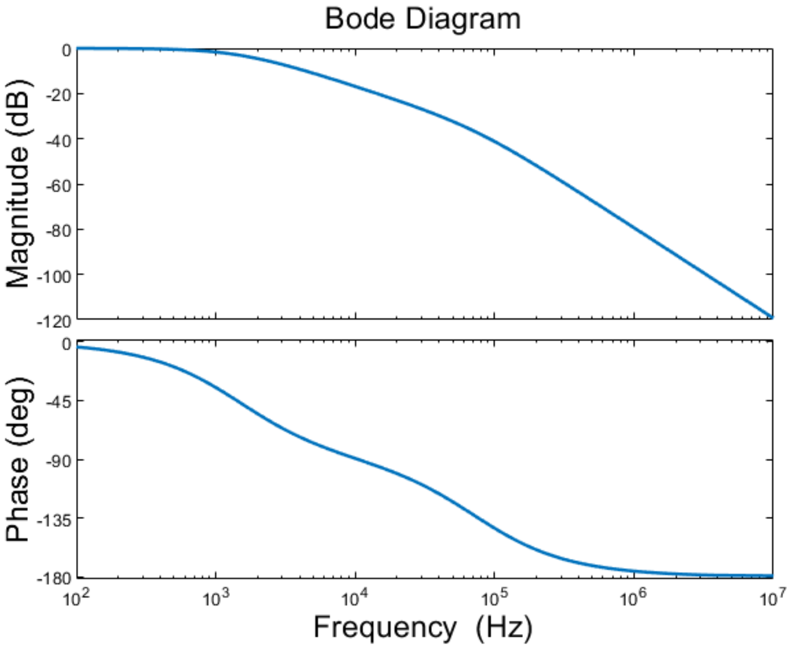

Figure 2.8 Closed loop response of the frequency locked loop.

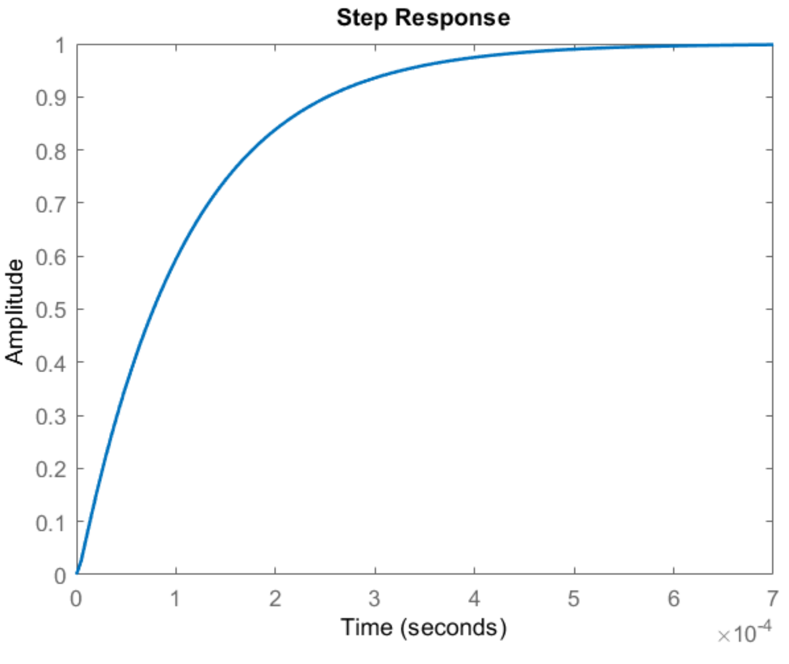

Figure 2.9 Step response of the frequency locked loop.

Note that this loop design is identical to type-I PLLs which has several drawbacks compared to the type-II counterpart. The type designation indicates the number of ideal integrators in the open loop response. One drawback includes reduced stability as the loop gain is increased. This can be intuitively understood from the loop gain plot by noticing that shifting the plot vertically increases the crossing point and thus reduces phase margin. Another drawback is that reducing the LPF pole frequency to minimize spurious modulation of the laser frequency, also leads to reduced stability and a greater ripple in the step response. This tradeoff can be eliminated with a type-II PLL as is implemented in the PIC OPLL and discussed in section 2.3. In actual lab experiments the LPF used had much sharper rolloff than a 1st order response. To eliminate the tradeoffs discussed above as well as obtain greater loop gain for attenuation of slow frequency noise components, a slightly more sophisticated servo with dual integrators and proportional control could have been utilized.

The active control suppresses the noise within the loop bandwidth and generally, it is preferable to set the loop gain to a level that suppresses strong 1/f flicker noise to a level below the Schawlow-Townes quantum limit [22]. The reduction in the closed loop spectral density of the laser frequency noise is given by Eq. 2.23. S_{cl} and $S_{f,\mathrm{laser}}$ are the noise spectral density of the laser with and without feedback respectively in units of $Hz/\sqrt{Hz}$, K is once again $K=K_{LAS}K_{D}K_{VI}\omega_{1}$, and G is the frequency dependent servo gain.

$$S_{f,cl} = \frac{S_{f,laser}}{|1+KG|} \tag{2.23}$$

2.3 Optical Phase Locked Loops

2.3.1 Introduction

Phase Locked Loops (PLLs) filter out undesirable fast phase excursions and follow slow ones. They are essential circuit blocks in communications systems which have stringent carrier frequency specifications, including mobile networks, Wi-Fi, and space communications. PLLs perform frequency synthesis that is both precise and accurate and meets the required channel resolution in congested multi-user networks. PLLs also improve the phase noise performance of Voltage Controlled Oscillators (VCOs) which serve as the RF/Microwave carriers is these networks.

OPLLs extend the operation of PLLs into the optical domain. Applications such as optical atomic clocks, dual comb spectroscopy, lidar, and sensing rely on OPLLs for accurate and precise control of optical wavelengths. Fig. 2.10 illustrates the key building blocks of the OPLL.

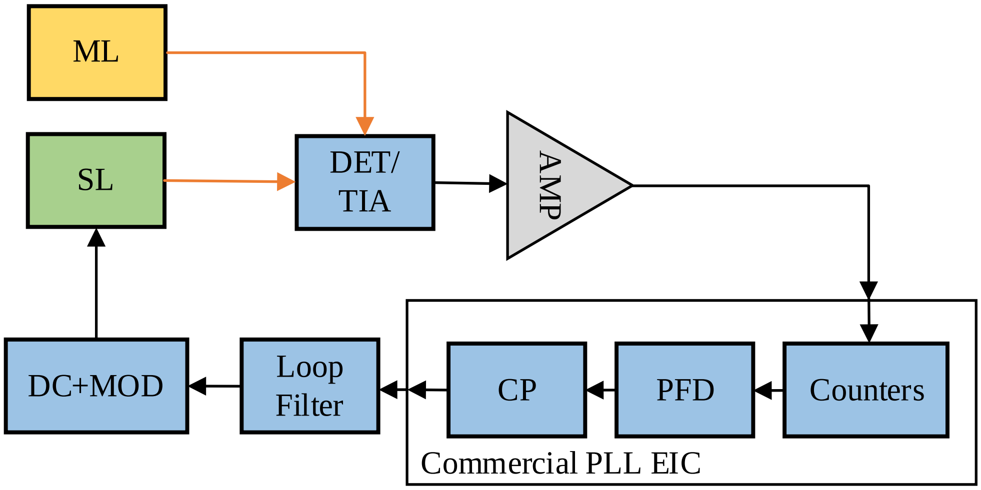

Figure 2.10 Building blocks of an optical phase locked loop.

The master laser serves as a reference for offset frequency locking the slave laser. The frequency noise performance of the master laser is assumed to be far superior to that of the slave laser. The master and slave lasers are tuned within the detector bandwidth and preferably as close as possible to the desired programmed offset frequency the loop is required to maintain between the two lasers. After the beat note is amplified with a TIA and amplifier, it is processed by a COTS packaged electronic integrated circuit. The PLL circuit contains counters, a phase-frequency detector (PFD), and a charge pump (CP). The charge pump output is filtered with a loop filter and a voltage-to-current (V-to-I) converter modulates the slave laser phase section to maintain the programmed offset frequency from the master laser.

PLL integrated circuits typically contain frequency counters composed of a 16-bit programmable counter and selectable dual modulus 4/5 or 8/9 prescalars for example. Simplified counter details are illustrated in Fig. 2.11 [23].

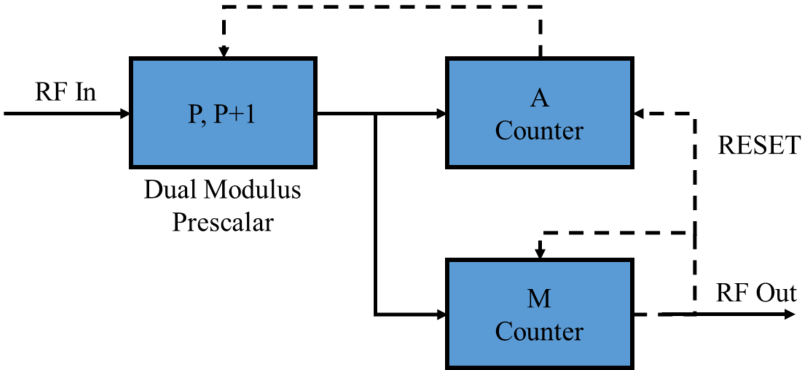

Figure 2.11 OPLL counter details.

The output RF, which serves as a comparison frequency to a reference at the PFD, can be described in terms of the input RF with Eq. 2.24 and Eq. 2.25.

$$f_{RF,IN} = N f_{RF,OUT} \tag{2.24}$$

$$N = MP + A = (M - A)P + A(P + 1) \tag{2.25}$$

In Eq. 2.25, P and $P+1$ are the dual modulus prescalars and the A and M counters are programmable. Eq. 2.25 indicates that the input frequency can be set to an integer multiple of the output frequency by using a dual modulus counter in a $P+1$ setting and counting A cycles of the input RF, and then in the P setting and counting M-A cycles of the input RF. Hence, if the output RF is equal to the phase detector comparison frequency, the input RF can be set to an integer multiple of that comparison frequency. For example, if the output RF is 100 MHz, the input RF can be set to 2.6 GHz using the settings: $P = 4$, $A = 2$, $M = 6$. It is important to note that theoretically only one divider is required to obtain input RF frequencies that are integer multiples of the output RF, but such hardware is difficult to construct over a broad frequency range. For int-N dividers, designers use the above architecture. In the mathematical modelling that follows we simply use N for frequency division.

A narrow bandwidth frequency multiplying OPLL can be described quantitatively much like any standard frequency multiplying PLL. In the following, I therefore focus on the key takeaways from a linear analysis of type-II PLLs. The type-II designation refers to the number of ideal integrators in the open-loop transfer function. The mathematical abstraction is in the Laplace domain and the input to and output from the OPLL feedback loop are the excess phases. The linearized model of the OPLL setup in the lab is demonstrated in Fig. 2.12.

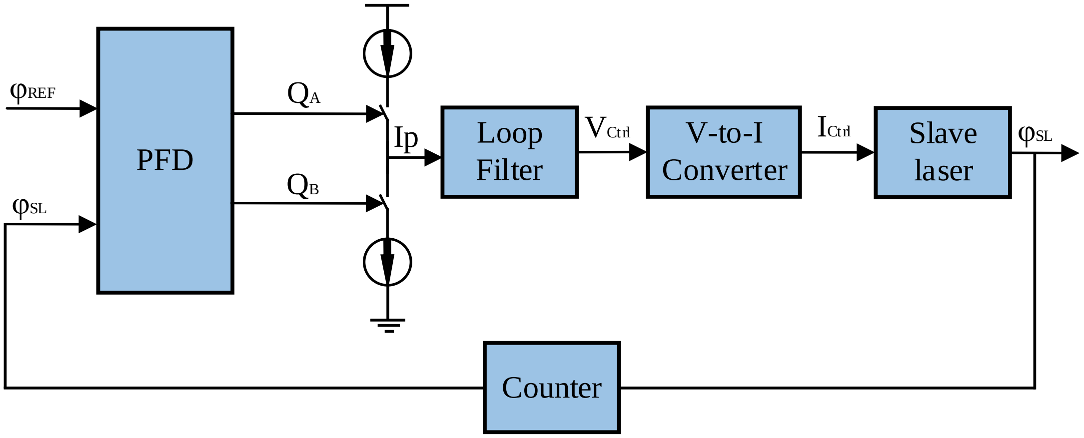

Figure 2.12 Model of OPLL.

One ideal integrator is contained in the slave laser, where injection of an electrical current into the SG-DBR laser phase section proportionally shifts the laser frequency. The phase accumulation can be described according to Eq. 2.26 where K_{LAS} is the slave laser phase section tuning sensitivity and K_{VI} is the V-to-I converter tuning sensitivity. K_{LAS} has units of rad/sec/mA. Both K_{LAS} and K_{VI} are assumed to be frequency independent in our analysis.

$$\frac{\varphi_{SL}}{V_{Ctrl}}(s) = \frac{K_{LAS}K_{VI}}{s} = \frac{K}{s} \qquad (2.26)$$

The second integrator is contained in the PFD/CP/loop filter combination. The PFD/CP/loop filter hardware input/output response is non-linear in operation since a change in the input excess phase is not accompanied by a proportional change in the output. Nevertheless, the mathematical description for time scales much greater than the input signal periods allows linearization of the response [24]. Open loop analysis of a type-II OPLL with a pure integrator PFD/CP/loop filter response shows that it is unstable as the phase margin is zero. This is because the two combined ideal loop integrators introduce a 180° shift in the open loop response. This problem is fixed by introducing damping into the circuit in the form of a lossy resistor. The filter used in this work is illustrated in Fig. 2.13. The filter has 4 poles for a 5th order loop. Eq. 2.27 shows the loop filter transfer function. The poles provide greatly increased rolloff which improves the spurious performance of the OPLL. This is especially critical for OPLLs due to the high tuning sensitivity of the laser.

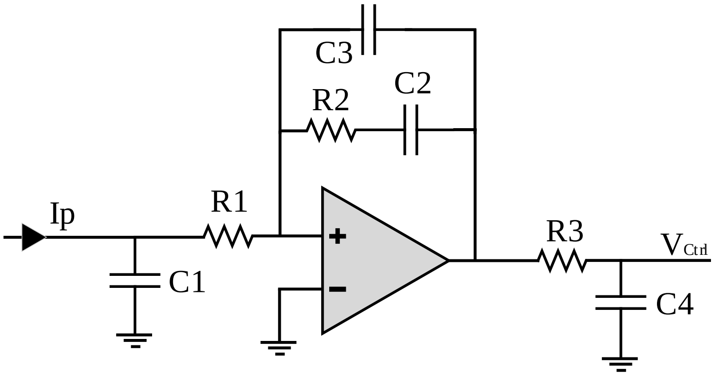

Figure 2.13 OPLL loop filter. 4 poles help reduce spurious content from PFD.

$$\frac{V_{Ctrl}}{I_p} = \frac{(1+sR_2C_2)}{sC_2(1+sR_1C_1)(1+sR_2C_3)(1+sR_3C_4)} \tag{2.27}$$

After linearization of the PFD/CP/filter cascade response, the loop gain can be expressed according to Eq. 2.28.

$$G(s) = \frac{V_{Ctrl}}{\Delta\varphi}(s) = \frac{I_p}{2\pi}\frac{(1+sR_2C_2)}{sC_2(1+sR_1C_1)(1+sR_2C_3)(1+sR_3C_4)} \tag{2.28}$$

The resulting simplified second order closed loop transfer function is described by Eq. 2.29. Because the poles at *R1C1*, *R2C3*, and *R3C4* should not significantly affect the loop dynamics, they were eliminated from the closed loop response. These poles must nevertheless be selected carefully because if placed incorrectly, they can degrade the phase margin performance of the loop which may lead to instability. Their use is illustrated after the initial simplified design.

$$H(s) = \frac{\frac{I_pK}{2\pi C_2}(R_2C_2s+1)}{s^2+\frac{I_pKR_2s}{2\pi N}+\frac{I_pK}{2\pi NC_2}} \qquad (2.29)$$

The denominator can now be written in standard form as in Eq. 2.30 where ζ is the damping factor and ω_n is the natural frequency according to Eq. 2.31 and Eq. 2.32 respectively.

$$s^2 + 2\zeta\omega_n s + \omega_n^2 \qquad (2.30)$$

$$\zeta = \frac{R_2}{2}\sqrt{\frac{I_pC_2K}{2\pi N}} \qquad (2.31)$$

$$\omega_n = \sqrt{\frac{I_pK}{2\pi C_2N}} \qquad (2.32)$$

Note that the type-II PLL has eliminated the ripple-stability tradeoff of the type-I PLL behavior we obtained in the frequency locked loop. Here, unlike the type-I, an increase in C_2 results in an increase in ζ and thus reduces ripple on the control voltage.

2.3.2 Loop Design

The above equations must be used together to carefully find the proper balance between a well-behaved transient response and a settling time appropriate for the application. After initial estimates are verified in test, the loop can be appropriately tuned to meet specifications where the performance falls short.

It was found that sampling the CO_2 gas absorption line at 1572.335 nm at ± 1, ± 1.2, ± 1.5, ± 2, ± 2.5, ± 4, ± 8 GHz offsets to the master laser, yielded measurements over a wide enough range to comfortably resolve the absorption line shape and overlay of a Lorentzian fit to the data. This is discussed in the system measurements section in Ch. 6. The OPLL is therefore designed to operate over frequency offsets from 1-10 GHz. It is important to ensure that specifications are met over the entire offset frequency range. This requires that the loop bandwidth and phase margin be consistent or predictably modified at all offsets so that the stability and transient response are satisfactory.

Both the damping ratio and natural frequency are a function of the counter N which is modified for each new offset according to Eq. 2.31 and Eq. 2.32 respectively. For example, for a 1 GHz offset and 100 MHz comparison frequency the division ratio N is 10 while it is 100 for a 10 GHz offset. Luckily, the performance can be maintained at each offset for a set selection of filter resistors and capacitors by simply modifying the charge pump current for every offset. PLL charge pump currents are programmable. Thus, if we switch from a division ratio N of 10 to 100, the charge pump current needs to increase by a factor of 10 as well. The programmable range of the COTS PLL charge pump current is 300 µA to 4.8 mA.

The design parameters and components are initially obtained for an offset frequency of 2 GHz and reference frequency of 100 MHz using a small charge pump current of 600 µA so that at a 10 GHz offset, a charge pump current of 3 mA may be used. Because the minimum PLL chip *N* divider value is 20, the reference for a 1 GHz offset requires division by 2. This capability is built-in the PLL circuit and is programmable. For a 100 MHz crystal oscillator reference, the PFD reference can be programmed to be anywhere from 1.5625 MHz to 200 MHz. Thus, as far as the linearized loop dynamics are considered, the results are the same for 1 and 2 GHz offsets.

We also note that dividing the output frequency by *N* reduces stability and response time. Intuitively the signal edges are compared *N* times less often as opposed to the case of equal input and output frequencies and so the loop has less opportunity to respond to phase changes. We thus prefer a comparison frequency at the PFD that is high so as to minimize *N*.

Table 2.2 summarizes the key performance specifications initially targeted for the OPLL.

Specification	Symbol	Value	Unit
Frequency Offsets of Interest	f	1-10	GHz
Design Frequency	f_{DES}	2	GHz
Phase Section Tuning Sensitivity	K_{LAS}	$(2\pi) * 8 * 10^9$	rad/sec/mA
V-to-I Sensitivity	K_{VI}	-2.5	mA/V
Charge Pump Current	I_P	0.6	mA
Divider	N	20	
PFD Comparison Frequency	f_{PD}	100	MHz
Damping Ratio	ζ	1	
Natural Frequency	f_c	$100 * 10^3$	Hz

Table 2-2. OPLL loop parameters.

Ideally, we want to target a phase margin of 60 degrees or better to maintain good loop stability. Using Eq. 2.33, we can obtain the capacitance value C2 for a given natural frequency, knowing that for well-behaved loops, the phase locking bandwidth is approximately equal to the natural frequency. Using the closest value available from capacitor lab kits, we can then find R2 for a damping ratio of 1. Fig. 2.14 shows the loop gain and phase responses using these initial C2 and R2 values while ignoring the impact from all other poles in the loop filter.

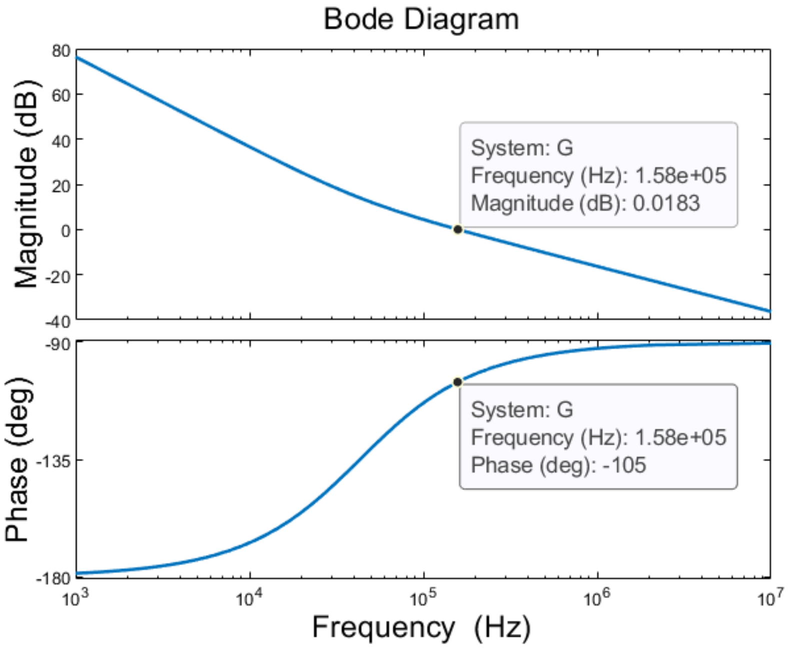

Figure 2.14 OPLL simplified loop gain and phase margin.

Examination of the results shows that the phase margin, obtained at the crossover frequency at 158 kHz, is 75°. We can now use the other filter poles to obtain steep rolloff for best spurious performance. Tab. 2.3 summarizes the capacitor and resistor values for the entire loop filter and corresponding zeros and poles.

Resistance	Capacitance	Zero/Pole
R1: 220 Ω	C1: 100 pF	Pole: 7.23 MHz
R2: 8 Ω	C2: 460 nF	Zero: 43.2 kHz
R2: 8 Ω	C3: 10 nF	Pole: 2.03 MHz
R3: 30 Ω	C4: 3.3 nF	Pole: 1.61 MHz

Table 2-3. Capacitors and resistors used in loop filter and corresponding poles and zeros.

Fig. 2.15 shows the open loop gain and phase response of the OPLL using the values from Tab. 2-3. The final design shows a crossover frequency of 158 kHz and phase margin of 63°. The increased rolloff is also visible. Compared to the simplified case, which shows just -56 dB loop gain at 100 MHz, the case with improved rolloff shows -149 dB loop gain at 100 MHz. Fig. 2.16 and Fig. 2.17 show the closed loop and step responses for this same design. These components are used to obtain gas sensing measurements obtained in section 6.2.

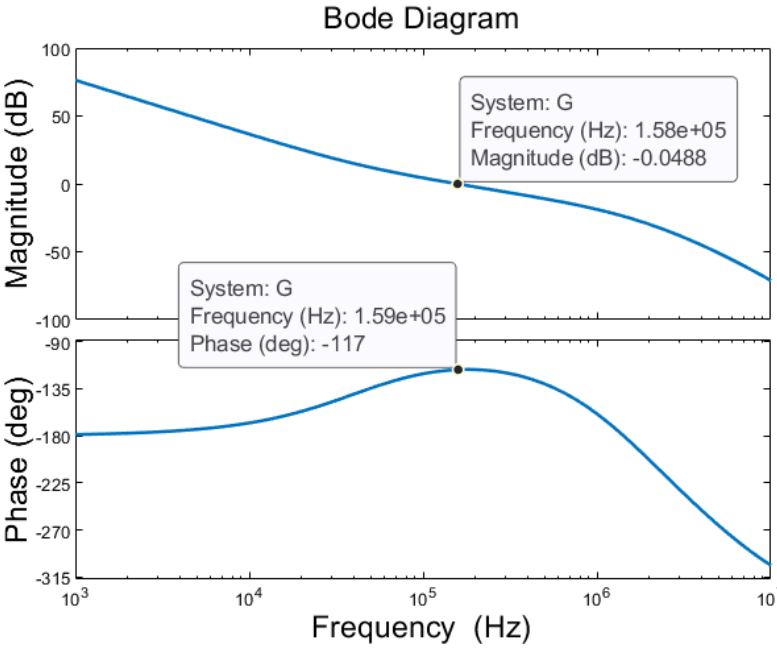

Figure 2.15 OPLL loop gain and phase margin using values from Tab. 2-3.

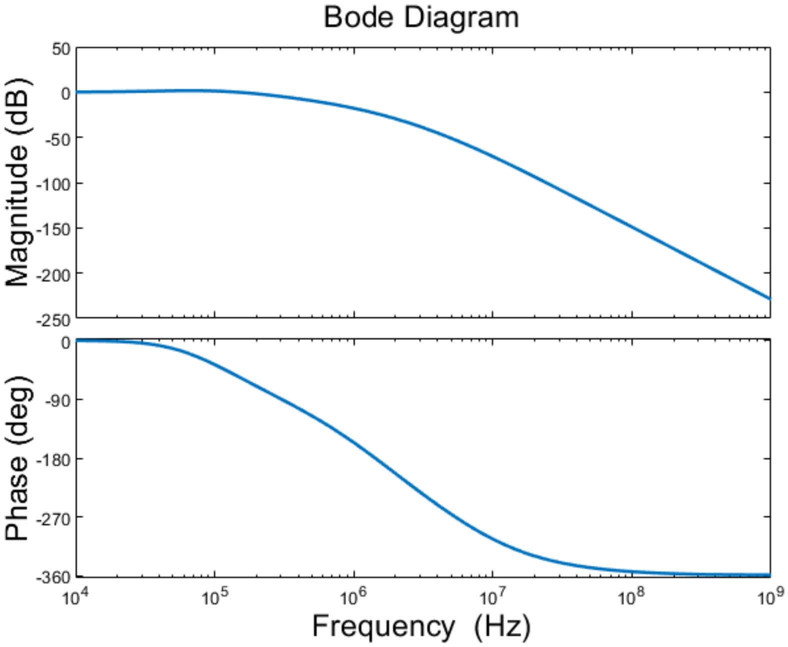

Figure 2.16 OPLL closed loop response.

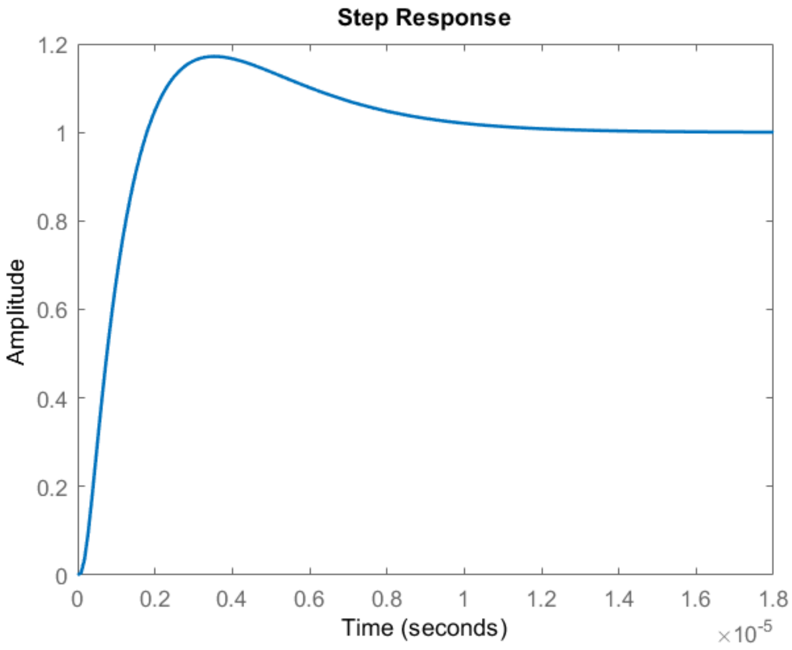

Figure 2.17 OPLL step response.

2.3.3 Transient Response

By taking the inverse Laplace transform of Eq. 2.29, we can obtain an expression for the step response of a type-II OPLL. Furthermore, because the frequency and phase are related by a linear time invariant operation the expressions are valid for both steps in frequency or phase at the input. Eq. 2.33 provides an expression for damping ratio less than or equal to 1.

$$\frac{\theta_o(t)}{N} = \theta_i(t)\left\{1 - e^{-\zeta\omega_n t}\left[\cos\left(\omega_n t\sqrt{1-\zeta^2}\right) - \frac{\zeta}{\sqrt{1-\zeta^2}}\sin\left(\omega_n t\sqrt{1-\zeta^2}\right)\right]\right\} \quad (2.33)$$

Eq. 2.33 shows that the output frequency follows the step input frequency with a decay given by $\zeta\omega_n$.

Because pulse transmission in our IPDA lidar occurs every 133 µs to prevent crosstalk from cloud scattering, we must target an OPLL frequency settling time that is significantly faster and ensure that a good balance between stability and settling time for the OPLL is still maintained. After performing tests in the lab, the original design does not reliably meet specifications for large frequency steps. Increasing the loop bandwidth can help improve the settling time performance in the lab. This study is discussed in section 6.2. Concurrently switching the tuning into the front and back mirrors and phase section of the laser can help speed up the transient response as well, but this requires automatic control [11]. In the lab setting, it was not possible to increase the bandwidth of the loop beyond a few hundred kilohertz due to bandwidth limitations in the V-to-I converter and long path delays.

A design capable of meeting transient specifications is instead verified in simulation using a simple OPLL model that is constructed in Advanced Design Systems software. The frequency dependency of the laser phase section and the path delays are not included but can be modeled with RC circuits and built-in time delay blocks. Furthermore, the frequency noise of the laser is not included in the simulation and as such this is a best-case scenario. The model is illustrated in Fig. 2.18. It shows an ideal op-amp and RC components comprising the loop filter. A PFD circuit block allows the user to set the charge pump current and the reference frequency. A VCO block, which acts as our laser, is tuned by the filter output. Its tuning sensitivity can be set according to the V-to-I and laser phase section tuning sensitivity obtained in section 2.3.2. A step change in the frequency is modeled by a step change in the division ratio at the other VCO input.

To ensure settling times are met for large frequency steps such as from 4 to 8 GHz, we increase the loop bandwidth significantly to approximately 2 MHz. This is reasonable given the large loop bandwidths illustrated in other works such as [25,26] and is at the same time significantly lower that the comparison frequency at 100 MHz which allows filtering of the spurious components leaving the PLL circuit. Fig. 2.19 and Fig. 2.20 show the new open loop gain and phase responses and closed loop response for this new design. The components selected are summarized in Tab. 2.3. Figure 2.21 shows the transient response for changes in the output frequency of the VCO for steps of 2-to-4, 4-to-8 GHz, and 2-to-12 GHz, showing that the settling time is sufficient for our application.

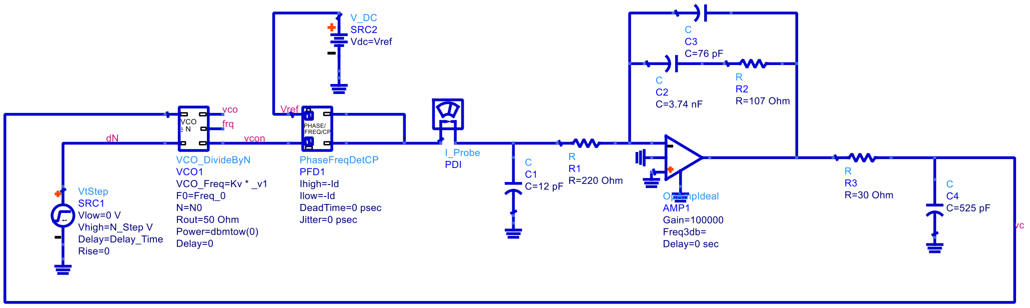

Figure 2.18 Schematic for transient analysis of an OPLL for fast switching.

Resistance	Capacitance	Zero/Pole
R1: 220 Ω	C1: 12 pF	Pole: 60 MHz
R2: 107 Ω	C2: 3.74 nF	Zero: 396 kHz
R2: 107 Ω	C3: 76 pF	Pole: 20 MHz
R3: 30 Ω	C4: 525 pF	Pole: 10.1 MHz

Table 2-3 RC components for fast OPLL switching.

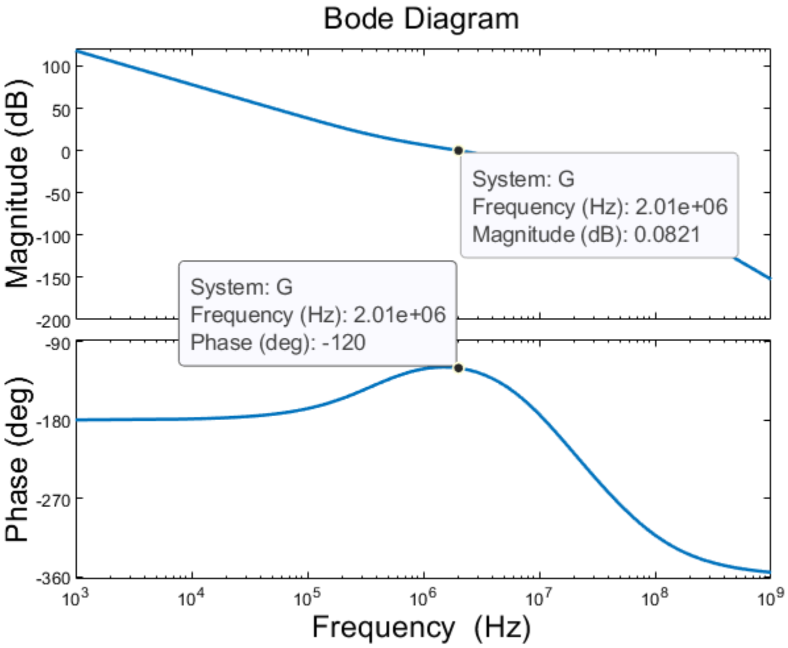

Figure 2.19 Open loop response for fast switching OPLL.

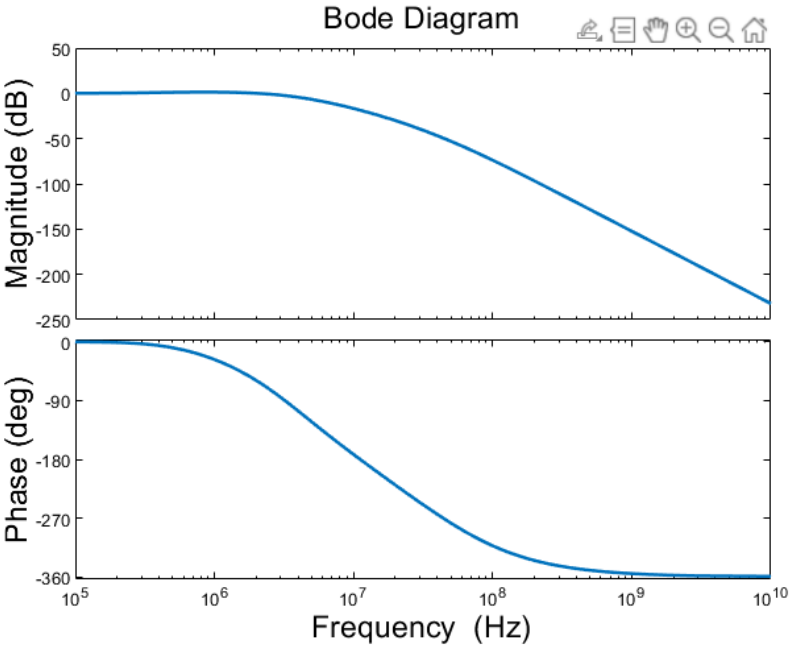

Figure 2.20 Closed loop response for fast switching OPLL.

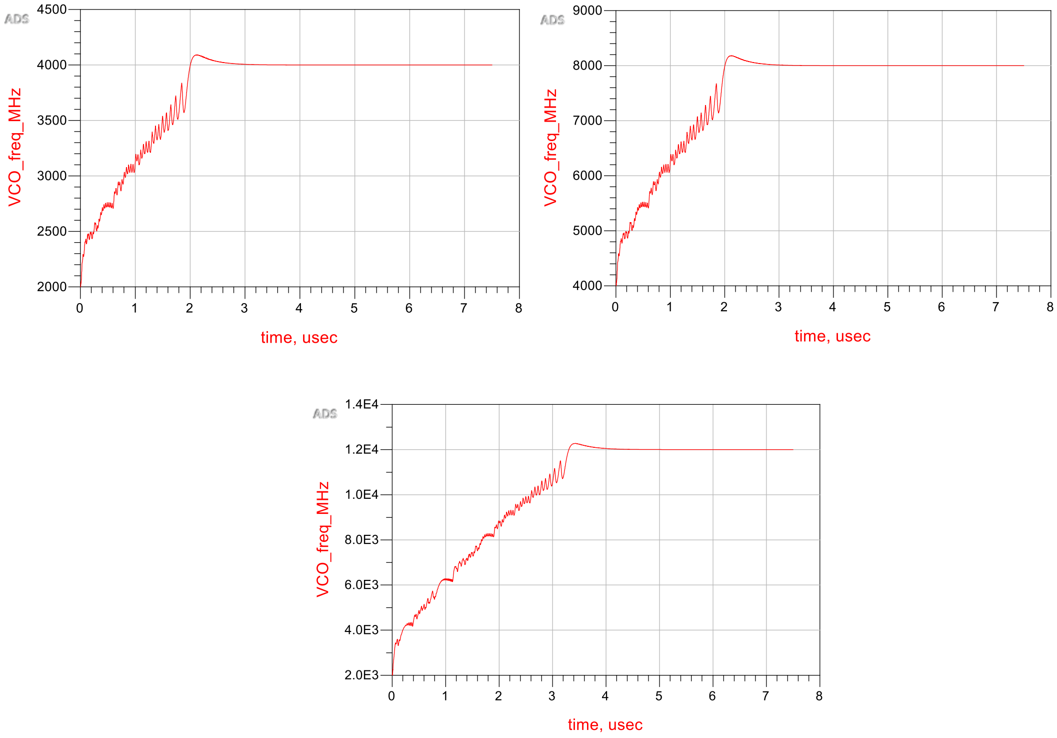

Figure 2.21 Frequency switching transient response for different frequency offset steps: 2 to 4 GHz, 4 to 8 GHz, and 2 to 12 GHz.

2.3.4 Wideband OPLLs

While the focus of this chapter has been on developing OPLLs with narrowband responses below 1 MHz, laser-based feedback systems with broad linewidths require much greater loop bandwidth, as they are otherwise relegated to slowly following the reference carrier. Because our reference laser is stabilized using a narrowband feedback loop as well, the stability will be fairly limited in the first place. Emphasis on high loop gain is also important. Increased bandwidth also requires that we consider the frequency dependent tuning response of the phase section as well as the time delay through the loop. A relationship can be obtained between the reference linewidth and the permittable delay in the loop to achieve a certain phase error variance [27-28] and appropriate compensation techniques may be required when the loop bandwidth is greater that the tuning bandwidth of the laser [26].

Eq. 2.35 shows the laser phase tuning frequency dependent response, which introduces an additional pole. This pole may be situated at approximately 100 MHz. The electro-optic response can be easily measured with a light wave network analyzer. Such a pole would have negligible effects on the dynamics of the OPLL examples illustrated so far.

$$K_P = \frac{K_{LAS}}{1+s\tau_P} \tag{2.35}$$

Modelling the time delay in the loop can be accomplished by including a delay term $e^{-s\tau}$, where τ is the time delay in the loop [29]. Time delays result in non-minimum phase control systems which can degrade the phase margin and response time of the loop [30]. Integration of all optical functions beside the laser in a complex optical system allows significant reduction in the loop delay compared to feedback loops constructed from bulk optics. Using line narrowing techniques allows utilization of SG-DBR lasers, which have relatively broad linewidth, in applications such as lidar and coherent WDM optical communications which stand to benefit from the laser’s wide tunability and low power consumption.

References

1. Stern, B., Ji, X., Dutt, A., & Lipson, M. (2018). Compact narrow-linewidth integrated laser based on low-loss silicon nitride ring resonator. *2018 Conference on Lasers and Electro-Optics, CLEO 2018 - Proceedings*, *42*(21), 21–24. https://doi.org/10.1364/ol.42.004541
2. Gundavarapu, S., Brodnik, G. M., Puckett, M., Huffman, T., Bose, D., Behunin, R., Wu, J., Qiu, T., Pinho, C., Chauhan, N., Nohava, J., Rakich, P. T., Nelson, K. D., Salit, M., & Blumenthal, D. J. (2019). Sub-hertz fundamental linewidth photonic integrated Brillouin laser. *Nature Photonics*, *13*(1), 60–67. https://doi.org/10.1038/s41566-018-0313-2
3. Schawlow, A. L., & Townes, C. H. (1958). Infrared and optical masers. *Physical Review*, *112*(6), 1940–1949. https://doi.org/10.1103/PhysRev.112.1940
4. Henry, C. H. (1982). Theory of the Linewidth of Semiconductor Lasers. *IEEE Journal of Quantum Electronics*, *18*(2), 259–264. https://doi.org/10.1109/JQE.1982.1071522
5. Verdiell, J., Koren, U., & Koch, T. L. (1992). *Linewidth and Alpha-Factor of Detuned-Loaded*. *4*(4), 302–305.
6. Larson, M. C., Akulova, Y. A., Coldren, C. W., Liljeberg, T., Fish, G. A., Nakagawa, S., Dahl, A., Kozodoy, P., Bingo, D., Bai, M., Ramdas, N., Penniman, S., Wipiejewski, T., & Coldren, L. A. (2003). High performance widely-tunable SG-DBR lasers. *Novel In-Plane Semiconductor Lasers II*, *4995*(July 2003), 66. https://doi.org/10.1117/12.475792
7. Mercer, L. B. (1991). *1 /f Frequency Noise*. *9*(4).
8. Coldren, Larry A., et al. Diode Lasers and Photonic Integrated Circuits. Wiley-Blackwell, 2012.
9. S. Nakagawa, G. Fish, A. Dahl, P. K., & C. Schow, M. M. (2003). *Phase noise of widely-tunable SG-DBR laser*. *2*, 2001–2003.
10. Rubiola, Enrico., et al. Phase Noise and Frequency Stability in Oscillators.
11. Numata, K., Chen, J. R., & Wu, S. T. (2012). Precision and fast wavelength tuning of a dynamically phase-locked widely-tunable laser. *Optics Express*, *20*(13), 14234. https://doi.org/10.1364/oe.20.014234
12. Yao, Y., Jiang, Y., Wu, L., Yu, H., Bi, Z., & Ma, L. (2016). A low noise optical frequency synthesizer at 700-990 nm. *Applied Physics Letters*, *109*(13). https://doi.org/10.1063/1.4963690
13. Oddington, I. A. N. C., Ewbury, N. A. N., & Wann, W. I. S. (2016). *Dual-comb spectroscopy*. *3*(4).
14. Udem, T., Holzwarth, R., & Hänsch, T. W. (2002). Optical frequency metrology. *Nature*, *416*(6877), 233–237. https://doi.org/10.1038/416233a

15. Black, E. D. (2001). An introduction to Pound–Drever–Hall laser frequency stabilization. *American Journal of Physics, 69*(1), 79–87. https://doi.org/10.1119/1.1286663
16. Drever, R. (1983). Laser Phase and Frequency Stabilization Using an Optical Resonator. *Applied Physics B, 31*(1983), 97–105.
17. Bjorklund, G. C. (1980). Measuring Weak Absorptions and Dispersions. *Optics Letters*, *5*(1), 15–17.
18. Bjorklund, G. C., Levenson, M. D., Lenth, W., & Ortiz, C. (1983). Frequency modulation (FM) spectroscopy - Theory of lineshapes and signal-to-noise analysis. *Applied Physics B Photophysics and Laser Chemistry*, *32*(3), 145–152. https://doi.org/10.1007/BF00688820
19. Bruner, A., Mahal, V., Kiryuschev, I., Arie, A., Arbore, M. A., & Fejer, M. M. (1998). Frequency stability at the kilohertz level of a rubidium-locked diode laser at 192114 THz. *Applied Optics*, *37*(27), 6410. https://doi.org/10.1364/ao.37.006410
20. Matthey, R., Gruet, F., Schilt, S., & Mileti, G. (2015). Compact rubidium-stabilized multi-frequency reference source in the 155-μm region. *Optics Letters*, *40*(11), 2576. https://doi.org/10.1364/ol.40.002576
21. Supplee, J. M., Whittaker, E. A., & Lenth, W. (1994). Theoretical description of frequency modulation and wavelength modulation spectroscopy. *Applied Optics*, *33*(27), 6294. https://doi.org/10.1364/ao.33.006294
22. Day, T., Gustafson, E. K., & Byer, R. L. (1992). Sub-Hertz Relative Frequency Stabilization of Two-Diode Laser-Pumped Nd: YAG Lasers Locked to a Fabry-Perot Interferometer. *IEEE Journal of Quantum Electronics*, *28*(4), 1106–1117. https://doi.org/10.1109/3.135234
23. Yeom, K. Microwave Circuit Design: A Practical Approach Using ADS. Pearson, 2015.
24. Razavi, B. RF Microelectronics. Prentice Hall, 2012.
25. S. Ristic, A. Bhardwaj, M. J. Rodwell, L. A. Coldren and L. A. Johansson, "An Optical Phase-Locked Loop Photonic Integrated Circuit," in *Journal of Lightwave Technology*, vol. 28, no. 4, pp. 526-538, Feb.15, 2010, doi: 10.1109/JLT.2009.2030341.
26. Ristic, S., Bhardwaj, A., Rodwell, M. J., Coldren, L. A., & Johansson, L. A. (2009). *Integrated Optical Phase-Locked Loop*. 2–4.
27. M. A. Grant, W. C. Michie, and M. J. Fletcher, “The performance of optical phase-locked loops in the presence of nonnegligible loop propagation delay,” J. Lightw. Technol., vol. LT-5, no. 4, pp. 592–597, Apr. 1987.
28. R. T. Ramos and A. J. Seeds, “Delay, linewidth and bandwidth limitations in optical phase-locked loop design,” Electron. Lett., vol. 3, pp. 389–391, 1990.
29. Hyun-chul Park, *High Speed Integrated Circuits for High Speed Coherent Optical Communications,* PhD thesis, University of California, Santa Barbara, August 2014.

30. Ogata, Katsuhiko. Modern Control Engineering. Pearson, 2009.

Chapter 3. PIC Architecture and Fabrication

3.1 PIC Architecture

Fig. 3.1 shows a micrograph image of the fabricated IPDA lidar seed laser PIC used in this work. It functionally follows the IPDA architecture from [1], but many of the key functions are performed using devices that operate based on different physical principles than their discretely packaged counterparts.

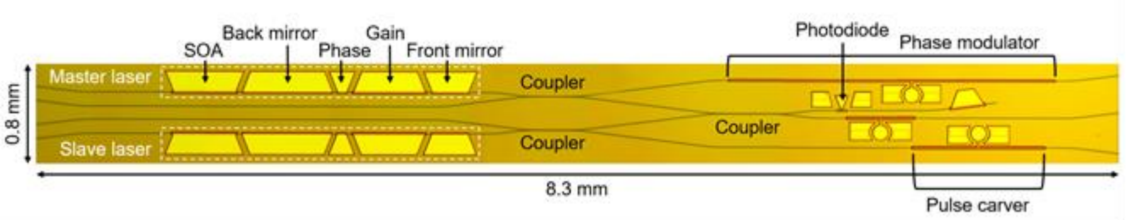

Figure 3.1 Micrograph image of fabricated IPDA lidar PIC.

The PIC consists of two SG-DBR lasers. Each laser has gain, phase, front and back mirror sections, and an absorber back section which can also be used as a power detector or to amplify light output from the back side of the PIC.

The master laser light is split using a directional coupler. Most of the light is directed to a 2.5 mm long waveguide phase modulator which is operated in forward bias in this work. The modulator is driven at 125 MHz and modulation index of π. This frequency and modulation index operating mode selection was a tradeoff between optimal error slope and modulation frequency and strength that could be obtained with the modulator. Light is coupled from the PIC and directly interfaced with the Herriott gas cell reference.

The remaining light is coupled together with a portion of the light from the slave laser to a high-speed photodiode to detect a beat note equal to the offset between the lasers. The beat note is fed to the OPLL for offset frequency locking. An additional larger photodiode allows absorption of any light not absorbed by the beat note detector. In addition, a second path can be used to amplify the coupled light output for use off the PIC.

Most of the light from the slave laser is used for amplified pulse carving on the second main output from the PIC. This is accomplished by an SOA and a custom-made circuit that drives the SOA from reverse bias for absorption to forward bias for amplification. In lab measurement the pulse carver is driven from 0 to 100 mA, which is itself sufficient to obtain more than 40 dB extinction ratio required to avoid power robbing from an EDFA that would follow for transmission.

3.2 Integration Platforms

The Offset Quantum Well (OQW) integration platform was selected for fabrication of the our IPDA lidar PIC. Compared to other platforms such as Selective Area Growth (SAG) [2] and Butt-Joint Growth (BJG) [3], the OQW platform is a fairly simple integration platform for fabrication and the integration of active and passive devices onto the same PIC. The OQW platform allows integration of active devices such as lasers, detectors, amplifiers, and efficient pulse carvers, as well as phase modulators, directional couplers, multimode interference couplers, and Mach Zehnder modulators. While SAG for example allows growth of different waveguide and quantum well structures, the OQW platform is limited to a single active and single passive area. Furthermore, the OQW process requires only one blanket regrowth after laser mirror grating formations. While simple to fabricate, the OQW platform has a few drawbacks such as parasitic reflections at the active/passive interfaces and reduced optical gain due to reduced overlap of the optical mode with the quantum wells. Angling the active-passive interfaces can help reduce the parasitic reflections. The Quantum Well Intermixing (QWI) [4] process was also used. Compared to OQW, QWI has reduced reflections at the active-passive interfaces, greater modal gain due to increased overlap of the optical mode with the quantum wells, and the ability to tailor bandgap regions on the PIC in cases where more than two bandgap regions are required, such as the integration of electro-absorption modulators along with passive and active sections. QWI also allows integration for SG-DBR lasers beside DFB lasers.

3.3 Epitaxial Structure

Tab. 3-1 shows details of the base epitaxial structure for the OQW integration platform in this work.

Layer	Material ($In_xGa_{1-x}As_yP_{1-y}$) (x)	(y)	Strain (ppm)	Thickness (nm)	Doping (cm^{-3})
Cap	1	0	0	170	5E+17 (Zn)
Cap	1	0	0	30	UID
SCH	0.7676	0.504	0	25	UID
Barrier 8x	0.732	0.52	-0.204	8	UID
QW 7x	0.732	0.852	0.912	6.5	UID
Spacer	1	0	0	20	5E+16 (Si)
WG	0.72	0.605	0	350	1E+17 (Si)
Buffer	1	0	0	100	6E+17 (Si)
Buffer	1	0	0	100	8E+17 (Si)
Buffer	1	0	0	800	1E+18 (Si)
Substrate	1	0	0	350,000	3-5E+18 (S)

Table 3-1 Base epi-structure for OQW integration platform.

Initially, 2-inch n-type InP substrates are purchased. All epitaxial layers are grown by MOCVD. After fabrication is completed, the n-type InP wafer is thinned down to approximately 150-200 µm. n-type InP buffer layers reduce the overlap of the optical mode with the highly doped substrate. Following the substrate and buffer layers, we have a 350 nm InGaAsP alloy waveguide structure for vertical confinement of the optical mode (Q=1.3 µm). A thin InP spacer protects the waveguide during the active/passive definition fabrication step. Five quantum wells 6.5 nm and six barriers 8 nm thick are grown and later selectively etched away from the passive regions of the PIC. A separate confinement heterostructure (SCH) layer underneath the cap protects the quantum wells from wet etching. Because the bandgap shifts to longer wavelengths with rising temperatures, we targeted bandgap wavelengths of approximately 1565 nm in the quantum wells. This is slightly below our application wavelength of 1572 nm. After active/passive definition, blanket regrowth by MOCVD of a 2 µm p-type InP cap, a 100 nm highly doped p-type InGaAs contact layer, and 500 nm InP cap completes the epitaxial structure. The 2 µm cap is used to define the waveguide ridge for the lateral confinement of the light. The InGaAs layer serves as a highly conductive contact layer for Ti/Pt/Au metal contacts.

3.4 Fabrication

Table 3-2 shows a list of fabrication steps for the OQW integration platform while Fig. 3.2 shows the simplified process flow.

Step	Description
Active/Passive	Etching of QWs to define the active and passive regions throughout PIC.
Laser Gratings	SG-DBR gratings defined using E-Beam lithography.
Regrowth	Blanket regrowth of upper cladding and contact layer.
Ridge Definition	Dry and wet etch of ridge waveguide for lateral confinement of optical mode.
Passivation Etch	Dopants diffused during regrowth removed to reduce parasitic capacitance.
n-Metal	Top side n-contact hole, via, and ohmic contact.
Isolation	Contact layer etch for p-contact isolation.
BCB and BCB vias	BCB deposition and vias for reduced parasitic capacitance for high-speed devices.
p-Metal	Top side p-contact vias, ohmic contacts, metal pads. n-Metal pads also generated.
Thinning	Sample lapped down to 150-200 µm for cleaving.
Backside Metal	Bottom side n-contact for soldering on carrier.

Table 3-2. Main OQW process fabrication steps.

Illustrated in Fig. 3.2(a) is the initial epi-structure before fabrication begins, right after MOCVD growth. The first fabrication step in the OQW process, shown in Fig. 3.2(b), is the active/passive definition. In this step, the quantum wells and barriers are selectively etched away to define active and passive device regions throughout the sample. First, a 100 nm SiN hard mask is deposited by PECVD followed by photoresist (PR). After photolithography, the hard mask is etched away everywhere with exception to the defined active regions using a $CHF_3/CF_4/O_2$ ICP recipe. The exposed protective InP cap and quantum wells are then etched away with a solution of HCl : H_3PO_4 (1 : 3) and H_2O_2 : H_2SO_4 : H_2O_2 (1 : 1 : 10) respectively. To reduce back reflections from interface discontinuities, the active region interfaces are etched at an angle.

Following the active/passive step, front and back mirror gratings are defined using high resolution e-beam lithography. This is also illustrated in Fig. 3.2(b). After lithography and SiN hard mask etch, the gratings are etched 100 nm using reactive ion etching (RIE) with CH_4 /H_2 /Ar (MHA) gases. Following grating etch, a blanket regrowth is performed by MOCVD, as illustrated in Fig. 3.2(c). This includes the InP cladding, InGaAs contact layer, and an InP protective cap.

The surface ridge waveguides confine the light laterally in the PIC [5]. The ridge waveguides are dry etched using an inductively coupled plasma (ICP) recipe containing $Cl_2/H_2/Ar$ gases in the [110] direction. This prevents undercutting of the ridge during crystallographic wet etching of the surface ridge waveguide [6]. The remaining InP cladding is cleaned up using a wet etching solution of HCl : H_3PO_4 (1 : 3) for smooth side walls that terminates on the InGaAsP waveguide. This is illustrated in Fig. 2.3(d).

Previously during regrowth, the InP cladding was doped with Zn. These p-type dopants tend to diffuse into the InGaAsP waveguide core. This increases the effective area of the PIN diode and can therefore degrade the performance of high-speed devices due to increased parasitic capacitance. The problem is addressed by etching 100 nm into the conductive quantum wells and waveguide core to remove dopants in regions where top side contacts will later be deposited. The hard mask from the waveguide definition step protects the ridge waveguide from etching while a photoresist mask is used to define the etching region. The etching is accomplished using RIE and MHA gases. This step is illustrated in Fig. 2.3(e).

PIC devices were then isolated by etching away the conductive p+ InGaAs contact layer in select regions. This is accomplished using a semi-self aligned (SSA) process step. First, the sample is coated with 200 nm SiN hard mask. Thick photoresist is then deposited, exposed, and partially developed above the isolation regions. The remaining photoresist is gradually etched away using an O_2 plasma until the SiN hard mask over the protective InP ridge is visible. The hard mask is etched away using RIE and CF_4/O_2 gases. The exposed InP cap layer and InGaAs contact layer are then etched using $HCl : H_3PO_4$ (1 : 3) and $H_2SO_4 : H_2O_2 : H_2O$ (1 : 1 : 10) solutions respectively. This step is illustrated in Fig. 2.3(f).

For probe testing, top side n-metal contacts are deposited throughout the sample. After n-hole pattern lithography and hard mask etching using ICP, the sample is etched down to the substrate using ICP and $Cl_2/H_2/Ar$ gases. N-metal lithography is performed on the sample for deposition of Ni/AuGe/Ni/Au (5 nm/100 nm/20 nm/300 nm) metals by e-beam evaporation. A standard liftoff process is used to remove the excess metal. The sample is then annealed in forming gas at 425°C to improve contact resistivity and ductility. This step is illustrated in Fig. 2.3(g).

To improve the opto-electronic bandwidth of the PIC beat note detectors, we applied a Benzocyclobutene (BCB) based polymer dielectric. Initially a 200 nm SiN hard mask is deposited for good BCB adhesion. BCB deposition is similar to a negative photoresist. Initially, BCB is spun on the entire sample. Lithography is performed to define the BCB patterns. Elsewhere, BCB is removed using puddle development on spinners. Finally, the remaining BCB is cured in N_2 gas for 4 hours at 250°C. This step is illustrated in Fig. 2.3(h).

After BCB deposition, the sample is ready for etching BCB vias. Initially a 100 nm SiN hard mask is deposited for good p-metal adhesion. The vias are defined in lithography where a critical alignment is required to ensure via placement over the ridge. After exposure and development, the hard mask and BCB are etched away using ICP $CF_4 : CHF_3$ and $CF_4 : O_2$ gases respectively. After coating of the inner BCB walls with SiN, a second critical alignment is performed, and a final hard mask etch is applied for p-metal via opening in the BCB. This step is illustrated in Fig. 2.3(i).

Vias are then also defined in lithography for the other sample devices and the hard mask is etched away using RIE with CF_4/O_2 gases. A sacrificial wet etch of the exposed InP cap layer is now performed over the entire sample using a solution of HCl : H_3PO_4 (1 : 3) for exposure of the InGaAs contact layer. This is illustrated in Fig. 3.2(j).

P contacts can now be formed using a standard liftoff process. Ti/Pt/Au (20 nm/40 nm/500 nm) metals are deposited by e-beam evaporation and then annealed in forming gas at 390°C for 30s. This is illustrated in Fig. 3.2(k).

In post processing, the samples are lapped down to 150-200 um thickness. Metal is then deposited on the bottom side of the PIC using e-beam evaporation for soldering onto electronic carriers. Individual PICs and die are cleaved, and anti-reflection (AR) coating is applied where necessary. We mostly relied on an external vendor for the cleaving and AR coating services. Individual PICs and test structures are mounted on electronic AlN or Alumina carriers which contain patterns for multi-probe placement and wire bonding. A stencil is used to apply a thin layer of solder paste on the carriers. PICs are placed down onto the solder paste using pick-and-place machines. Hot plates are then used for solder reflow.

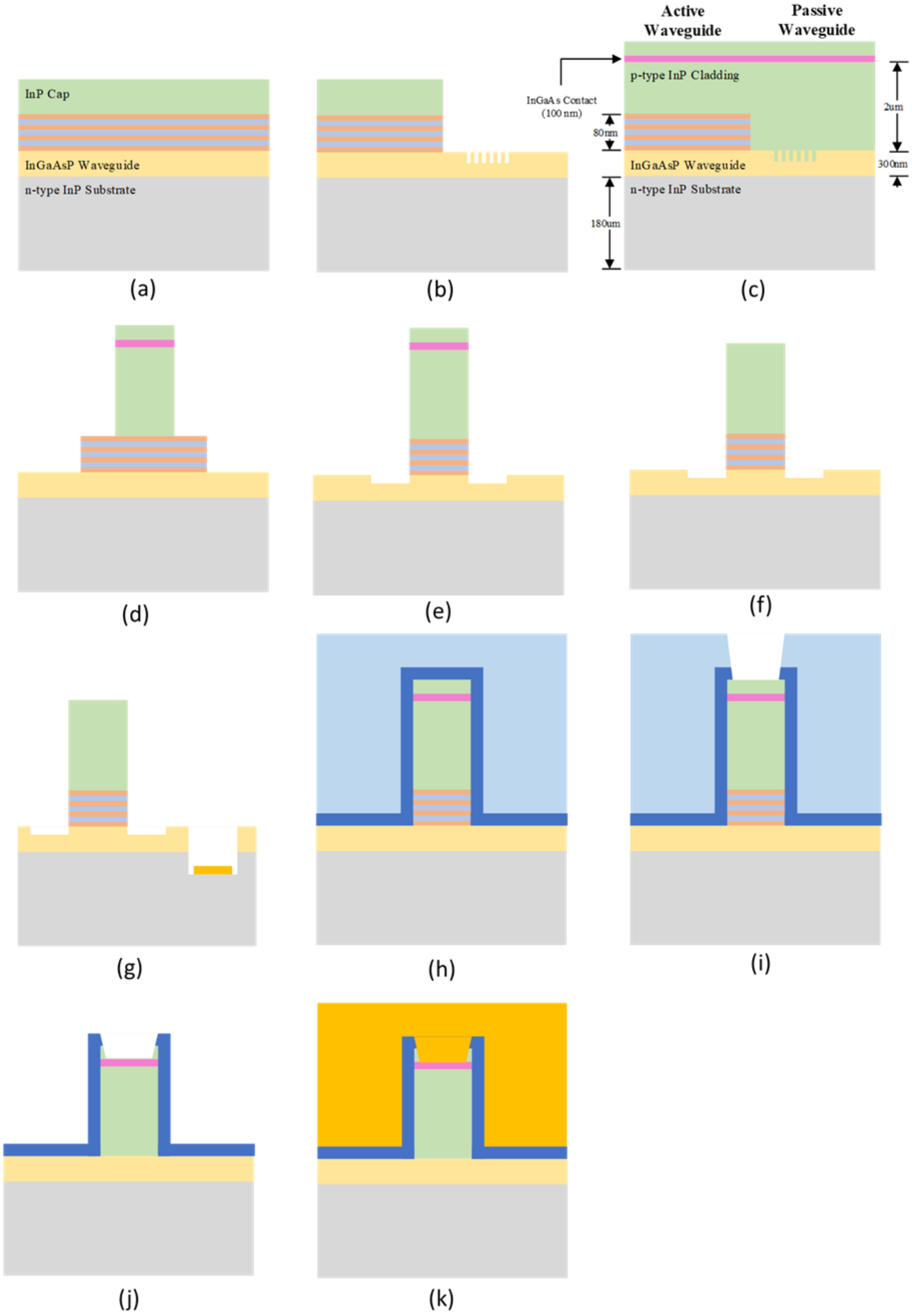

Figure 3.2 (a) epitaxial structure; (b) active/passive; (c) regrowth; (d) ridge waveguide definition; (e) passivation; (f) isolation; (g) n-metal; (h) BCB deposition; (i) BCB vias; (j) p-metal vias; (k) p-metal

References

1. Numata, K., Chen, J. R., & Wu, S. T. (2012). Precision and fast wavelength tuning of a dynamically phase-locked widely-tunable laser. *Optics Express*, *20*(13), 14234. https://doi.org/10.1364/oe.20.014234
2. Sasaki, T., Yamaguchi, M., & Kitamura, M. (1994). Monolithically integrated multi-wavelength MQW-DBR laser diodes fabricated by selective metalorganic vapor phase epitaxy. *Journal of Crystal Growth*, *145*(1–4), 846–851. https://doi.org/10.1016/0022-0248(94)91152-5
3. Skogen, E. J., Barton, J. S., Denbaars, S. P., & Coldren, L. A. (2002). A quantum-well-intermixing process for wavelength-agile photonic integrated circuits. *IEEE Journal on Selected Topics in Quantum Electronics*, *8*(4), 863–869. https://doi.org/10.1109/JSTQE.2002.800849
4. Skogen, E. J., Barton, J. S., Denbaars, S. P., & Coldren, L. A. (2002). A quantum-well-intermixing process for wavelength-agile photonic integrated circuits. *IEEE Journal on Selected Topics in Quantum Electronics*, *8*(4), 863–869. https://doi.org/10.1109/JSTQE.2002.800849
5. L. A. Coldren and S. W. Corzine, *Diode Laser and Photonics Integrated Circuit*s. New York: Wiley-Interscinece (1995).
6. Eliáš, P., Kostič, I., & Hasenöhrl, S. (2002). Polar diagram of wet-etched (100) InP. Conference Proceedings - International Conference on Indium Phosphide and Related Materials, 100, 229–231. https://doi.org/10.1109/iciprm.2002.1014334

Chapter 4. PIC Device Performances

4.1 SG-DBR Lasers

4.1.1 Introduction

SG-DBR lasers make use of sampled gratings to obtain periodic reflectivity peaks that have a comb like structure [1,2]. The front and back mirror gratings are misaligned with respect to each other. Only a single pair of mirror peaks overlaps at any one time. By properly designing the spacing between the reflectivity peaks, tuning over as much as 40 nm is possible. The sliding of the mirrors with respect to each other is very much like a vernier scale. To ensure continuous tunability, the spacing between the mirrors should be below the tuning range of a single mirror on its own which is approximately 8 nm [1].

Fig. 4.1 shows simulation results of the front and back SG-DBR mirrors for the SG-DBR lasers used in this work. Effective indices were obtained using mode simulations in Lumerical MODE for a variety of etch depths, while the sampled grating mirror responses were obtained using the Transfer Matrix Method (TMM) in Matlab. The SG-DBR specifications for both mirrors are provided in Tab. 4-1. Due to limitations in the minimum resolution of the e-beam lithography system, a JEOL JBX-6300FS, an asymmetric grating period was used to ensure that the Bragg wavelength fell near 1572 nm. Symmetric gratings for the same grating period that was used in this design resulted in a Bragg wavelength near 1600 nm which significantly degraded the tuning performance in our generation 1 lasers.

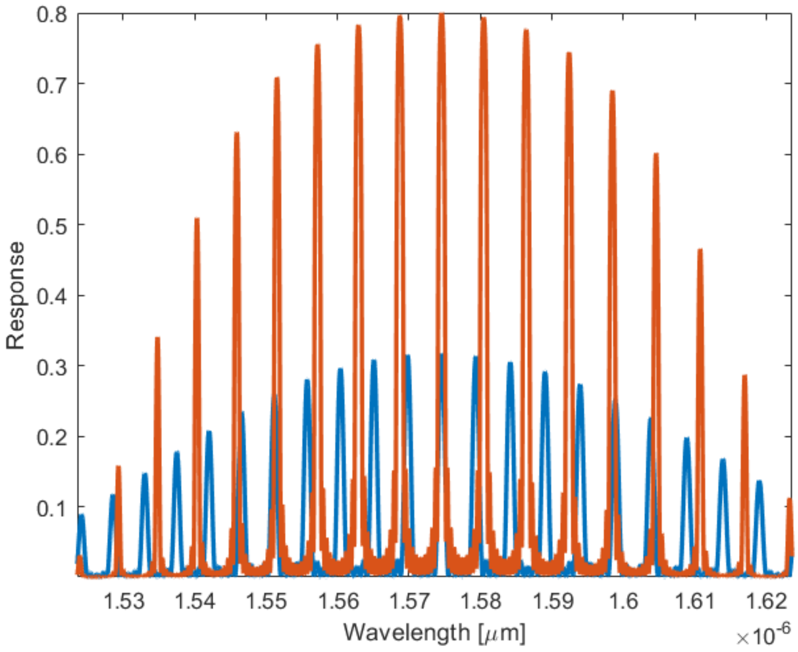

Figure 4.1 SG-DBR front and back mirror reflectivity spectra.

Specification	Front Mirror	Back Mirror
Grating Period Asymmetry	244 nm 120/124 nm	244 nm 120/124 nm
Burst Length	4.148 µm	6.1 µm
Sampling Length	68.712 µm	61.34 µm
# of Bursts	5	12
Etch Depth	100 nm	100 nm

Table 4-1 SG-DBR design specifications.

The SG-DBR laser was selected for both master and slave lasers mainly due to its broad band tunability. Wavelength overlap with the CO_2 absorption line is critical. We found that with proper design and grating fabrication of the SG-DBR mirrors this was easily attainable and so would improve PIC yield. DFB lasers were also designed and are attractive due to their generally narrower linewidth but due to process variability in the cleanroom and to ensure good PIC yields, most PICs utilized master and slave SG-DBR lasers. Furthermore, unlike DFB lasers, SG-DBR lasers do not suffer from phase reversal due to contention between thermal and carrier effects around 0.1-1 MHz [3,4]. This allows use of SG-DBR lasers in wideband OPLLs [5,6].

Also, to reduce amplified reflections back into the laser, some PICs did not have SOAs following the laser. These generally performed the best with respect to tunability and SMSR, although suffered from power variability over the mode-hop free tuning range using the phase section only.

4.1.2 LIV Curves

Fig. 4.2 shows the LIV curves for a laser with no SOA immediately following the front mirror at different temperatures. The laser output power was detected using another SOA for pulse generation purposes that was approximately 4 mm away. Nevertheless, the output power at 100 mA was 5 mW at a 15°C stage temperature.

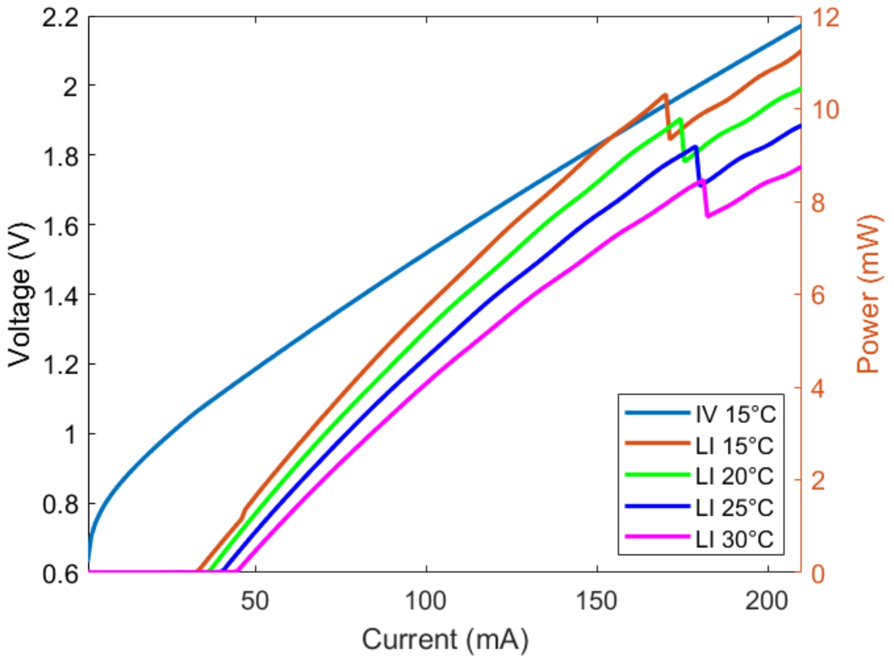

Figure 4.2 LIV curves for different stage temperatures.

As expected, the threshold current drops and slope efficiency rises at lower stage temperatures. Fig. 4.2 shows that the threshold current varied between 30-50 mA over 15°C change to the stage temperature. The slope efficiency was a bit low. At 20°C it was 0.06 W/A. To maintain consistency in output powers, a detector on the back side of the laser could be used to adjust the gain section current appropriately. This situation may arise should the laser have to operate over a wide temperature range.

4.1.3 Tunability and SMSR

Fig. 4.3 shows overlapped lasing spectra of the SG-DBR laser displayed on an OSA. The 40 nm tuning range was obtained by varying the current bias into the SG-DBR front and back mirrors, and phase section. Tuning SG-DBR lasers can be quickly accomplished by sweeping the current into the front mirror. This results in super-mode hopping across the 40 nm tuning range. The effective index in a mirror section varies with respect to carrier density according to Eq. 4.1.

$$\frac{\partial \bar{n}}{\partial N} \approx -\Gamma_{xy} 10^{-20} cm^3 \qquad (4.1)$$

Γ is the transverse confinement. The Bragg wavelength of the grating mirrors varies according to Eq. 4.2.

$$\frac{\Delta\lambda_g}{\lambda_g} = \frac{\Delta\bar{n}}{\bar{n}_{DBR}} \qquad (4.2)$$

Equation 4.2 shows that increasing the current density into the mirror blue shifts the Bragg wavelength. Because the separation between front mirror reflectivity peaks is slightly reduced compared to the back mirror, good initial alignment between the two mirrors will result in super-mode hopping towards lower wavelengths when current is injected into the front mirror.

Strong misalignment of the mirrors can reverse the super mode hopping direction. Once the desired wavelength is within a few nanometers below the lasing super mode, minor adjustments to the back and front mirror can tune the SG-DBR to the desired wavelength. The tuning process should begin with a few milliamps in the phase section as it is later used in feedback. Minor adjustments to the phase section or mirror currents can optimize the mode overlap with the mirror peaks. This optimizes the mode hop-free tuning range using the phase section only and provides optimal SMSR performance.

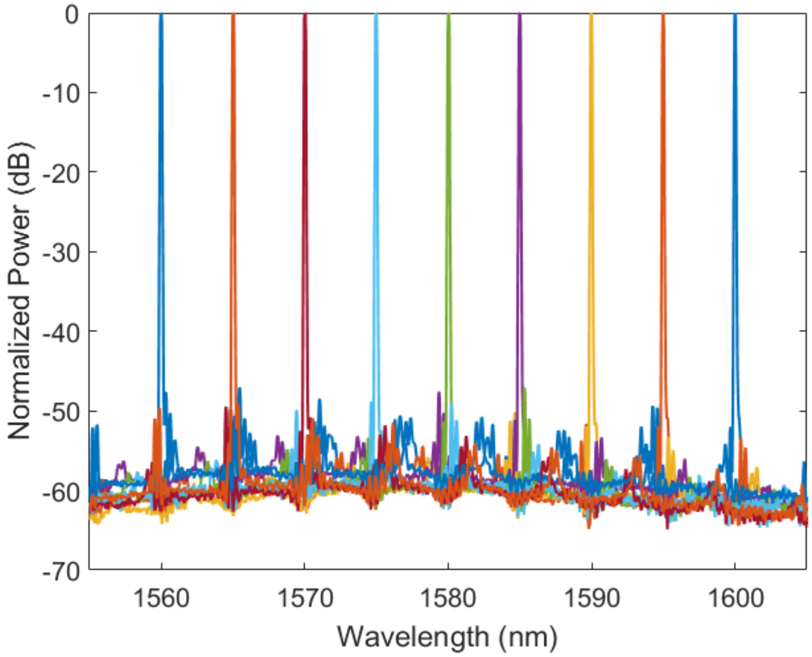

Figure 4.3 Overlapped SG-DBR spectra showing 40 nm tuning range.

Fig. 4.4 and Fig. 4.5 show 50 dB side-mode and super-mode suppression ratio of the adjacent longitudinal side-modes and super-modes when the SG-DBR laser was tuned to near the CO_2 absorption line at 1572 nm. Also visible is the close-in broad band noise floor. Both performance metrics can be improved by increasing the current drive into the gain section as the additional carriers are radiatively stimulated most intensely with the strongest longitudinal mode. As much as 55 dB SMSR was obtained in the introductory design.

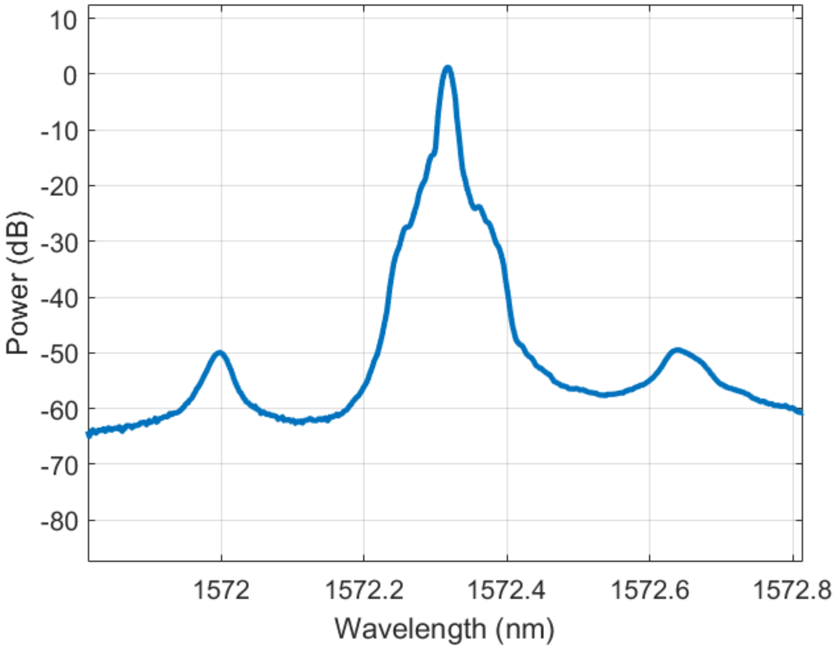

Figure 4.4 SG-DBR SMSR at 1572 nm.

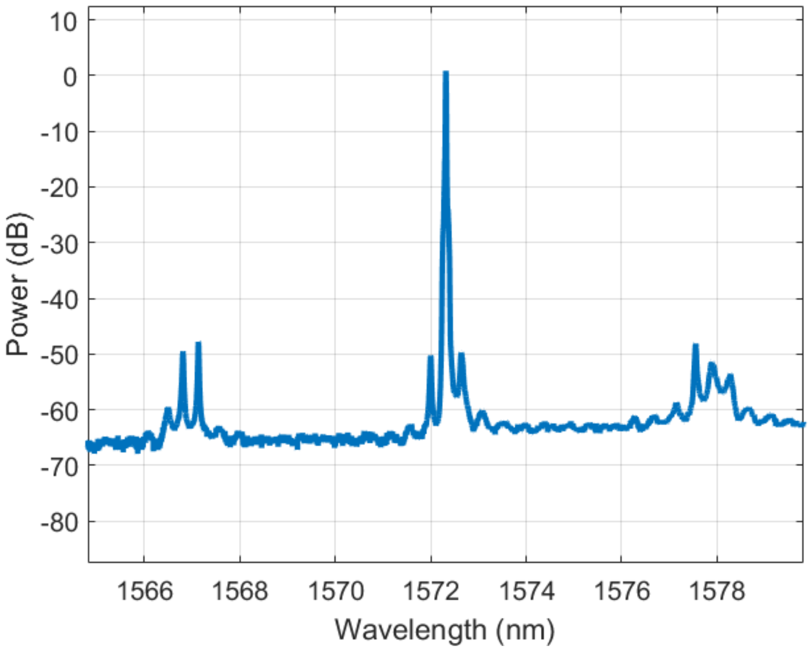

Figure 4.5 SG-DBR super-mode SR near 1572 nm.

Strong undesired modes and super-modes in the SG-DBR degrade the detection sensitivity. A strong second mode has a flattening effect on the DC transmission signal from the gas cell and increases the detector shot noise too. Before a system relying on closed loop feedback is enabled, the gas transmission can be used to tune the master laser. The reduction in dynamic range of that DC signal limits the system's capability to align the laser accurately and quickly with the gas absorption line. This can be exemplified by considering the on-line to off-line extinction ratio when a second off-line mode accompanies the main lasing mode as well as arbitrarily assuming the signal strength is halved at the peak absorption wavelength.

Eq. 4.3 compares these two cases:

$$\frac{P_1}{\frac{P_1}{2}} = 2 > \frac{P_2+P_1}{P2+\frac{P1}{2}} = \frac{P_2+P_1}{\frac{(2P_2+P_1)}{2}} \tag{4.3}$$

For best operation it is desirable to have SMSR greater the 45 dB.

In both the frequency modulation stabilization and OPLL feedback loops we rely on current injection into the SG-DBR phase section for fine tuning of the laser wavelength. Fig. 4.6 shows the fine tuning of the lasing mode over a 4 mA range using current injection into the phase section only at a 20°C stage temperature.

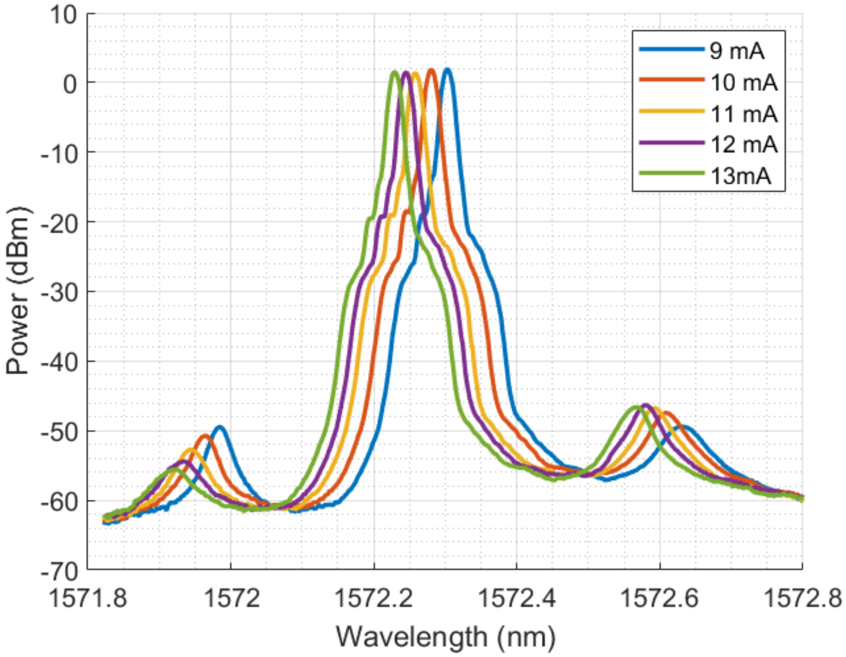

Figure 4.6 SG-DBR wavelength fine tuning using the phase section at 20°C.

The side and super mode suppression ratio over this range remains close to 50 dB. The mirrors were tuned for optimal side mode suppression at a current of 11 mA, the middle of the continuous phase section tuning current range. The tuning range using the phase section is ~ 0.1 nm / 12 GHz over this range. The tuning rate is therefore estimated to be ~ 2.5 GHz / mA.

Although fast tuning is possible with modulation of the SG-DBR phase section current, significant changes in ambient temperature can shift the SG-DBR lasing wavelength beyond the mode hop free range obtainable using phase section tuning only. Drift due to significant changes in ambient temperature can be neutralized to some degree with slow feedback control of the SG-DBR laser stage temperature. By locking the laser wavelength using temperature, the SG-DBR mirrors jointly shift to lower or higher wavelengths with temperature at a rate of +0.1 nm / °C. Furthermore, since the tuning is mode hop free over a wide tuning range, the effective cavity length also varies accordingly in size. We can estimate the change in size since we know the effective cavity length is an integer multiple of the lasing wavelength. For example, assuming a 10°C change in temperature and an initial effective length of 750 um and lasing wavelength of 1.55 um, the modal number can be obtained using Eq. 4.4.

$$\frac{m\lambda}{2} = Leff \qquad (4.4)$$

This gives m = 970. The change in effective length over 10°C can now be determined from Eq. 4.5 since we know we get 1 nm shift over a 10°C temperature change.

$$\frac{\Delta L_{eff}}{°C} = \frac{970*1\ nm}{2*10\ °C} \approx 50\,\frac{nm}{°C} \qquad (4.5)$$

Fig. 4.7 illustrates mode hop free tuning using the thermal stage temperature from 10°C to 30°C. Current injection into all the SG-DBR sections remained the same, although the coupling lensed fiber was realigned to detect similar output powers.

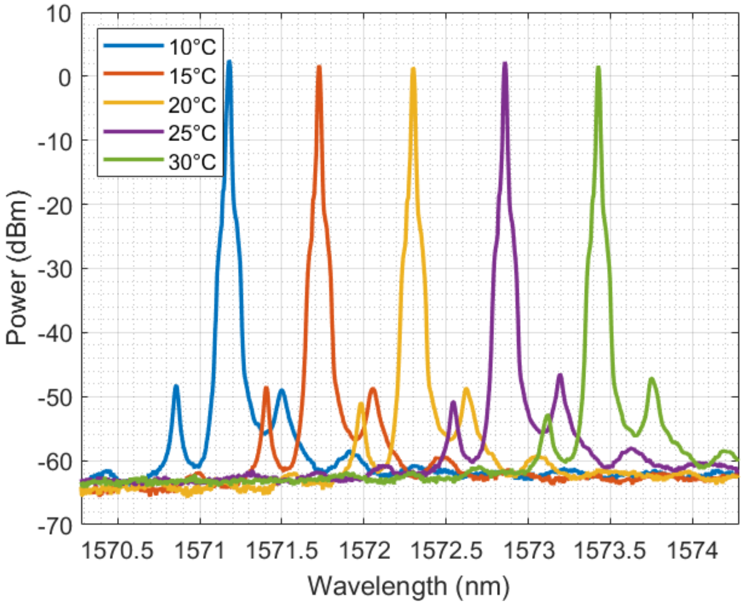

Figure 4.7 Mode hop free thermal tuning of the SG-DBR.

Fast tuning of the phase section at stage temperatures at the tuning edges of Fig. 4.7 are illustrated in Fig. 4.8 at 10°C and 30°C respectively over a 4 mA range. The side mode suppression ratio in these cases was better than 45 dB, showing that the SG-DBR requires no changes in the mirror setting over a wide temperature range and is therefore suitable for operation in harsh environments where the temperature might fluctuate significantly.

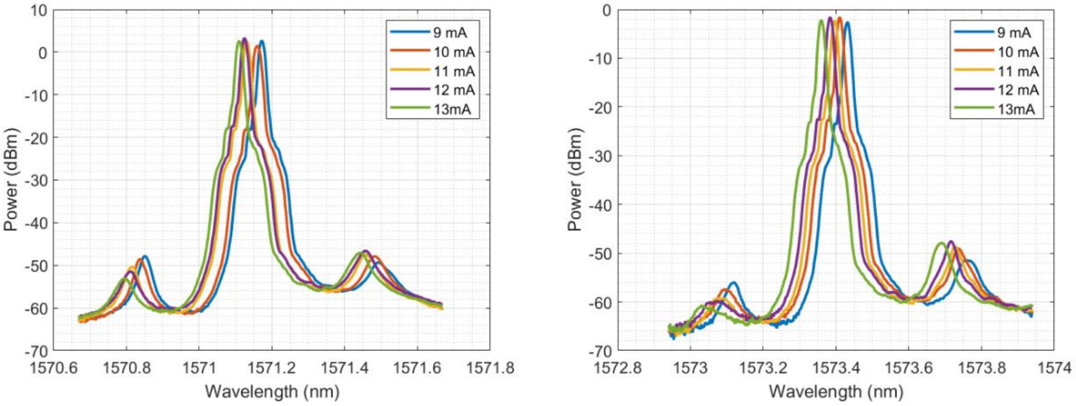

Figure 4.8 Fast tuning of the SG-DBR at 10°C and 30°C with no changes to the mirror settings.

4.1.4 Linewidth

Fig. 4.9 shows the SG-DBR linewidth measurement results. The full width half maximum (FWHM) is 5 MHz. In the self-heterodyne technique, the FWHM is twice the actual laser linewidth since the laser is convolved with a delayed version of itself. The actual SG-DBR linewidth is thus 2.5 MHz.

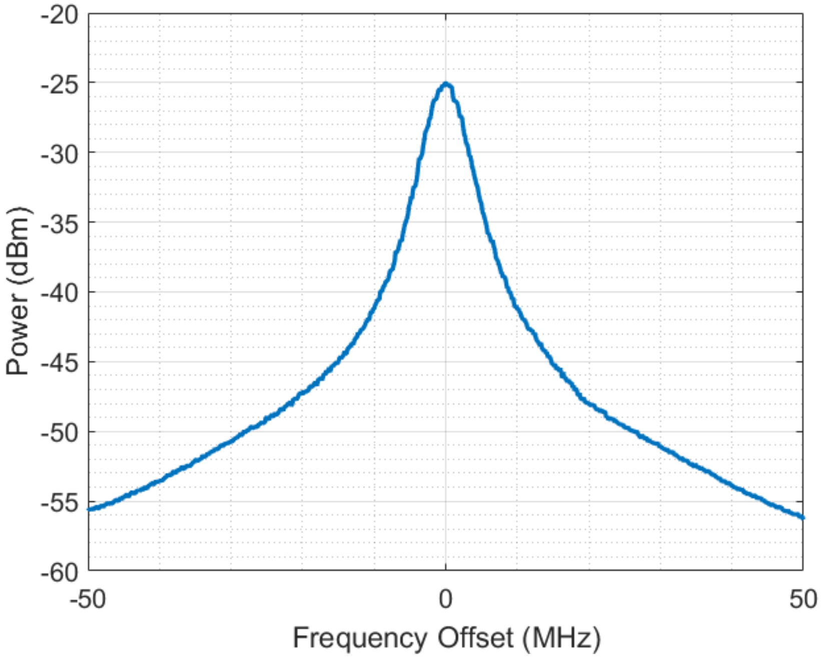

Figure 4.9 SG-DBR self-heterodyne linewidth measurement.

4.2 High-Speed Detector

As previously mentioned, there are several benefits to sampling the sides of the absorption line. Because CO_2 has diurnal vertical transport, sampling at sides of the line where the absorption is due to pressure broadened CO_2 molecules, helps maintain uniform measurement sensitivity in the lower troposphere. Furthermore, atmospheric weighting functions can be calculated at two to three heights by sampling the absorption line at the sides of the line [7]. Finally, instrument wavelength offsets can also be solved for by using a line fitting process.

We are interested in sampling wavelengths at offset frequencies up to ±15 GHz. We fabricated quantum well PIN waveguide photodiodes ranging in size from 30-50 µm. Furthermore, to reduce device parasitic capacitances, BCB was deposited beneath the p-metal contacts. Fig. 4-10 shows the normalized opto-electronic bandwidth measured with a light wave component analyzer for a -2.5V reverse bias across the photodiode. PIN photodiodes normally show improved quantum efficiency and reduced parasitic capacitances at increased reverse bias levels although this increases the depletion region width and transit time too.

The bandwidth specification of 15 GHz was met but there was no discernable variability in the bandwidth of the different detectors sized at 30, 40, and 50 µm. This is perhaps due to the similar pad sizes.

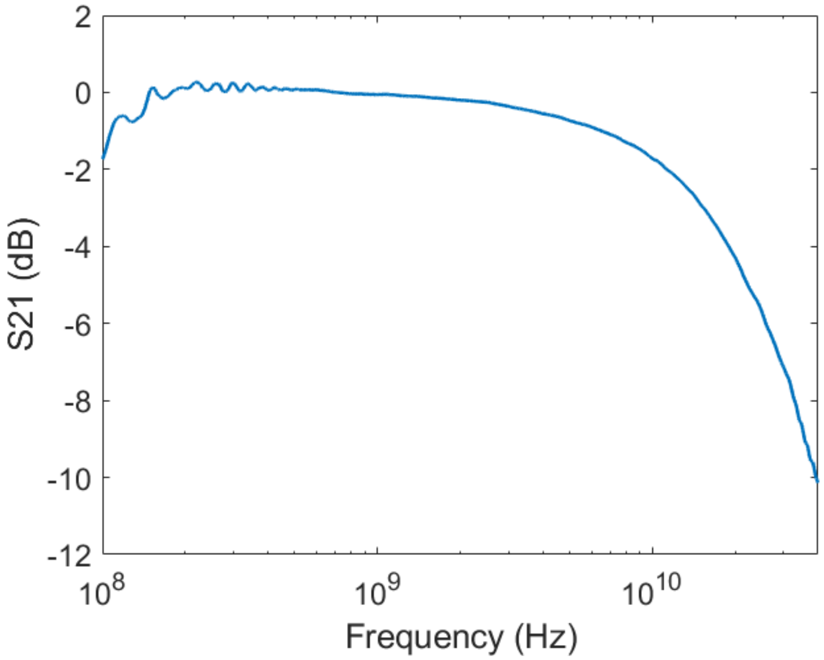

Figure 4.10 Integrated PIN photodiode bandwidth with BCB.

4.3 Semiconductor Optical Amplifiers

4.3.1 SOA Gain and Saturation

Semiconductor optical amplifiers (SOAs) can be strategically placed throughout a PIC to compensate for chip and coupling losses, in order to meet PIC output power requirements. Furthermore, since SOAs have input dependent gain, they can be used to level the SG-DBR output power [8]. In SG-DBR lasers, noticeable variations in the output power are possible over a few GHz of tuning. Fig. 6.2 shows the gas cell transmission of a CO_2 absorption line as the phase section current is swept. It was determined that the mode-hop-free tuning sensitivity of the SG-DBR phase section was ~ 3 GHz/mA. The noticeable variation in detected power causes errors in the mapping of the absorption line, and if not addressed with gain leveling using an SOA, would require post processing to compensate for this variation.

Fig. 4.11 shows the input power dependent gain and saturation of a 500 µm SOA as a function of the bias current. The curves were obtained by integrating two series SOAs. The first SOA is reverse biased to detect the input power from an off-chip source coupled using a lensed fiber. After that, the SOA bias current is swept up to 300 mA while the second SOA is reverse biased for absorption. The responsivity is assumed to be 1A/W.

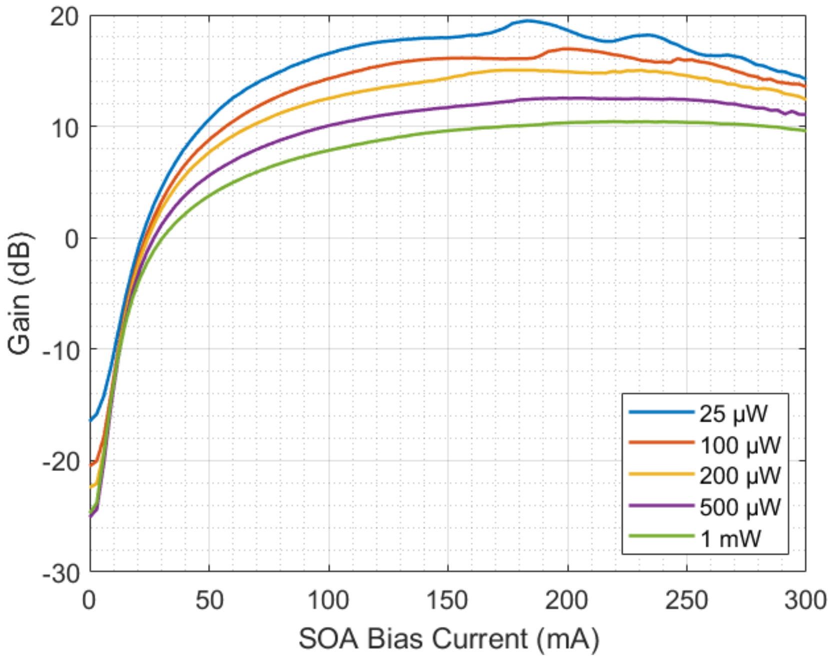

Figure 4.11 SOA input dependent gain and saturation for different bias currents.

18 dB gain is achieved for 25 µW input power at 150 mA bias but only 9 dB for 1 mW of input power. Most of the gain using the SOA is obtained between transparency and 100 mA. The SOA gain saturates from 150 to 250 mA, corresponding to lower and higher input powers

respectively. For greater currents, gain roll off due to heating occurs. Also noticeable is a large gain ripple for the cases with lower input powers. This is perhaps due to etalon effects that are more pronounced at lower input powers due to the increased saturation length of the SOA. At high input powers, most available carriers are coherently stimulated. It is thus critical to minimize reflections in the PIC to reduce ripple and maintain consistent operation. Furthermore, we found that PICs with integrated SOAs had significantly poorer tuning performance and were occasionally multimode [9]. Facet reflections should be kept below 10^{-4} to avoid such issues [10]. Strategic placement of the SOAs on the PIC is required to prevent use of erbium doped fiber amplifiers with the gas cell. To obtain high gain saturation, dual SOAs can be used as well as tapering of the waveguide and active region as the saturation is limited by the small cross sections of the waveguide [11]. Finally, we can see that we can carefully select an optimal SOA bias point to equalize the gain due to carrier absorption tuning losses in the SG-DBR phase section.

4.4 Phase Modulator Efficiency and RAM

4.4.1 Introduction to InP Phase Modulators

There are a several physical effects that can be leveraged in InP based integration platforms for construction of phase modulators. The optimal choice will be influenced by system requirements and these include the modulation efficiency, bandwidth, residual amplitude modulation, size, and power consumption. In frequency stabilization or spectroscopy schemes, impure phase modulation that is accompanied by strong amplitude modulation can significantly deteriorate system performance [12].

InP based amplitude and phase modulators integrated beside a laser diode have been demonstrated to have high bandwidth and efficiency as well as tailorable chirp to counteract chirp induced on the laser [13].

The phase shifting occurs due to modulation of the phase constant of the propagating optical plane wave which is a function of effective optical index in the waveguide. The contributions from physical effects in the modulator, from both electro-optic and carrier-based effects, can be combined to obtain the total change in effective index.

Phase modulator efficiency can be analyzed by construction and analysis of a Mach-Zehnder modulator interferometer. A plot of the output power as a function of the bias on the modulator can be generated this way. When this information is combined with the absorption data in the modulator, one can use Eq. 4.6 and Eq. 4.7 to determine the phase modulator efficiency in reverse bias operation [14]. Here $\Delta\alpha$ and $\Delta\beta$ are the power attenuation and phase constants respectively, L is the interaction length, $SR_{in}=(P1/P2)_{in}$ and $SR_{out} = (P1/P2)_{out}$ are the input and output power splitting ratios, V_1 and V_2 are the potentials across the MZM arms, and φ is a phase shift introduced into one of the arms.

$$E(V_1, V_2) = E_i\left[\sqrt{SR_{in}SR_{out}}\exp\left\{-\left[\frac{\Delta\alpha(V_1)}{2} + j\Delta\beta(V_1)\right]L\right\} + \exp\left(-\left\{\frac{\Delta\alpha(V_2)}{2} + j[\Delta\beta(V_2) + \varphi]\right\}L\right)\right] \quad (4.6)$$

$$E_i = \frac{E_0}{\sqrt{(1+SR_{in})(1+SR_{out})}} \quad (4.7)$$

Absorption information can be obtained my measuring the photocurrent as a function of bias on the arm. The modal absorption can then be obtained using Eq. 4.8.

$$\alpha = -\frac{1}{L}\ln\left(1 - \frac{I_{pc}(V)\hbar\omega}{qP_{in}}\right) \tag{4.8}$$

Changes in the refractive index due to electric field effects include the linear electro-optic Pockels effect and the electro-refractive effect due to Franz-Keldysh absorption. Eq. 4.9 shows the change in index due to the Pockels effect for light propagating in the [110] or [$\bar{1}$10] directions in the crystal.

$$\Delta n = \frac{n^3 r_{41} E}{2} \tag{4.9}$$

The coefficient r41 for a variety of InGaAsP compositions can be obtained from [15].

In semiconductors, application of an electric field also induces a change in the optical absorption which is referred to as the Franz-Keldysh effect. The Franz-Keldysh effect on the absorption edge appears as a shift of this edge to lower energies [16]. The change in refractive index due to change in absorption edge can be quantified using the Kramers-Kronig transform.

The change in refractive index due to this effect turns out to have a quadratic electric field relationship as expressed in Eq. 4.10. As the transmission wavelength approaches the material bandgap energy, the Kerr coefficient strengthens.

$$\Delta n_{LEO} = \frac{n^3 R_{kerr} E^2}{2} \tag{4.10}$$

In reverse bias, one must also consider band-filling effects. As carriers occupy energies in the band, holes require more energy to transition into the conduction band. Consequently, the absorption is reduced. In n-type semiconductors where the carriers are depleted in reverse bias the effect is reversed and referred to band-emptying. The Kramers-Kronig relations can then be used to obtain the corresponding changes in the refractive index.

In this work modulation of the light phase is accomplished using carrier injection into the waveguide in forward bias. This is known as the plasma effect. This effect is due to absorption of free carriers in the conduction or valence bands of the semiconductor and results in a decrease in the refractive index. As these transitions involve smaller energies, this effect is more significant at wavelengths that are longer than the bandgap energy. The plasma dispersion effect is significantly more efficient than electric field-based effects and is not polarization dependent [17]. Eq. 4.11 shows the relationship between the hole and electron carrier densities and the change in refractive index,

$$\Delta n(x) = -\frac{\lambda^2 q^2}{8\pi^2 c^2 n \epsilon_0}\left(\frac{N_e}{m_e} + \frac{N_h}{m_h}\right) \tag{4.11}$$

λ is the wavelength in vacuum, q is the electron charge, c is the speed of light, n is the refractive index, ϵ_0 is the vacuum dielectric constant, N_e and N_h are the electron and hole carrier densities, and m_e and m_h are the electron and hole effective masses respectively [18]. The injected carrier density into the waveguide is expressed in Eq. 4.12,

$$N = \frac{J\tau}{qd} \tag{4.12}$$

J is the current density, τ is the carrier lifetimes, and d is the waveguide core thickness. The phase modulator bandwidth can be limited by the carrier lifetime or the RC response time.

Generally, the cumulative effects can be combined to determine the change in refractive index and then the corresponding phase change in the modulator can be expressed as Eq. 4.13.

$$\Delta\varphi = \frac{2\pi\Delta n_{eff}L}{\lambda} \tag{4.13}$$

4.4.2 Phase Modulator RAM

Implementing a frequency modulation stabilization scheme requires a phase modulator capable of very pure phase modulation performance and low loss. Typical telecom L-band lithium niobate specifications are illustrated in Tab. 4-2. It is worth noting that these high-performance modulators have loss of about 3 dB, are polarization dependent and as such require polarization maintaining hardware, have a $V\pi$ around 3.5V, and demonstrate significantly superior phase modulation purity.

Parameter	Symbol	Condition	Min	Typ.	Max	Unit
Crystal		Lithium Niobate X-Cut				
Waveguide Process		Ti Diffusion				
Insertion Loss	IL	Without Optical Connectors		2.7	3.5	dB
Polarization Dependent Loss	PDL			5	8	dB
Optical Return Loss	ORL		-40	-45		dB
Vπ RF at 50 kHz				3.5		V
RF Input Impedance	Zin-RF			10,000		Ω
Operating Wavelength	λ		1530	1550	1625	nm

Table 4.2 Lithium niobate phase modulator specifications.

As mentioned earlier, the residual amplitude modulation (RAM) performance of phase modulators has critical implications on the performance of frequency modulation stabilization schemes. Time dependent RAM can be expressed according to Eq. 4.14 where *V(t)* is the time dependent voltage applied to the modulator about the bias point.

$$P(t) = P_o + \varepsilon V(t) \tag{4.14}$$

Peak to peak RAM can be expressed using Eq. 4.15.

$$RAM_{dB} = 10\log\left(\frac{\varepsilon V_{pp}}{P_o}\right) \tag{4.15}$$

RAM is induced in lithium niobate modulators due to reflections at the input and output facets. The modulator acts as a weak optical resonator. When a voltage is applied to the modulator fringe like patterns result due to the change in effective length of the cavity. In addition, the incoming fundamental mode can be coupled into an electro-optically induced secondary mode beneath the electrodes. Amplitude modulation occurs as the two modes interfere as they travel along the waveguide at different velocities and then couple into the optical output fiber [19]. RAM levels for lithium niobate phase modulators can be as low as 0.04%.

Residual amplitude modulation can limit the sensitivity in laser frequency modulation stabilization schemes. Due to interference effects in electro-optic phase modulators, the frequency dependent fringe-like patterns modulate the output intensity [20]. Such a source of RAM manifests itself as a background signal that limits sensitivity, although noise due to this type of RAM can be minimized by adjusting the relative phase of the local oscillator and signal at the phase detector [20]. Furthermore, this phase adjustment is independent of the laser frequency. There are nevertheless sources of RAM that are frequency independent and do not always have a well-defined phase behavior. These can be mitigated to some degree by addressing both frequency dependent and independent RAM.

Time-varying RAM arising from multipath interference, polarization misalignment, temperature variations, vibrations, and other sources, particularly in the phase modulator, can limit detection sensitivity [21].

In frequency modulation spectroscopy demonstrated in [22], a servo control scheme is used to obtain shot-noise limited detection. The servo control addresses RAM due to temperature dependent birefringence in the optical phase modulator crystal. In this case, shot noise detection is accomplished by actively rotating one of the transverse principal crystal axes to align with an input or output polarizer. That way, the transmitted light does not see the crystal birefringence. The rotation is done by detecting the in-phase component and using a servo integrator amplifier and lead/lag amplifier to further increase the low frequency gain.

4.4.3 Efficiency and RAM Measurement

Here we will discuss a sensitive measurement technique for estimation of phase modulator efficiency and RAM that relies on heterodyne conversion of optical modulations to the RF domain and demodulation with an RF IQ receiver. The setup was adapted from [23] which relied on bulk optics to couple light into a GaAs/AlGaAs double heterostructure phase modulator. A schematic of the complete test setup is illustrated in Fig. 4.12.

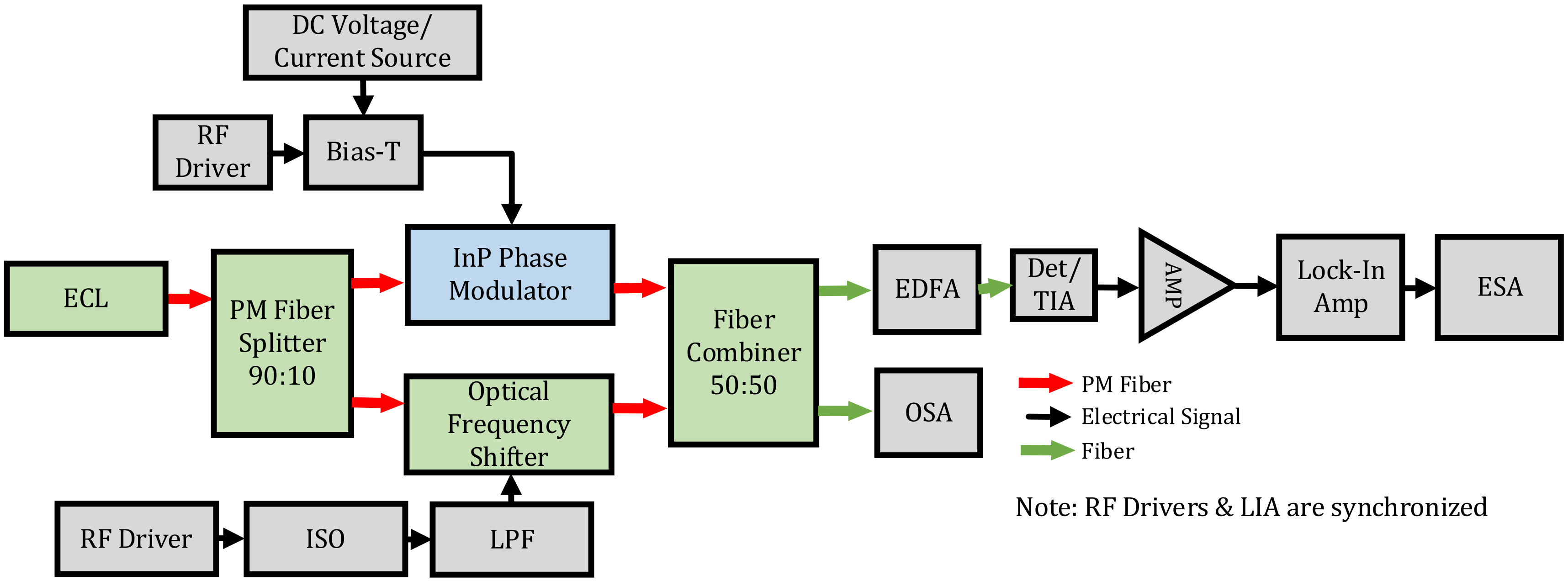

Note: RF Drivers & LIA are synchronized

Figure 4.12 Measurement setup for phase modulator efficiency and RAM.

Where possible, polarization maintaining fiber is used. An isolator and low pass filter are used to reduce harmonics from the signal generator driving the optical frequency shifter. Normally the standard high-power driver that can be purchased with the frequency shifter would be used but that option did not have a 10 MHz synchronization port. Hence, we used standard RF generators to synchronize the RF drivers for the optical frequency shifter, indium phosphide phase modulator, and lock-in amplifiers. This helps ensure better phase coherence during testing. It is better to use a single source with multiple split paths but requires additional microwave components. As the drive level on the modulator rises, so do the fundamental and higher order optical phase and amplitude modulation components. After detection on an ESA, these levels can then be plotted as a function of the drive strength. A narrow linewidth (100 kHz) ECL ensures that the ESA’s frequency noise floor remains low, since a good degree of coherence is maintained in the setup as light propagates along different paths. This generates a strong beat note at the optical shift frequency of 107 MHz. Because we rely on a digital LIA, it is important to use an external preamplifier to ensure that the input levels into the LIA are at least 200 mVpp. This helps minimize quantization noise of the input ADC. For RAM measurements, it is important to know the unmodulated beat note input amplitude to the LIA. In post processing, this level can be used to find the ratio of peak-to-peak power fluctuations to the average power according to our definition of RAM. Finally, the modulation frequency is limited on the low end by the bias-T low frequency cutoff and on the high end by the bandwidth of the LIA’s low pass filter. A modulation frequency between 0.5-1 MHz is suitable.

4.4.4 Phase Modulator Efficiency in Forward Bias

Fig. 4.13 compares the efficiency for a 2.5 mm long ridge waveguide phase modulator for different forward bias points of 5, 10, and 25 mA.

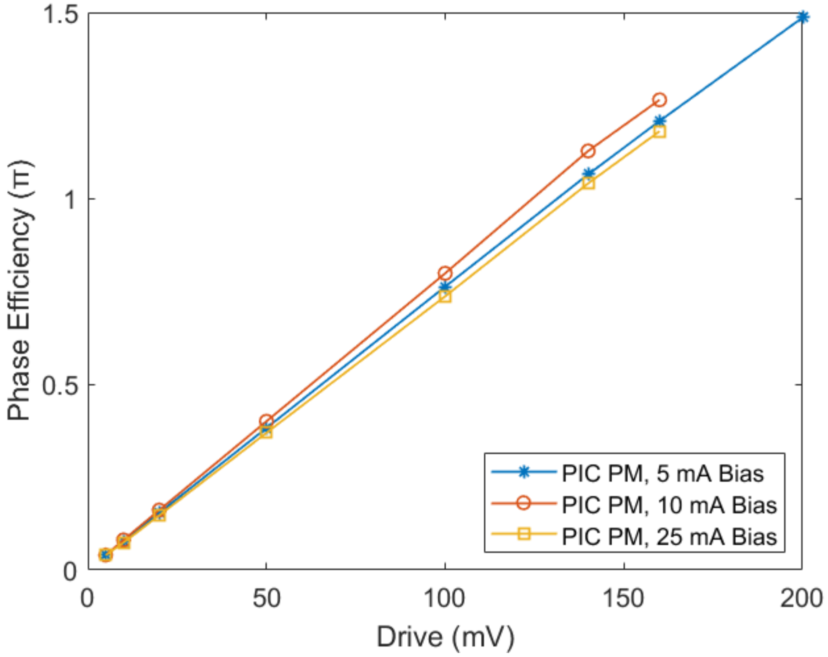

Figure 4.13 Phase modulator efficiency in forward bias.

It is important to note in this plot that the drive on the horizontal access would be the drive delivered to a 50Ω load from a 50Ω signal generator. The actual drive can be obtained by performing a phase modulator return loss measurement using a network analyzer and calculating the reflection coefficient. To account for the variation in the phase modulator load at low modulation frequencies, we can estimate the equivalent resistance from the IV curve and scale the horizontal axis drive values accordingly for a simple linear analysis. The IV curve is provided in Fig. 4.18. The approximate linearized loads at the different bias points are illustrated in Tab. 4-3.

Bias Current	Linearized Equivalent Load
5 mA	17.2 Ω
10 mA	9.6 Ω
25 mA	8.1 Ω

Table 4-3 Phase modulator linearized loads at different bias points.

Fig. 4-14 shows the adjusted phase modulator efficiencies. We can see that using 50 Ω signal generators, there appears to be an increase in the low frequency modulation efficiency at increased current level bias points. As is discussed shortly, phase shift in forward bias, due to free carrier absorption, relies on changes in the current density of the modulator. A larger equivalent series resistance results in an overall smaller change in current for an identical voltage drive level. These results are therefore expected.

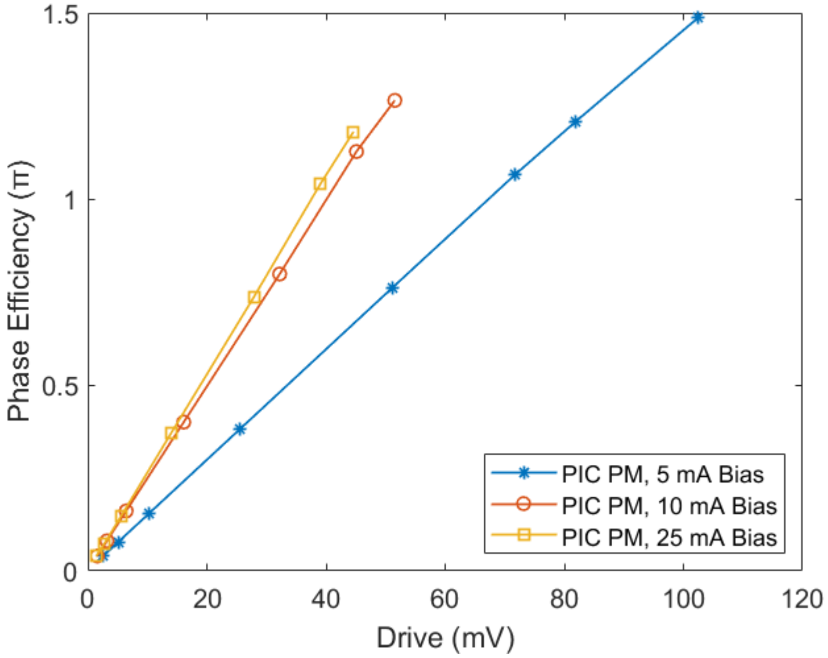

Figure 4.14 PM efficiency with drive levels scaled according to the linearized loads.

We can thus conclude that it is advantageous to have a small series resistance when driving the phase modulator in forward bias with a 50Ω signal generator.

Because phase shift in forward bias relies on a carrier density effect, we can define a J_π and we obtain this value using a few assumptions. For simplicity we also assume that the current flow in the waveguide is strongly confined to a lateral area defined by the ridge width which is approximately 3 microns. For a 2.5 mm long phase modulator the current flow waveguide cross section is $2.5\,mm * 3\,\mu m = 7.5 * 10^{-5}\,cm^2$. Since we know the actual voltage drop and linearized load, we can now estimate the phase modulator efficiency as a function of the current density drive in the waveguide at different bias current densities.

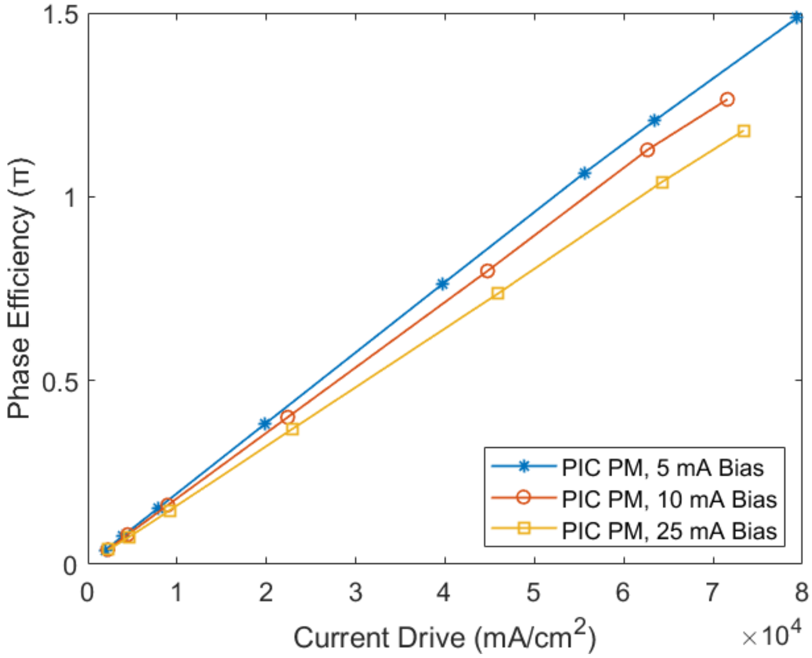

Figure 4.15 PM efficiency with respect to current density drive levels at different forward bias points.

Over the examined range from 5 to 25 mA, Fig. 4-15 shows that the phase modulation efficiency slightly drops at greater current bias points. This is possible due to heating, current spread, and reduced nonlinear effects on the response. Nevertheless, this is perhaps the most appropriate characterization of the modulator's efficiency as it captures the physics in forward bias operation and ideally would be made without factoring the modulator's equivalent load. Changes in current would preferably be made using an ideal current source, which unlike a 50Ω source, injects a set current without attention to the modulator's equivalent load.

To obtain a better feel for the operating conditions, we use the plot of Fig. 4-14 to find that for our 2.5 mm long phase modulator, at a 25 mA bias, approximately 5 mApp drive is required to achieve a π phase shift. This is a good indicator that the linearized load analysis is limited to mostly higher bias currents as these changes are clearly large enough for non-linear operation as can be seen from the IV curve at a 10 mA bias point. Finally, at 25 mA bias, we define our $J_\pi = 65\ A/cm^2$.

4.4.5 Phase Modulator Efficiency in Reverse Bias

Fig. 4.16 shows the efficiency for our 2.5 mm long ridge waveguide phase modulator in reverse bias.

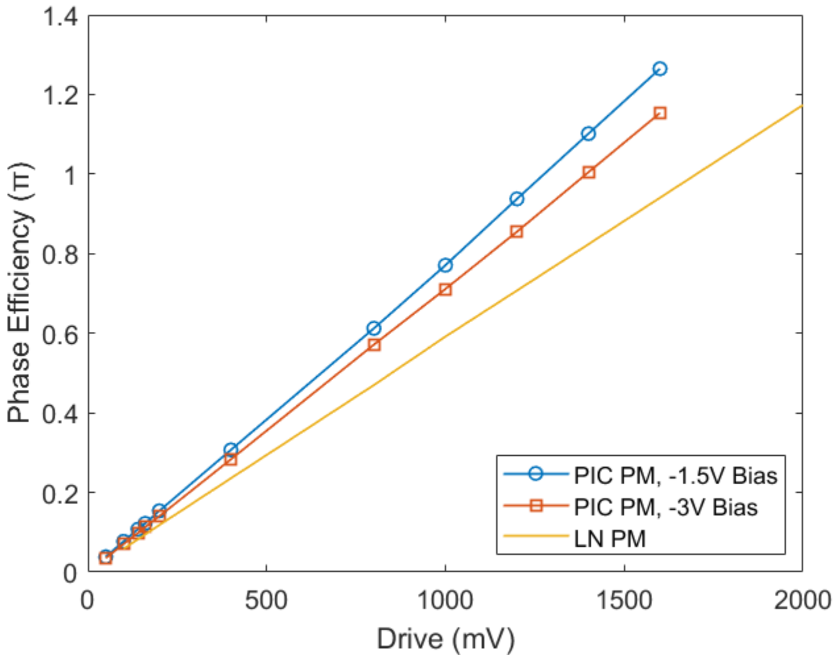

Figure 4.16 PM efficiency in reverse bias.

The horizontal axis assumes a 50Ω load which is far from the case for our reversed biased phase modulator which acts more like a high impedance load at low modulation frequencies. The performance of a commercial lithium niobate phase modulator is also plotted for comparison. This modulator also has a high impedance load which indicates the required drive is actually double that shown on the graph. In the case of the indium phosphide modulator, we perform a simple analysis as in the forward bias case to estimate the actual efficiency by determining the equivalent small signal load at different bias points which can be obtained from the IV curve in Fig. 4.20. Tab. 4-4 shows the equivalent low frequency loads at two different bias points obtained by taking the inverse of the slope of a fitted curve.

Reverse Bias	Equivalent Load
-1.5V	946Ω
-3V	570Ω
Lithium Niobate	10,000Ω

Table 4-4 Equivalent small signal load of a PM in reverse bias.

We can now scale the drive levels assuming these loads and a linear response about the modulation drive level. This analysis is far more limited than the forward bias counterpart since the signal levels are very large. Fig. 4.17 shows the modulation drive levels assuming these loads. The drive levels expectedly approximately doubled because of the high impedance loads presented to the 50Ω signal source generator.

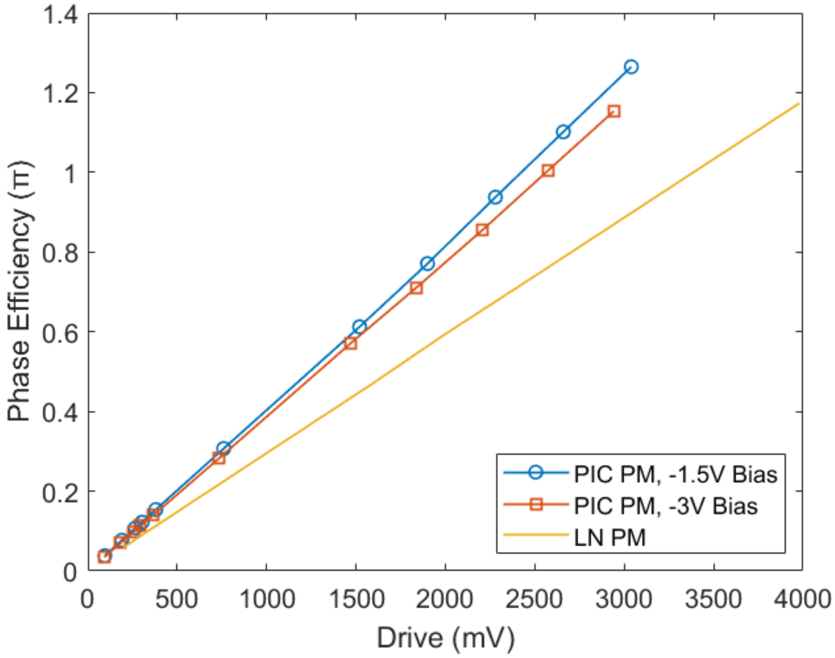

Figure 4.17 PM efficiency scaled according to linearized loads.

We can now define the efficiency of our phase modulator at a reverse bias of -1.5V. Fig. 4.17 indicates that the $V_\pi = 2.5\text{V}$. This is approximately 1V or 30% better than the commercial LN modulator. Because we rely on electro-optic effects we can define the general structural efficiency using results from our 2.5 mm long phase modulator to be: $\frac{180°}{2.5V*2.5mm} = 29\frac{°}{V*mm}$.

4.4.6 Phase Modulator Peak-to-Peak RAM in Forward Bias

We can first estimate the DC RAM performance for a forward biased phase modulator using simple loss-current-voltage (LSIV) curves. Fig. 4.18 shows the LSIV curves for a 2.5 mm long indium phosphide ridge waveguide phase modulator. The power was detected off-chip with a power meter. An edge coupled lensed fiber was used to collect light from the PIC. Fig. 4.17 shows that there is an exponential decay in the output power in forward bias as the current density in the modulator increases.

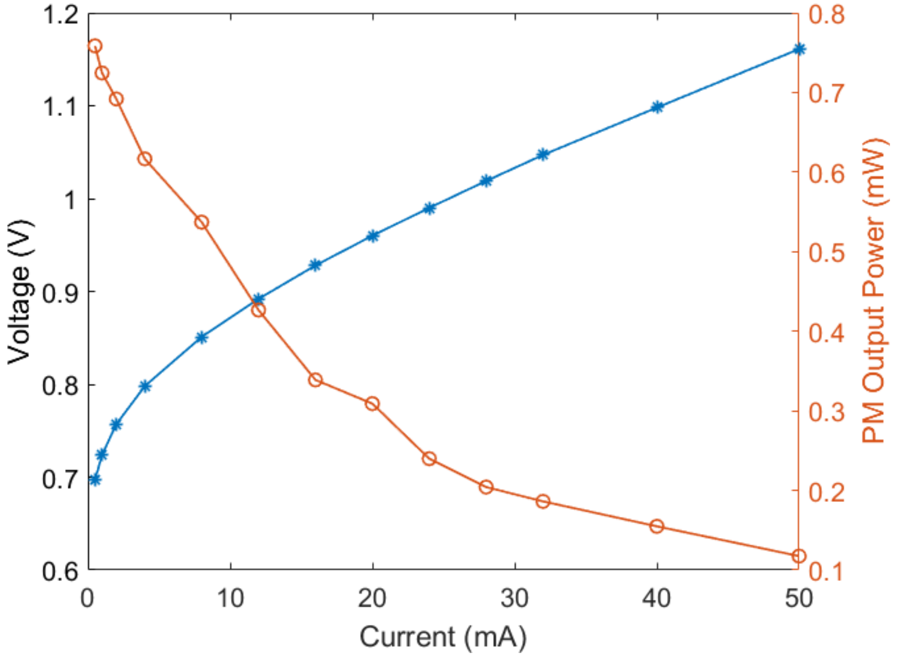

Figure 4.18 Loss-current-Voltage curves of forward biased PM.

To estimate peak-to-peak RAM from this curve, we simply observe what the changes in output power are at a particular bias point for a given modulation swing about that bias point. We can assume the bias point power as the average power, although strictly speaking this is only the case when the swing deviations in power are equal. For a more accurate estimate, we can obtain the nonlinear coefficients of the RAM response by using the Taylor series expansion about the bias point to the appropriate degree for the modulation strength used. For simplicity, we use the linearized loads to perform a quick estimate of peak-to-peak RAM using points on the plot at a bias of 24 mA which was used for system testing. For calculations, three points are selected in Tab. 4-5.

Phase Modulator Current	Output Power
20 mA	0.309 mW
24 mA	0.240 mW
28 mA	0.204 mW

Table 4-5 Points for RAM estimation in forward bias.

We can now estimate peak-to-peak RAM: $\frac{0.309-0.204}{0.240} * 100\% = 43.8\%$. This implies that peak-to-peak fluctuations in power are approximately 43.8% the average power for current swings of ± 4 mA. We saw from before that 5 mApp is required for a π phase shift and so we can appropriately scale the expected RAM to be 27% in this case. Because the IV response of the phase modulator is approximately linear, we can quickly estimate the drive required from a 50Ω signal generator in lab assuming we use a bias-T to separately drive the phase modulator with RF and DC signals. We saw from before that at a forward bias of 25 mA, the equivalent load is 8 Ω. A 5 mA current swing would result in a $5\ mA * 8\ \Omega = 40\ mVpp$ swing across the phase modulator diode. We can quickly determine the signal source level required for this using a resistive divider circuit. To deliver this voltage swing, the 50 Ω signal source generator would have to be $40\ mVpp * \frac{(8+50)}{8} = \ 290\ mVpp$.

Using the test setup from Fig. 4.12, we can plot the first order peak-to-peak RAM as a function of the drive levels on our modulator in forward bias. We rely here on the first order products as they were by far the most dominant. We also convert the voltage drive levels to current density to make a fair comparison to the phase modulator efficiency from Fig. 4.15 which is replotted in Fig. 4.19 for convenience.

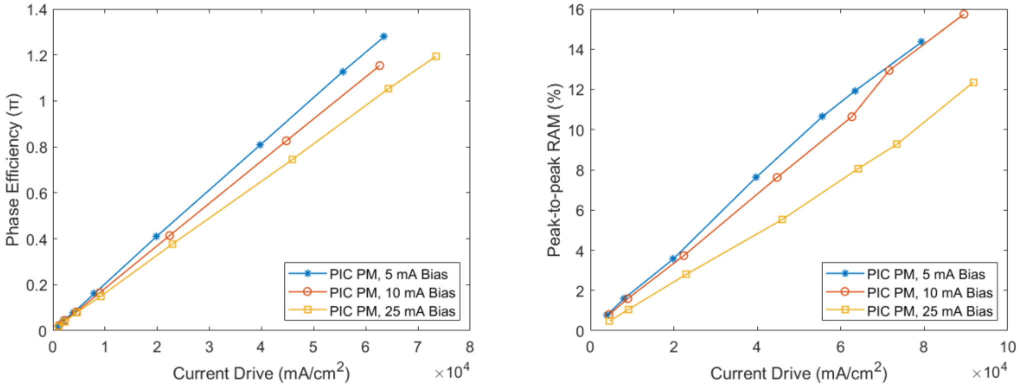

Figure 4.19 Efficiency and RAM comparison in forward bias.

We see that at a bias of 25 mA, which has a $J_\pi = 65\ A/cm^2$, the RAM levels are approximately 8% which is two orders of magnitude greater than lithium niobate modulators. This is also much reduced compared to the value from a linear analysis, stressing the importance of measurement and more accurate load representation. While not illustrated here, a complete picture of the efficiency and RAM can be obtained by adding up contributions from higher order components. Because we used a 50 Ω source to drive our modulators, the modulator efficiency was best at 25 mA since the equivalent load was smallest. This results in the greatest current modulation for the same voltage drive. Furthermore, of the operating points studied, the operation is most linear at 25 mA since the series resistance of the modulator dominates the IV response. We also see from Fig. 4.19 that the RAM at 25 mA bias would be minimized at equal modulation current drive densities. When we study the LSIV curve of the modulator, it appears as though the 25 mA bias will have the best RAM performance due to reduced deviations in power for the same current drive levels but it is important to keep in mind the loss and thus average power are the highest and lowest respectively. It turns out that 25 mA was indeed the best in terms of efficiency and RAM compared to the other points. Of course, one must balance this performance with the acceptable output power from the PIC which was minimum at 25 mA. This was nevertheless sufficient to generate a strong error signal for feedback stabilization of the master laser. An SOA before the modulator would have still been beneficial.

4.4.7 Phase Modulator Peak-to-Peak RAM in Reverse Bias

A similar discussion on peak-to-peak estimate of RAM holds true for the indium phosphide ridge waveguide phase modulator in reverse bias. Fig. 4.20 shows the current through the phase modulator as a function of the voltage bias across it. Fig. 4.20 also shows the loss obtained by edge coupling a lensed fiber to a PIC and observing the output power with a power meter.

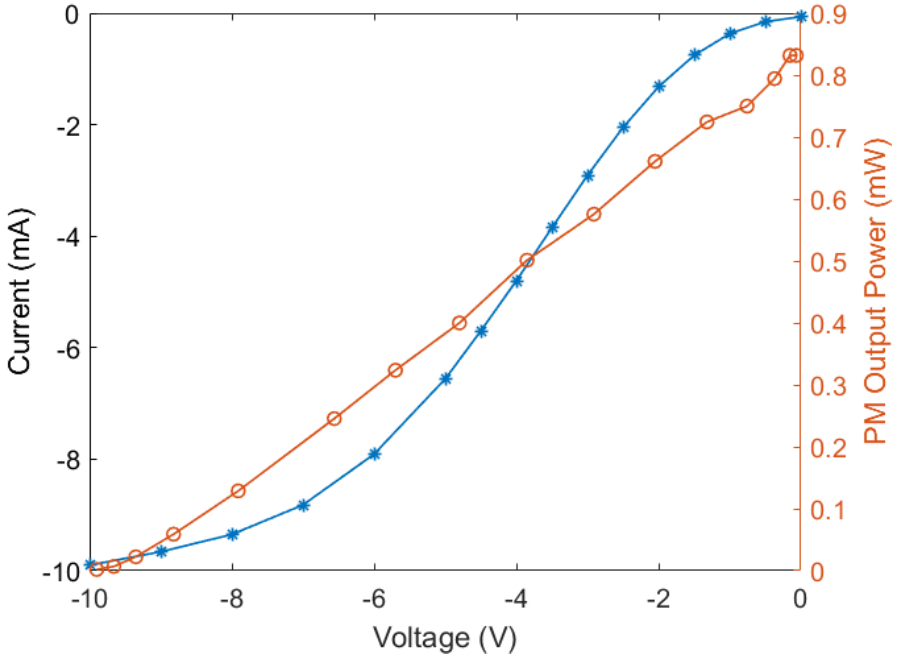

Figure 4.20 LSIV curve of a reverse biased PM.

The output power appears to fall linearly with reverse bias until it begins to flatten out around -9V when most of the power has been absorbed. We can again estimate the peak-to-peak RAM using the loss curve by selecting three points shown in Tab. 4.6:

Phase Modulator Voltage	Phase Modulator Output Power
-2.5V	0.661 mW
-3V	0.575 mW
-3.5V	0.501 mW

Table 4-6 Point for linearized analysis of reverse biased PM.

The peak-to-peak RAM can now be estimated to be: $\frac{0.661-0.501}{0.575} * 100\% = 27.8\%$. This implies that peak-to-peak fluctuations in power are approximately 27.8% the average power for current swings of ± 0.5V. It is worth mentioning again that for a more complete analysis, a Taylor series expansion should be used to determine the non-linear coefficients of peak-to-peak RAM about the bias point to the appropriate degree for the modulation strength used. We can also quickly estimate the drive required from a 50Ω signal generator in lab assuming we use a bias-T to separately drive the phase modulator with RF and DC signals. The IV curve at a bias point of -3V is approximately linear. We see therefore that the reverse biased diode can be modeled with a series resistor of 570Ω. The high impedance is expected for a reverse biased diode as it is typically approximated as a current source in this regime. To deliver a 1Vpp voltage swing, the 50Ω signal source would have to be $1\,Vpp * \frac{(550+50)}{550} = 1.1\,Vpp$. We make a similar comparison in Fig. 4.21 of peak-to-peak RAM and efficiency in reverse bias as we did in forward bias. We also scale the drive levels appropriately to their linearized loads for consistency and focus on first order RAM which was dominant at our required modulation levels.

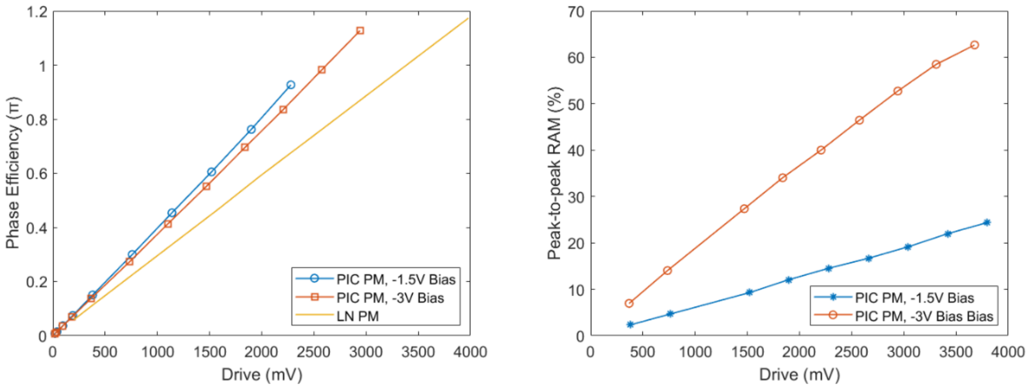

Figure 4.21 PM efficiency and RAM in reverse bias.

We can conclude that while the efficiency in both cases was similar, the RAM at -3V was more significant both due to the lower output power and greater variation in power for drive levels that were similar in both cases in terms of efficiency. Thus, we can conclude that in reverse bias it is preferable to operate at reduced reverse bias levels and ideally a flattening of the loss curve at those levels is desirable.

4.4.8 RAM Shapes

Although the previous sections have mostly focused on a simplified linear approach, it is worth investigating the shape of RAM for various bias levels of the indium phosphide waveguide phase modulator. In addition to the spectral strength response that can be obtained for each nonlinear component of RAM, it is desirable to observe the cumulative shape in the time domain. This can be done by tracing out the LSIV curve, directly observing the intensity output variation from the modulator on an oscilloscope, or replacing the ESA in Fig. 4.12 with a scope. The modulation envelop waveform can be used to estimate peak-to-peak RAM by dividing the peak-to-peak fluctuations by the mean. Fig. 4.22 shows the RAM envelope obtained for a drive level of 160 mVpp at forward bias levels of 5, 10, and 25 mA respectively. We can see for example, by dividing peak-to-peak fluctuation by the mean, that peak-to-peak RAM for 10 mA forward bias at 160 mVpp, results in a RAM of about 13%.

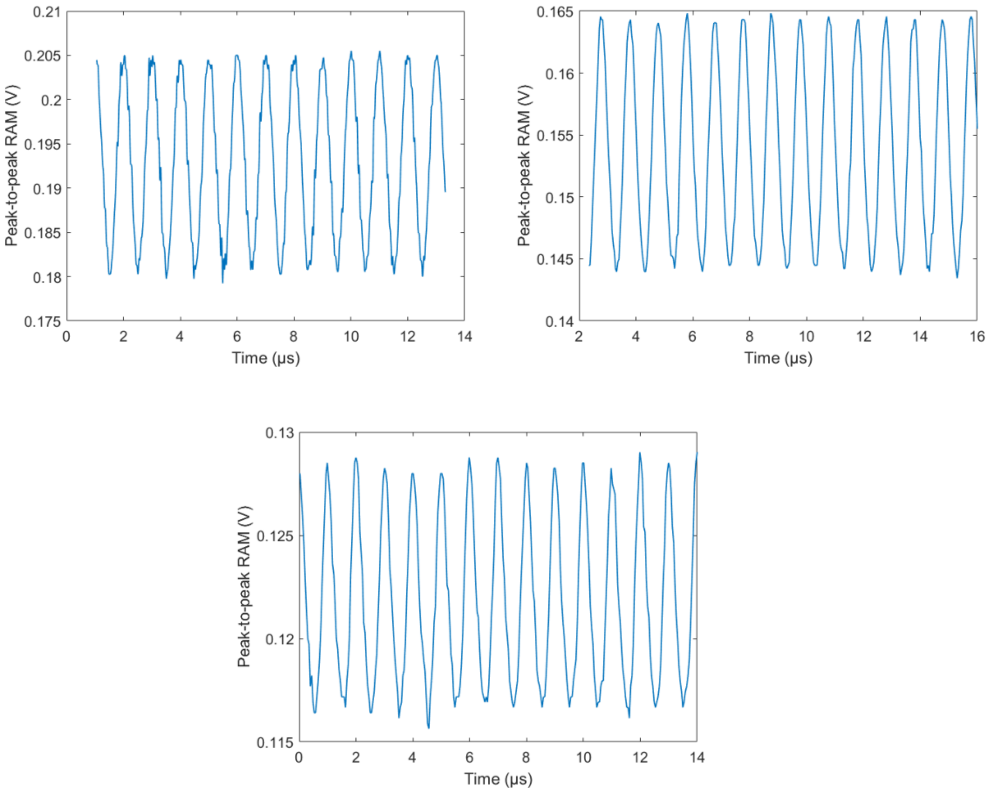

Figure 4.22 RAM modulation envelopes at a bias operation of 5, 10, and 25 mA.

4.4.9 Low-RAM Phase Modulators

Phase modulators have critical importance in the overall performance in absorption spectroscopy and laser stabilization. Semiconductor based phase modulator designs, particularly in indium phosphide, show significant RAM due to absorption. This is the case both in forward and reverse bias due to free carrier absorption or the electro-refractive effect respectively.

A new type of promising phase modulator with improved RAM was implemented in generation 2. A schematic of the device is shown in Fig. 4.23 along with a micrograph of the fabricated structure. The phase modulator has a Mach-Zehnder type structure and is based on a shift-and-dump Mach-Zehnder switch from [24].

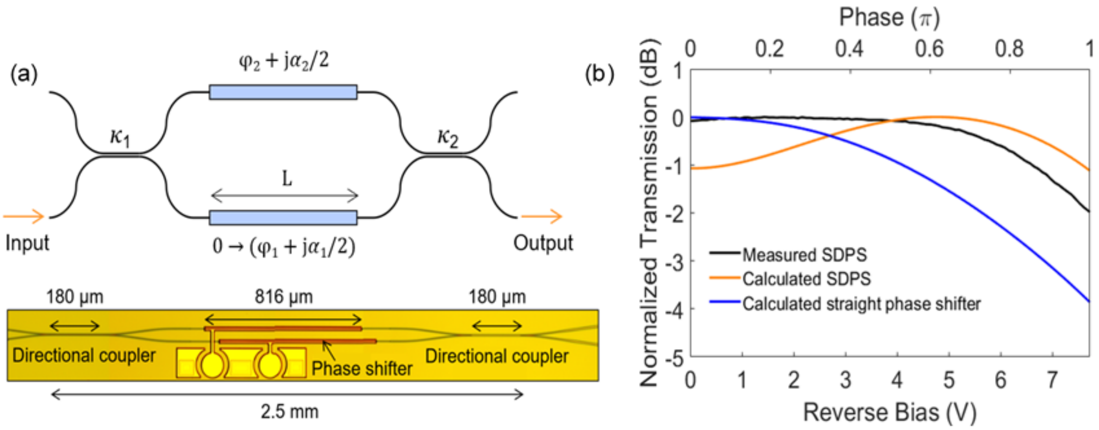

Figure 4.23 Mach-Zehnder type phase modulator.

After incoming light is split by a directional coupler, light in each arm experiences absorption loss and a phase shift. While the bottom modulator arm is biased and sinusoidally modulated to obtain the proper phase shift for the application, the top arm is optimally biased so that the amplitude output remains constant along the entire modulation cycle. For example, on the upswing of the modulation, the bottom arm experiences a phase shift and possibly increased absorption in forward bias modulation. Consequently, the light arriving at the output coupler on both arms has a different relative phase. This changes the nature of the interference at the output directional coupler with the intent that the additional loss experienced during the up-swing modulation is compensated for through reduced destructive interference on the output. A similar reverse action would occur on the downswing.

Fig. 4.23 also shows the response comparison over a π phase shift between a straight and Mach-Zehnder type phase shifter. The change in transmission is clearly reduced over π phase shift. In that phase modulator, where the coupling coefficients were designed such that $\kappa = 0.12$, the change in transmission over a π phase shift was reduced from 3.85 dB to 1.98 dB. The reduction in transmission difference for $\pi/2$ phase shift appears to be significantly more impressive.

The condition in the modulator to achieve reduced RAM is expressed in Eq. 4.16 which sets the Mach-Zehnder transmission levels equal at a 0 and a prescribed phase shift which in this case is π. Using the device structure from Fig. 4.23, Eq. 4.16 can be expressed in terms of the coupling coefficients, absorption, and arm lengths according to Eq. 4.17.

$$E_{out}(\varphi_1 + \tfrac{j\alpha_1}{2}) = E_{out}(0)e^{j\varphi_1} \tag{4.16}$$

$$e^{j\varphi_1}\sqrt{(1-\kappa_1)(1-\kappa_2)}\left(1 - e^{-\frac{\alpha_1 L}{2}}\right) + e^{\left(j\varphi_2 - \frac{\alpha_2 L}{2}\right)}\sqrt{\kappa_1\kappa_2}\left(1 - e^{j\varphi_1}\right) = 0 \tag{4.17}$$

References

1. L. A. Coldren and S. W. Corzine, Diode Laser and Photonics Integrated Circuits. New York: Wiley-Interscinece (1995).
2. Jayaraman, V., Chuang, Z. M., & Coldren, L. A. (1993). Theory, Design, and Performance of Extended Tuning Range Semiconductor Lasers with Sampled Gratings. IEEE Journal of Quantum Electronics, 29(6), 1824–1834. https://doi.org/10.1109/3.234440
3. Liang, W., Yariv, A., Kewitsch, A., & Rakuljic, G. (2007). Coherent combining of the output of two semiconductor lasers using optical phase-lock loops. Optics Letters, 32(4), 370. https://doi.org/10.1364/ol.32.000370
4. Kobayashi, S., Yamamoto, Y., Kimura, T., & Ito, M. (1982). Direct Frequency Modulation in AIGaAs Semiconductor Lasers. IEEE Transactions on Microwave Theory and Techniques, 30(4), 428–441. https://doi.org/10.1109/TMTT.1982.1131084
5. S. Ristic, A. Bhardwaj, M. J. Rodwell, L. A. Coldren and L. A. Johansson, "An Optical Phase-Locked Loop Photonic Integrated Circuit," in Journal of Lightwave Technology, vol. 28, no. 4, pp. 526-538, Feb.15, 2010, doi: 10.1109/JLT.2009.2030341.
6. Ristic, S., Bhardwaj, A., Rodwell, M. J., Coldren, L. A., & Johansson, L. A. (2009). Integrated Optical Phase-Locked Loop. 2–4.
7. Abshire, J. B., Riris, H., Allan, G. R., Weaver, C. J., Mao, J., Sun, X., Hasselbrack, W. E., Kawa, S. R., & Biraud, S. (2010). Pulsed airborne lidar measurements of atmospheric CO2 column absorption. *Tellus, Series B: Chemical and Physical Meteorology*, *62*(5), 770–783. https://doi.org/10.1111/j.1600-0889.2010.00502.x
8. Lee, S. L., Heimbuch, M. E., Cohen, D. A., Coldren, L. A., & DenBaars, S. P. (1997). Integration of semiconductor laser amplifiers with sampled grating tunable lasers for WDM applications. IEEE Journal on Selected Topics in Quantum Electronics, 3(2), 615–627. https://doi.org/10.1109/2944.605713
9. Mason, B., Barton, J., Fish, G. A., Coldren, L. A., & DenBaars, S. P. (2000). Design of sampled grating DBR lasers with integrated semiconductor optical amplifiers. IEEE Photonics Technology Letters, 12(7), 762–764. https://doi.org/10.1109/68.853492
10. Al., K. E. S. et. (1992). Recent advances in semiconductor optical amplifiers and their applications. 242–245.
11. J. P. Donnelly *et al*., "High-power 1.3-μm InGaAsP-InP amplifiers with tapered gain regions," in *IEEE Photonics Technology Letters*, vol. 8, no. 11, pp. 1450-1452, Nov. 1996, doi: 10.1109/68.541546.
12. Numata, K., Chen, J. R., Wu, S. T., Abshire, J. B., & Krainak, M. A. (2011). Frequency stabilization of distributed-feedback laser diodes at 1572 nm for lidar

measurements of atmospheric carbon dioxide. Applied Optics, 50(7), 1047–1056. https://doi.org/10.1364/AO.50.001047

13. Jonathon Barton, PhD thesis, University of California, Santa Barbara, September 2004.
14. Lawetz, C., Cartledge, J. C., Rolland, C., & Yu, J. (1997). Modulation characteristics of semiconductor Mach-Zehnder optical modulators. Journal of Lightwave Technology, 15(4), 697–702. https://doi.org/10.1109/50.566692
15. Bach, H. G., Krauser, J., Nolting, H. P., Logan, R. A., & Reinhart, F. K. (1983). Electro-optical light modulation in InGaAsP/InP double heterostructure diodes. Applied Physics Letters, 42(8), 692–694. https://doi.org/10.1063/1.94075
16. Mendoza-Alvarez, J. G., Coldren, L. A., Yan, R. H., Hausken, T., Lee, K., Alping, A., & Pedrotti, K. (1988). Analysis of Depletion Edge Translation Lightwave Modulators. Journal of Lightwave Technology, 6(6), 793–808. https://doi.org/10.1109/50.4068
17. Ito, F., Matsuura, M., & Tanifuji, T. (1989). A Carrier Injection Type Optical Switch in GaAs Using Free Carrier Plasma Dispersion with Wavelength Range from 1.06 to 1.55 μm. IEEE Journal of Quantum Electronics, 25(7), 1677–1681. https://doi.org/10.1109/3.29311
18. Botteldooren, D., & Baets, R. (1989). Influence of band-gap shrinkage on the carrier-induced refractive index change in InGaAsP. Applied Physics Letters, 54(20), 1989–1991. https://doi.org/10.1063/1.101191
19. iXblue Photonics White Paper. "*Residual Amplitude Modulation of Optical Phase Modulator*".
20. Whittaker, E. A., Gehrtz, M., & Bjorklund, G. C. (1985). Residual amplitude modulation in laser electro-optic phase modulation. Journal of the Optical Society of America B, 2(8), 1320. https://doi.org/10.1364/josab.2.001320
21. Numata, K., Chen, J. R., Wu, S. T., Abshire, J. B., & Krainak, M. A. (2011). Frequency stabilization of distributed-feedback laser diodes at 1572 nm for lidar measurements of atmospheric carbon dioxide. Applied Optics, 50(7), 1047–1056. https://doi.org/10.1364/AO.50.001047
22. Wong, N. C., & Hall, J. L. (1985). Servo control of amplitude modulation in frequency-modulation spectroscopy: demonstration of shot-noise-limited detection. Journal of the Optical Society of America B, 2(9), 1527. https://doi.org/10.1364/josab.2.001527
23. Arar, B., Schiemangk, M., Wenzel, H., Brox, O., Wicht, A., Peters, A., & Tränkle, G. (2017). Method for in-depth characterization of electro-optic phase modulators. Applied Optics, 56(4), 1246. https://doi.org/10.1364/ao.56.001246
24. Nicolas Dupuis, Jonathan E. Proesel, Herschel Ainspan, Christian W. Baks, Mounir Meghelli, and Benjamin G. Lee, "Nanosecond-scale shift-and-dump Mach–Zehnder switch," Opt. Lett. 44, 4614-4616 (2019)

Chapter 5. PIC Subsystem Measurements

5.1 Error Signals

As we saw earlier, coherent detection in laser-based frequency modulation spectroscopy shows that a variety of error signals can be obtained [1,2]. The error signal in this work was obtained by sweeping the frequency modulated laser across the CO_2 absorption line and coherently detecting a beat note generated by the gas cell detector. The error signal and reference gas cell transmission for quadrature detection is demonstrated in Fig. 5.1.

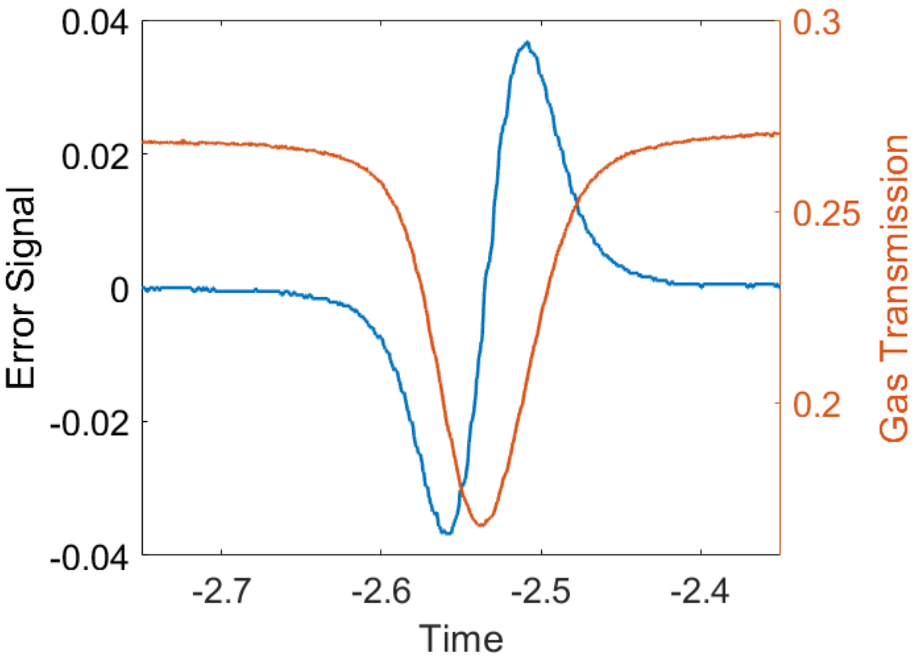

Figure 5.1 Gas cell transmission and coherently detected error signal.

We previously saw that the integrated phase modulator in forward bias generates significant RAM levels. Measured values were approximately 10% for our required modulation index. Nevertheless, quadrature detection of the beat note does not seem to generate significant offsets in the error signal as can be seen in Fig. 5.1 and confirmed in the gas sensing measurements in Ch. 6. Instead, there appears to be very good agreement in the shape of the error signal on the left- and right-hand side of the zero crossing. This is a good indication that systematic frequency offsets are mostly attenuated with coherent quadrature detection using our phase modulator. It is also likely that this offset cancellation is strong because of the phase modulator efficiency. This allows operation over a mostly linear regime as discussed in Ch. 4. In such a case we can express the output of the modulated PIC as sinusoidally amplitude and phase modulated according to Eq. 5.1, which after expansion and some trigonometry can be rewritten according to Eq. 5.2. *a* and *m* are the amplitude and phase modulation indices respectively.

$$A(1-\mathrm{asin}(\omega_m t))\cos\left(\omega_c t - msin(\omega_m t)\right) \tag{5.1}$$

$$A\cos(\omega_c t - m\sin(\omega_m t)) - \frac{Aa}{2}\sin\{(\omega_c+\omega_m)\,t - m\sin(\omega_m t)\} + \frac{Aa}{2}\sin\{(\omega_c-\omega_m)\,t - m\sin(\omega_m t)\} \tag{5.2}$$

Eq. 5.2 shows that the inputs to the gas cell are the desired purely phase modulated carrier signal along with two additional carriers offset from the primary carrier by the modulation frequency. These additional carriers are also purely phase modulated with amplitudes scaled according to the amplitude modulation index. If each component of Eq. 5.2 can be treated independently, we can hypothesize that when our wavelength is purely aligned with the absorption line, where its error signal is zero, any component in the output due to the offset carriers demodulated in quadrature cancel each other. This cancellation is likely limited by the amplitude and phase modulation response nonlinearity which may account for slight offsets in the error response. Measurements show that for a modulation index of π the RAM and phase efficiency response of the phase modulator in forward bias is dominated by the linear components. As the frequency shifts from the center, these additional error signals may be opposite in sign but are not the same magnitude. Thus, we can also hypothesize that this cancellation effect is reduced but not dominant relative to the error signal from the primary carrier. The linearity of the demodulated error signal shows that perhaps there is only an effect on the error slope. Fig. 5.2 compares the in-phase and quadrature error signals. We see that the in-phase error signal displays an offset which would introduce a significant systematic offset in the locking wavelength. We can thus hypothesize that while the quadrature dispersion components cancel, the in-phase absorption components add up to produce an offset. Note the slight asymmetry generated in the dispersion signal as well using strong inputs. Clearly the absorption signal is inappropriate for wavelength locking.

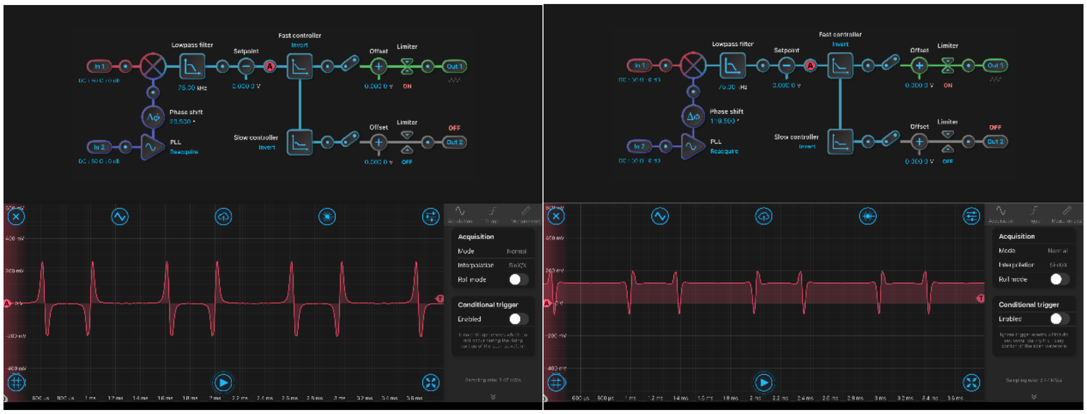

Figure 5.2 Quadrature and in-phase error signals.

5.2 Master Laser Stabilization

Fig. 5.3 shows the test setup for long-term stability of the master laser wavelength [3]. The laser is initially tuned to a wavelength ~ 0.35 nm below the absorption line. This is because thermal coupling from the other devices on the PIC will shift its operating wavelength. Most of that shift is due to thermal coupling from the 150 mA injected into the slave laser gain section. The slave laser is also tuned to the vicinity of the absorption line, although its wavelength is not considered for master laser stabilization. Once all the devices are on, the phase modulator is driven at a modulation depth of π at 125 MHz. The modulation frequency and depth are selected to obtain the sharpest frequency discriminating error slopes. This analysis was done at NASA Goddard and actually showed that an optimal error signal could be obtained using a modulation frequency of 250 MHz and index of 2.5π. Such a modulation depth was impractical in our indium phosphide modulators. The modulated light is edge coupled off-chip using a polarization maintaining lensed fiber. PM fiber reduces time-varying sources of RAM due to the birefringence of single mode non-PM fiber such as SMF-28 fiber.

Modulated light passes through a Herriott gas cell with an equivalent path length of 10 meters and CO_2 pressure of 40 mbar. The modulated light experiences both absorption and dispersion as it travels along the cell. Deviations of the laser from the peak absorption line are encoded in a photo detected beat note at the 125 MHz modulation frequency in the form of an amplitude modulation. This beat note is amplified and coherently detected using a double balanced mixer. Coherent phase detection generates a frequency discriminating error signal. A servo filters the error signal which is fed into the phase section to correct the wavelength.

By introducing a perturbing sinusoidal source on top of the original error signal using a difference amplifier, and observing the new error signal, we can study the feedback loop's ability to reject external perturbations. Fig. 5.4 demonstrates the frequency response perturbation rejection of the closed loop. As expected, the low frequency components are rejected strongly while the fast components are not, as the loop cannot response fast enough. This technique can be used to optimize the servo performance.

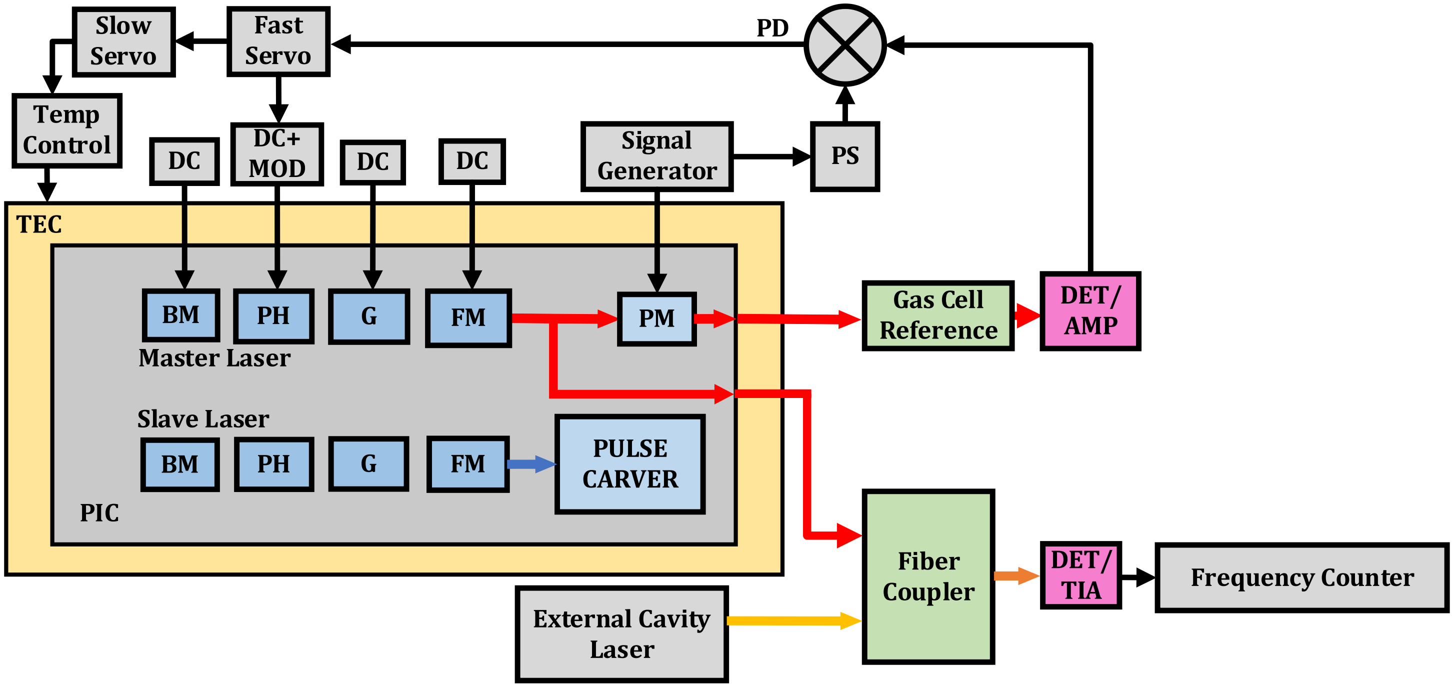

Figure 5.3 Test setup for master laser stabilization and frequency characterization.

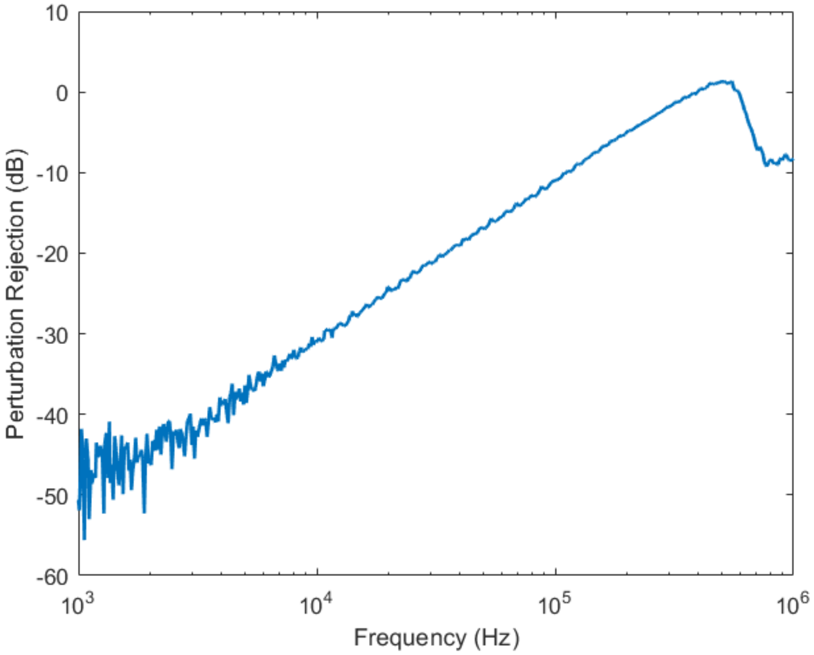

Figure 5.4 Feedback loop rejection of an external sinusoidal perturbation.

In Fig. 5.3, the fast servo response modulates the master laser phase to correct the wavelength. The slow servo is critical for operation over a wide temperature range when environmental disturbances are significant. In the controlled environment of the lab, the slow servo was not used. Instead, the PIC stage temperature was stabilized with a temperature controller and the modulation input was not used.

To characterize the long-term frequency stability of the master laser, a 2x2 directional coupler combines the master laser light with that from an ECL. The ECL is offset to the absorption line by ~2 GHz and is used as a frequency gold standard in this experiment. The combined light is photo detected which generates a 2 GHz beat note. This beat note is amplified with a TIA to appropriate sensitivity levels for detection by a frequency counter. The frequency counter is set to a gate time of 1 second. This measurement can be repeated continuously with a zero dead-time frequency counter such as the CNT-91. We can then obtain a plot of the measured frequency of the input beat note for a selected gate time over a given test time of an hour for example. Fig. 5.5 shows precisely this in a plot that measures the beat note frequency over a period of an hour for 1 second gate times.

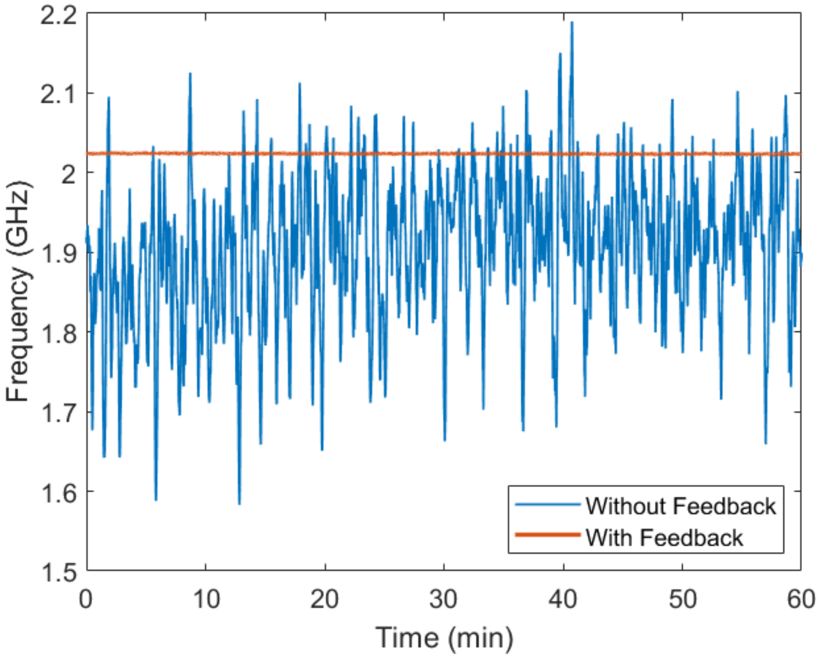

Figure 5.5 Master laser stability for 1 second gate times.

The frequency standard deviation over this 1-hr test time improved by a factor of 236 from 90.5 MHz to 384 kHz. Peak to peak frequency deviations improved by a factor of 221 from 607 MHz to 2.75 MHz. It is important to note that these results are obtained after warming up the system for an hour. It is also important to note that the assumption that the ECL is a gold standard is limited and its stability has not been characterized, although the ECL linewidth was verified to be 100 kHz and clearly had better drift performance than our free running SG-

DBR lasers. For more complete results the ECL frequency stability can be characterized, or two identical master SG-DBR lasers can be used [4]. Furthermore, the free-running stability of the master laser appears to be very poor. This is perhaps due to optical feedback from the lensed fibers and defective photonic devices in the PIC, such as the directional couplers.

Over long time scales, we can assess the noise performance of the laser with Allan deviation and relative Allan deviation measurements as illustrated in Fig. 5.6. The Allan deviation measurement eliminates effects such as systematic sources of noise in the measurement [4]. We can see that beginning approximately at gate times of 10 msec, the feedback performance results in a reduction in the Allan deviation by 2 orders of magnitude for 1 second gate times and almost 3 orders of magnitude for 10 second gate times. The relative Allan deviation was better than 10^{-9} in these cases.

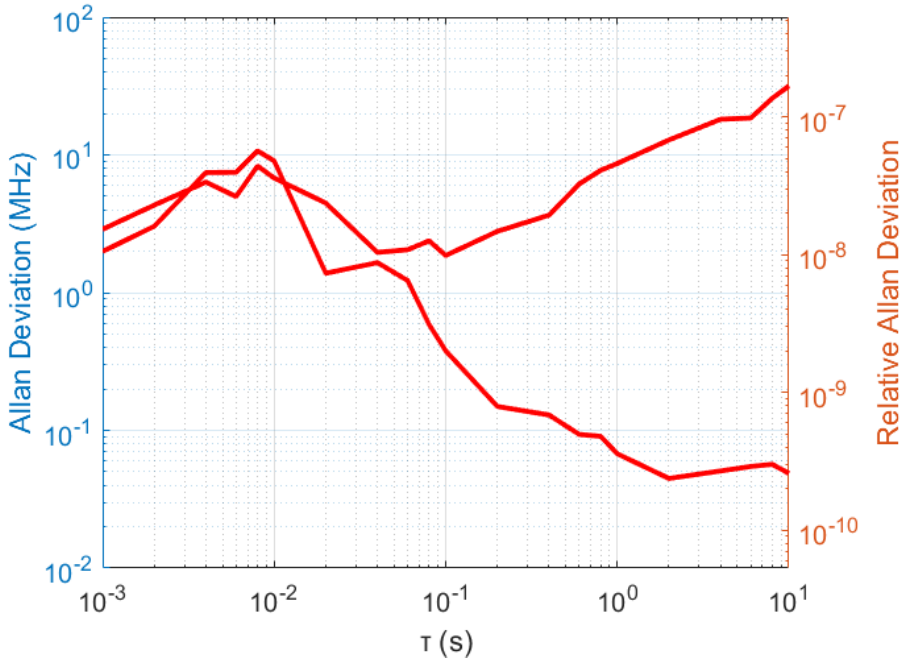

Figure 5.6 Allan and relative Allan deviation of the master laser unlocked and locked to the reference cell.

5.3 Slave Laser Stabilization

Once the master laser is stabilized, focus can turn to slave laser stabilization at programmed frequency offsets from the master laser. Fig. 5.7 shows a simplified test schematic for characterization of the offset frequency between the two lasers. For simplicity, Fig. 5.7 emits all the hardware required for master laser stabilization.

Our SG-DBR slave lasers are limited to approximately 12 GHz mode hop free tuning using the phase section of the laser only. This limits us to conveniently tune across ~ 10 GHz continuous windows on each side of the absorption line. To sample the opposite side of the absorption line or a window covering a greater range of wavelengths, the slave laser requires tuning of the front and back mirrors and perhaps the phase section. This is information that can be stored in a look-up table and fed forward to the slave laser once wavelength sampling of a window is complete. Fast frequency switching under 30 μs and up to 15 GHz offset using the phase section of a DS-DBR laser was demonstrated in [5]. There, feedforward injection of current reduced switching times to compensate for narrow PLL bandwidths.

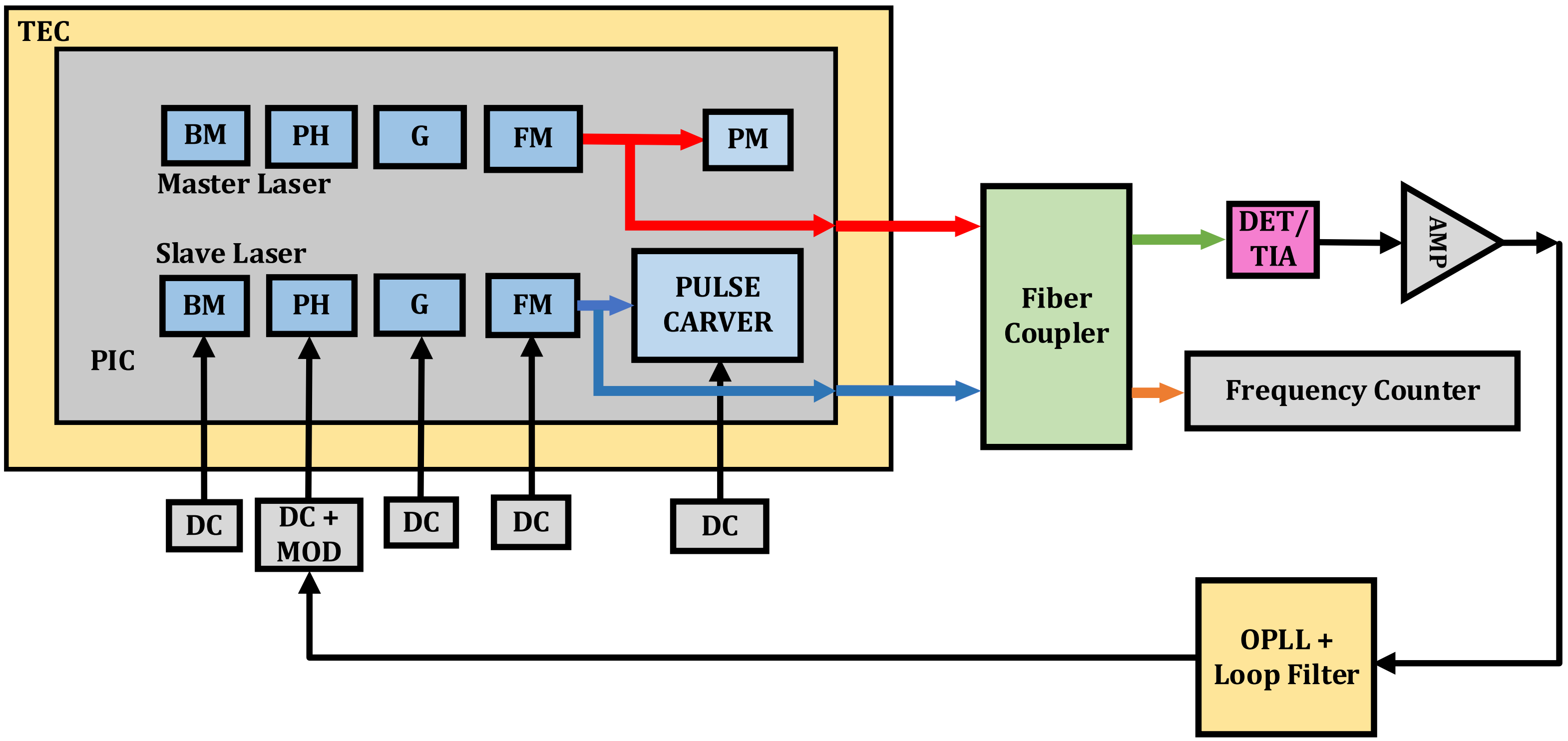

Figure 5.7 Test setup for slave laser offset locking to the master laser.

The OPLL loop filter drives a voltage-to-current converter with a transfer function of -2.5 mA/V. To ensure mode hop free continuous tuning windows, the active loop filter output range can be limited appropriately but this is not required. If output limiting is not implemented in some form, tuning beyond the mode hop free range can occur and does require startup of the OPLL to an initial condition. A startup condition can use an op-amp with pure proportional gain and can then be switched to proportional-integral gain once the loop is engaged. This prevents op-amp saturation due to integral control. If for example our sampling window is to be 1-10 GHz offset from the absorption line, a more direct but less effective approach may be to limit the output using appropriate supply levels or limiters. If we set the DC bias point of the laser phase section to be 10 mA, we can conveniently use an operational amplifier in our active loop filter with a ± 1V supply. This would limit the control voltage to approximately ± 1V into the voltage-to-current converter which corresponds to ± 2.5 mA current modulation. We previously saw that 4 mA was required to cover 10 GHz mode hop free continuous tuning using the phase section of the laser only. We would have to ensure that the laser is mode hop free over 5 mA.

Phase detectors relying on double balanced mixers or XOR gates have both positive and negative gain over a 0 to π and π to 2π phase difference respectively. Hence, they can automatically phase lock in feedback. PFDs on the other hand have monotonic gain over a 4π phase difference. Thus, in addition to ensuring that the laser tuning is mode hop free in our sampling window, the PFD polarity requires appropriate setting as well.

We can best demonstrate the appropriate polarity selection with an example. Let's qualitatively examine the transient behaviors for a sample slave laser wavelength shift from 1 GHz to 2 GHz offset from the master laser at wavelengths that are greater than the absorption line to which the master laser is locked to. Current injection into the laser phase section results in a blue shift in the wavelength due to free carrier absorption. We also note that blue shifting the wavelength when the slave laser is at a higher wavelength than the master laser reduces the beat note frequency. We also assume the reference frequency into the PFD is a 100 MHz crystal oscillator. At steady state, the frequencies into the PFD are equal. This is a required condition of phase locking as the phase difference between two signals can only be maintained if the frequencies are equal. Since we are starting with a 1 GHz offset, we know that the divider is set to N = 10, so that the divided offset frequency is equal to the 100 MHz reference at the PFD. Because the steady state frequencies will be equal at the PFD when the offset is switched to 2 GHz, we know that this step change in the offset frequency can be accomplished by programming the divider to N = 20. Shifting to this greater offset frequency for wavelengths greater than the master laser requires reduction in current injected into the laser phase section. This requires a positive voltage shift on the modulation control input of the current driver. Sourcing current from the charge pump into the loop filter charges the op-amp feedback capacitor. This lowers the output level as the op-amp attempts to maintain the input levels to its differential terminals equal. The converse is true if the charge pump sinks current.

Because the shift does not happen instantaneously, momentarily the comparison frequency at the PFD becomes 1 GHz / 20 = 50 MHz. For a positive polarity setting, the PFD mostly enables the charge pump sourcing current when the phase accumulation or frequency is greater on its reference input, and the sinking current source when the accumulation is greater on the comparison input. Thus, a negative polarity is suitable for offset frequency locking the slave laser at wavelengths that are greater than that of the master laser due to the negative tuning efficiency of the modulation input on the phase section current source. A similar argument shows that a positive polarity is suitable for frequency offsets that are at wavelengths below the master laser.

Once the laser is locked, the beat note between the master laser and slave laser is amplified and fed into a frequency counter. Like before, we set the gate time to 1 second and measure the changes in frequency over a 1-hour period. Fig. 5.8 compares the offset frequency between the locked master and slave lasers when the two are offset phase locked with an OPLL programmed at a 2 GHz offset and when the slave laser is free running. Note that approximately 25 minutes after leaving the lab do the conditions in the free running case settle.

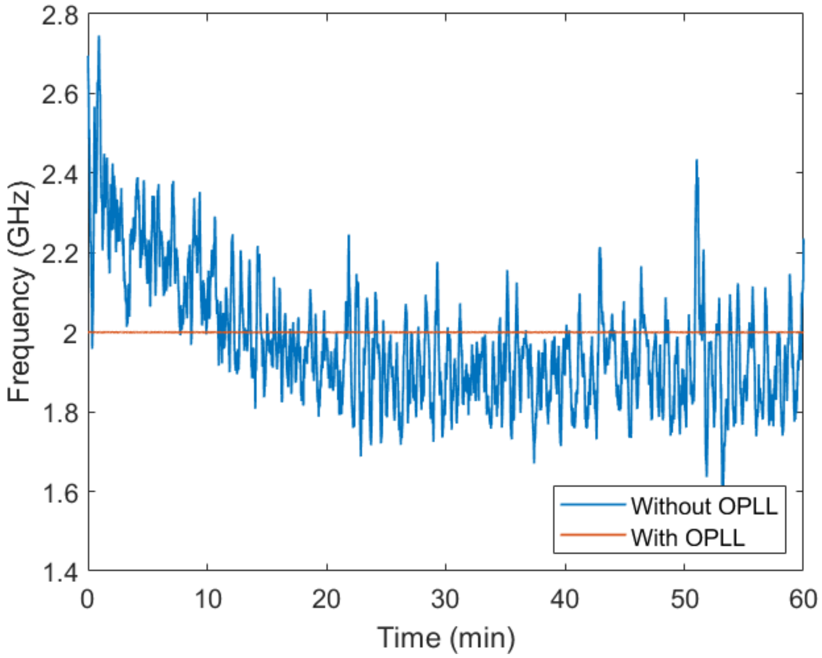

Figure 5.8 Master-slave beat note with the slave laser free running and locked at 2 GHz offset using the OPLL.

Over a 1-hour period the frequency standard deviation improved from 162 MHz to 37.6 kHz. Peak-to-peak deviations also improved from 1.23 GHz to 295 kHz. The mean frequency offset from the master laser was measured to be 1.999911243 GHz. The degradation in performance of the slave laser compared to that of the master laser can be attributed to limited loop bandwidths, optical feedback from fibers and defective PIC components, and broad linewidths of the lasers, even after locking to the cell. Long path delays in the test setup and noise from other sources in the lab, such as supplies and cables, also degrade the performance. Coupling from the phase modulator driver onto the master laser generates a beat note with strong sidebands at the 125 MHz modulation frequency but because the OPLL follows slow frequency excursions, it is possible that even after dividing the beat note frequency down, the frequency modulation is low pass filtered by the narrow feedback loop bandwidth and is expected to be averaged out , although this may be a problem over shorter averaging times. A larger loop bandwidth can help improve performance as long as the signal path lengths are appropriately reduced. Better isolation of devices and shielding can help reduce spurious effects and noise as well.

Using commercially available PLL chips we were able to show offset phase locking at offsets ranging from 1 to 15 GHz. Overlapped spectra of the slave laser at various offsets is demonstrated in Fig. 5.9 which also overlaps the master laser spectrum locked to the absorption line at 1572.335 nm.

Finally, Fig. 5.10 shows the master-slave beat note at 4 GHz. The spurious contents at ± 75 MHz is due to optical feedback from the fiber coupling. It was extremely critical to minimize these to obtain good frequency locking. Note that due to the OPLL narrowband response, this beat note is representative of double the linewidth of our SG-DBR lasers. Close inspection shows the FWHM of the lasers was ~ 3 MHz.

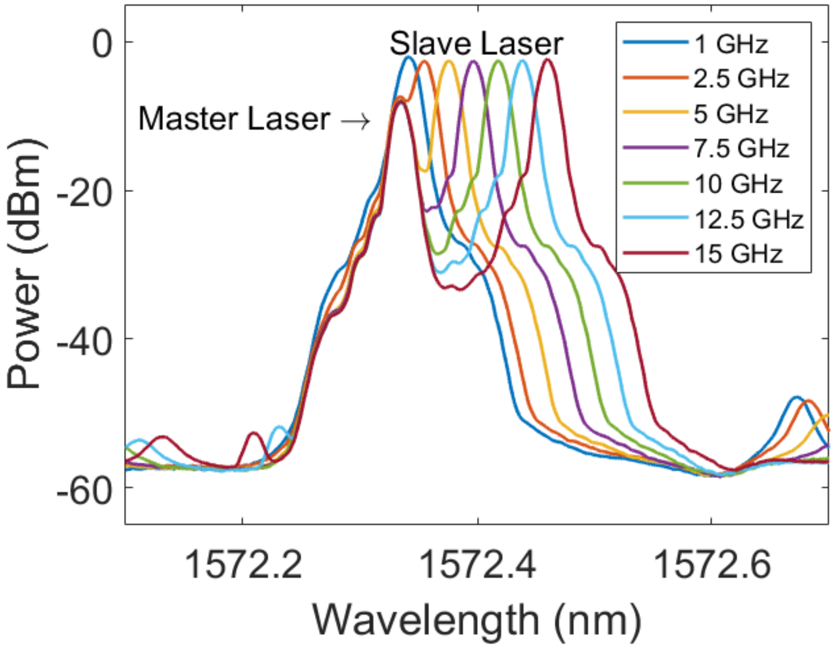

Figure 5.9 Master laser spectrum and overlapped slave laser spectrum locked at various frequency offsets.

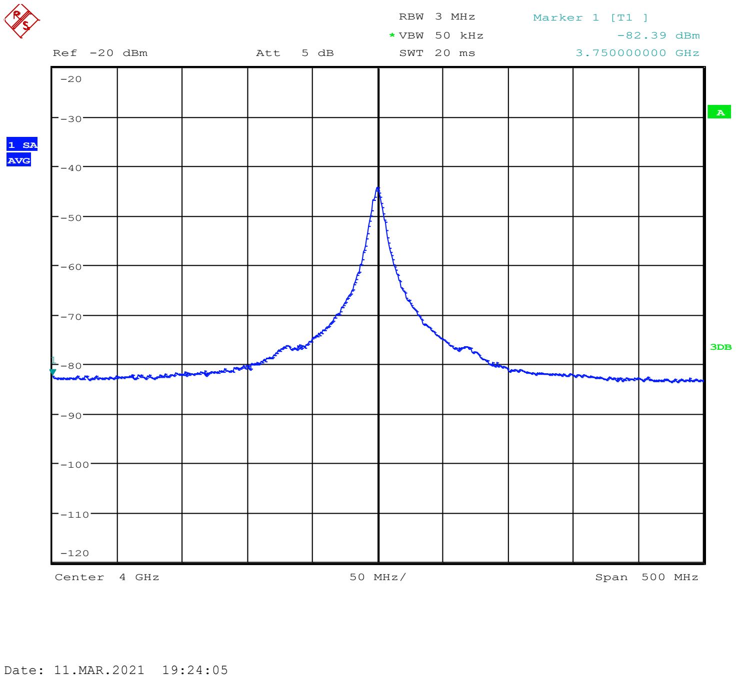

Figure 5.10 Master-slave beat note for 4 GHz offset.

5.4 Pulse Generation

The final subsystem measurements involve characterization of the 1 µs pulses. In the lab these are obtained using a pulsed current source. Direct modulation of an SOA from 0-100 mA with a pulsed current source results in strong overshoot in the optical pulse. As much as 50% was observed. To reduce the overshoot a 40 Ω resistor is placed in series with the current source [6]. This significantly slows down the pulse edges. Rise and fall times were 262 and 169 ns respectively but it is acceptable in our application. Faster responses are expected with electronic integration. For atmospheric applications an EDFA would have to follow the PIC to reach peak pulse powers of 2.5 kW. The slower pulse edge should help generate a more even pulse at the EDFA output. The extinction ratio of the pulse was evaluated at DC with power meters and an OSA. Even at 0 mA bias, the absorption is strong enough to meet the 40 dB extinction ratio requirement.

The significant current drive into the SOA also begs the question as to whether there is any electromagnetic coupling from the SOA onto the laser and the corresponding transient response which can affect the system performance. Similarly, optical effects in the SOA can lead to chirping of the laser wavelength which could be problematic as well if the amplifier is in saturation. In the lab environment both effects would have to be studied carefully using GSG probes. Within a circuit board, proper shielding would have to be implemented. SOA switching that is significantly faster than 1 µs has been demonstrated [7].

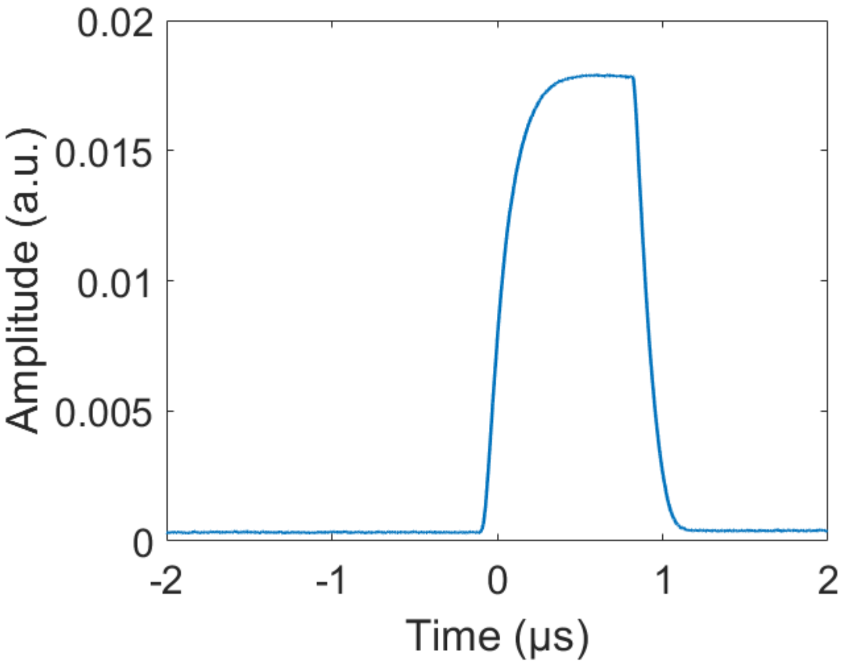

Figure 5.11 Detected pulse from the PIC.

References

1. Bjorklund, G. C., Levenson, M. D., Lenth, W., & Ortiz, C. (1983). Frequency modulation (FM) spectroscopy - Theory of lineshapes and signal-to-noise analysis. *Applied Physics B Photophysics and Laser Chemistry*, *32*(3), 145–152. https://doi.org/10.1007/BF00688820.
2. Supplee, J. M., Whittaker, E. A., & Lenth, W. (1994). Theoretical description of frequency modulation and wavelength modulation spectroscopy. *Applied Optics*, *33*(27), 6294. https://doi.org/10.1364/ao.33.006294.
3. Black, E. D. (2001). An introduction to Pound–Drever–Hall laser frequency stabilization. *American Journal of Physics*, *69*(1), 79–87. https://doi.org/10.1119/1.1286663.
4. Rubiola, Enrico., et al. Phase Noise and Frequency Stability in Oscillators.
5. Numata, K., Chen, J. R., & Wu, S. T. (2012). Precision and fast wavelength tuning of a dynamically phase-locked widely-tunable laser. *Optics Express*, *20*(13), 14234. https://doi.org/10.1364/oe.20.014234.
6. ILX Lightwave. *Tuning the LDP-3840B for the Optimum Pulse Response. https://www.newport.com/medias/sys_master/images/images/h5a/hcb/8797289283614/TN-3840-2-Tuning-the-LDP-3840B-for-Optimum-Pulse-Response.pdf.*
7. Agrawal, G. P., & Olsson, N. A. (1989). Self-Phase Modulation and Spectral Broadening of Optical Pulses in Semiconductor Laser Amplifiers. *IEEE Journal of Quantum Electronics*, *25*(11), 2297–2306. https://doi.org/10.1109/3.42059

Chapter 6. System Measurements

6.1 Power Consumption

PICs require accurate and precise thermal control. This is especially important when operation over a narrow range of frequencies is required. 0.001°C thermal stability is possible using thermoelectric coolers such as the WTC3243. Careful consideration of the PIC power consumption is required when selecting a thermal solution.

Table 6-1 shows the DC power consumption of various sections of the PIC as well as estimated power consumption for the on-chip detector which was not used. The total DC power consumption of the PIC is 600 mW. If used, the additional power consumption of the SG-DBR back absorbers need to be considered. The absorbers can be used to maintain expected power levels over extended operation and a variety of temperatures by compensating current injection levels into the gain section. While this adds system complexity it would likely be required to maintain measurement consistency.

PIC Section	Voltage (V)	Current (mA)	Power (mW)
Master Back Mirror	0.897	6.00	5.38
Master Front Mirror	1.185	23.00	27.26
Master Gain	1.718	150	257.7
Master Phase	1.259	8.70	10.95
Slave Back Mirror	0.890	5.20	4.63
Slave Front Mirror	0.173	22.20	3.84
Slave Gain	1.680	150	252
Slave Phase	1.278	10.00	12.78
Phase Modulator	1.012	25.00	25.3
Detector	-1.5	-10	15
Pulse Generator 1% PRF	1.306	100	1.31
Total Power Consumption			616 mW

Table 6-1 DC power consumption of the IPDA PIC.

6.2 IPDA PIC Lidar System Measurements

6.2.1 CW Measurements

It is interesting to note whether there are any significant offsets in the locking points or potentially other sources of systematic noise and errors in the PIC IPDA lidar that can affect its precision and accuracy performance. These would need to be accounted for in post processing.

Good accuracy within a 10's of MHz may be obtained using a wavemeter which was not available. Instead, to study this, the master laser is locked to the reference cell, and the slave laser is offset frequency locked to the master. The slave laser, in CW operation, is directed to a second CO_2 Herriott gas cell for sampling and detection of the 1572.335 nm absorption line. In this test, the gas cell was pressurized to obtain approximately 75% absorption at the peak absorption wavelength. For pressurizing the cell, an ECL tuned to 1572.335 nm was used for simultaneous pressure reading as a functioning pressure meter was not available. Higher pressures broaden the absorption line which when sampled helps resolve line features at greater offsets. In this case the sampling occurs under CW conditions and sample are averaged.

The beat note for OPLL processing is obtained using the back-side output of the master laser and split light from the front-side of the slave laser. The pulse carver is biased at 80 mA for SOA amplification mode and the master laser is stabilized as before. After CW light passes through the gas cell, it is photo detected and digitized on a sampling oscilloscope. The mean of 1000 samples over 100 µsec is reported at programmed frequency offsets of ± 1, ± 1.2, ± 1.5, ± 2, ± 2.5, ± 4, ± 8 GHz. The detected cell output power results are shown in Fig. 6.1. A Lorentzian fit is also plotted. The full width half maximum of the fit is approximately 1.6 GHz and the absorption peak is close to 75%, which matches well with expectations, although no in depth data processing was performed.

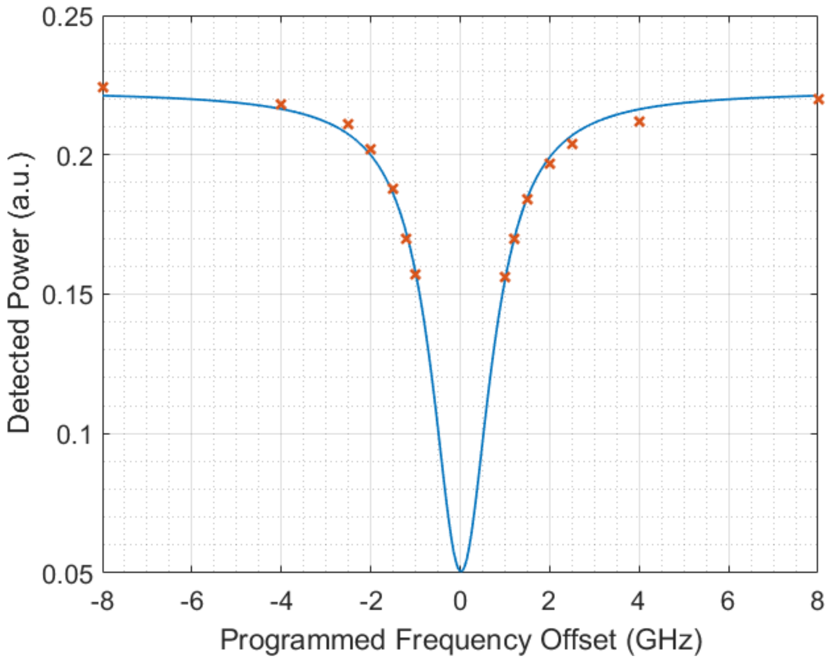

Figure 6.1 Detected CW cell output power measurements of CO_2 gas at 1572.335 nm with Lorentzian fit.

It is clear from Fig. 6.1 that the detected power is greater at negative frequency offsets. Negative offsets correspond to wavelengths that are longer than the absorption line peak. This change in absorption can be due to offsets in the frequency locking point of the master laser or differences in output power of the slave laser as it is tuned, possibly due to free carrier absorption losses in the laser phase section. Because this variation in power is visible over a continuous sweep in the absorption line, as demonstrated in Fig. 6.2, it is likely that the variation in power at equal positive and negative programmed offsets is dominated by the output power variation into the gas cell from the PIC slave SG-DBR. This is also verified by studying the detected power at significant offsets from the absorption line with an ECL which shows that the power at both tails is much closer than that obtained with the slave SG-DBR.

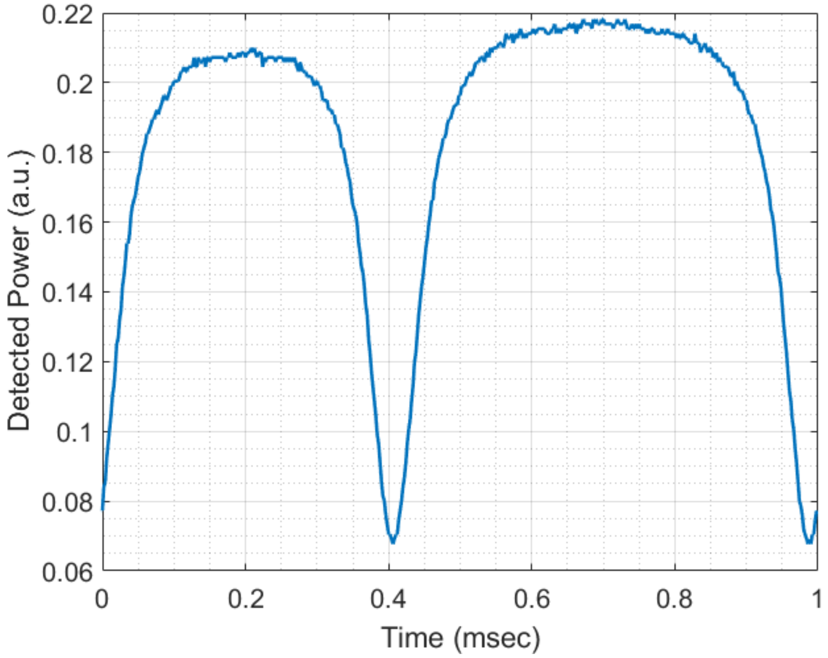

Figure 6.2 Gas cell detected power obtained with continuous sweep of the SG-DBR slave laser.

Such systematic errors can be addressed in post processing by concurrently measuring the input power into the gas cell. Another option would be to level the power using an SOA. With SOAs, facet reflections are a concern and can lead to reduced predictability in the tuning characteristics of the SG-DBR slave laser.

6.2.2 Pulse Measurements

Pulsed measurements can be performed using a setup similar to that for CW measurements, except that the OPLL beat note is generated using the back-side output of both the master and slave lasers. A lensed fiber used for the slave laser front side output is directly fiber connected to the gas cell.

Pulse measurements can illuminate on transient effects that do not surface during CW measurements. For example, the pulses can generate new systematic sources of noise due to electromagnetic interference coupling from the pulse generator to the laser. The pulse generator is stepped in current from 0 to 100 mA. The pulsed source is specified to have fast edges with less than 50 ns rise and fall times. Coupling was indeed a problem in the bench-top setup as frequency measurements of the stability degraded. This interference can be reduced using GSG probes in the lab and would have to be addressed in the packaging and electronic design.

In an attempt to perform pulsed measurements, it had also resurfaced that the gas cell detector bandwidth limited the acquisition of the fast edges and the electronic circuitry filtered out slower components of the pulse from the AC output of the CO_2 detector circuit. Thus, the high-speed output from the electronic detection circuitry showed up-spikes on the rising pulse edge followed by fast decay and down-spikes on the pulse falling edge, also followed by fast decay according to circuit time constants. Strong coupling also degraded the performance of the relative frequencies between the master and slave lasers. This was verified using laser stability measurements such as in Ch. 5.3 and showed that frequency of the beat note was significantly degraded.

To at the very least obtain pulsed measurements in any form, the pulses had to be extended to 100 µsec to utilize the DC output of the gas cell detector PCB. Fig. 6.3 shows pulse measurements at different frequency offsets. Each pulse is averaged 128 times to help settle fluctuation in the output intensity.

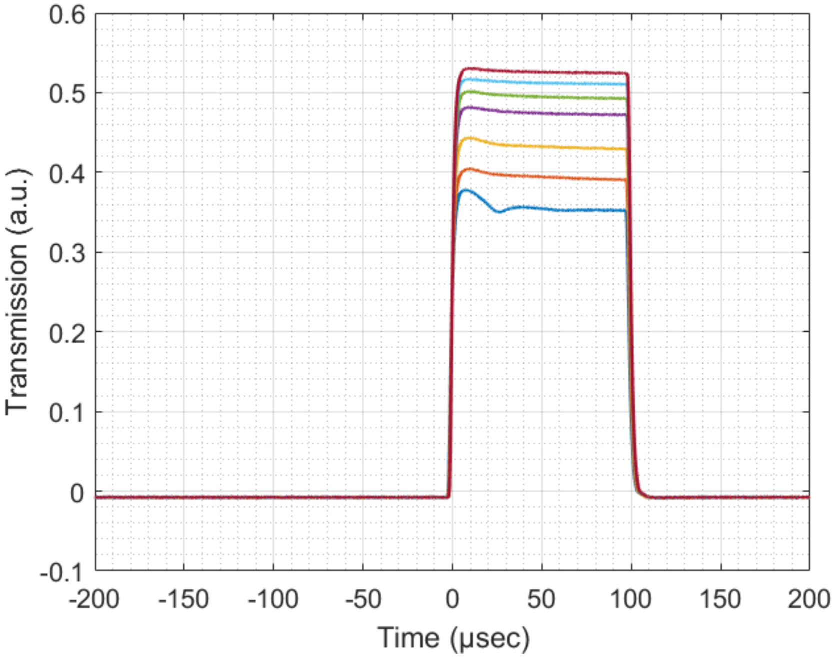

Figure 6.3 Extended pulse measurements at different offset frequencies.

While we cannot obtain short pulses due to limitations in the gas cell detection hardware, there are a few interesting lessons hidden in Fig. 6.3. First, as the pulse transients settle, the average value of each pulse looks very similar to that obtained using CW measurements. This is expected as the behavior appears more and more like a CW measurement as the pulse length is extended. Second, the transient responses at the beginning of the pulse shows that there is a strong chirp in the slave laser frequency, most likely due to electromagnetic coupling on the probe and carrier. We can conclude this because the transient response of pulses at weak transmissions appear to have much greater peak-to-peak deviations than do those for large frequency offsets and strong transmissions. Because these deviations correspond to changes in transmission intensity, they are much stronger closer to the absorption line at offsets of less than 2 GHz, after which the line tapers off much more slowly. The distinctions are most notable when the maximum and minimum transmissions are compared. At higher offsets the changes in transmission are weak functions of frequency and so the pulses are fairly flat. These results stress the importance of good packaging and electronic design. Using proper detection hardware with appropriate bandwidths, one can use this setup to see whether actual transients from SOA chirp and electromagnetic coupling are a significant portion of the pulse width. In such an instance an MZM may be more appropriate for pulse carving, although a single MZM in indium phosphide platforms is insufficient to obtain the required 40 dB extinction ratio. SOAs have nevertheless been used to generate very fast pulses, even under a ns [1].

6.2.3 Frequency Switching Transient Response

It is important to ensure that a step in the OPLL offset frequency settles properly before a pulse is transmitted by the IPDA lidar. Studying the transient of the frequency step response is possible by sending a trigger signal to a frequency counter shortly before a pulse is transmitted. The frequency counter can be set to a gate time that is a small fraction of the time between pulse transmissions. 1-10 μsec gate times are sufficient. A plot of the measured frequency versus time can then be generated before and after the frequency switching command.

Unfortunately, a graphical user interface developed by the vendor was used for programming the OPLL. Consequently, it was not possible to time the counter measurement start time with the change in OPLL offset frequency.

Instead a more direct approach for measuring the transient response was used. Instead of measuring the frequency change with a frequency counter, the modulation voltage on the V-to-I converter was measured on an oscilloscope. A significant change on the modulation voltage, as would be the case for a frequency step, can be captured with an appropriate trigger level and edge type setting. The modulation voltage sampling was done using a simple inverting operational amplifier circuit with high input impedance to minimize disturbances to the original circuit. To improve the resolution of the measurement, a DC bias was subtracted from the initial offset setting at 2 GHz so that the response on the oscilloscope would switch from approximately 0V to its new value. Therefore, the plots in Fig. 6.4 show the change in voltage across the modulation input rather than the actual value. Fig. 6.4 shows the transient response using this technique for several targeted loop bandwidths and phase margins for a frequency switch from 2 to 4 GHz. Note that the horizontal time scales are different.

We can see that changing the loop bandwidth from 250 kHz to 500 kHz while maintaining a 60° phase margin improved the transient settling time from 600 µsec to 125 µsec. It is important to note that the loop bandwidth in this context refers to the frequency at which the loop gain is equal to 1. Increasing the phase margin and reducing the loop bandwidth results in significant slowdowns, as expected.

While the 500 kHz loop bandwidth circuit settles in less than 130 µsec, much faster settling time is required to ensure that the IPDA system can switch frequencies and comfortably settle before a pulse is transmitted. A much more significant switch in offset frequency would not have met system requirements. Far faster settling times are possible using large loop bandwidths. This would be possible with proper electronic feedback circuit design and significantly shorter path delays. Reported loop bandwidths exceeded 600 MHz in previous works. This would easily meet the frequency settling time requirements for the IPDA application. It is important to note that PFD reference inputs are typically limited to ~ 100-200 MHz. To ensure that spurious content from the PFD is adequately attenuated so that the laser is not frequency modulated by spuroius, the loop bandwidth should be limited to ~ 10-20 MHz. The OPLL PFD in our work was limited to 250 MHz.

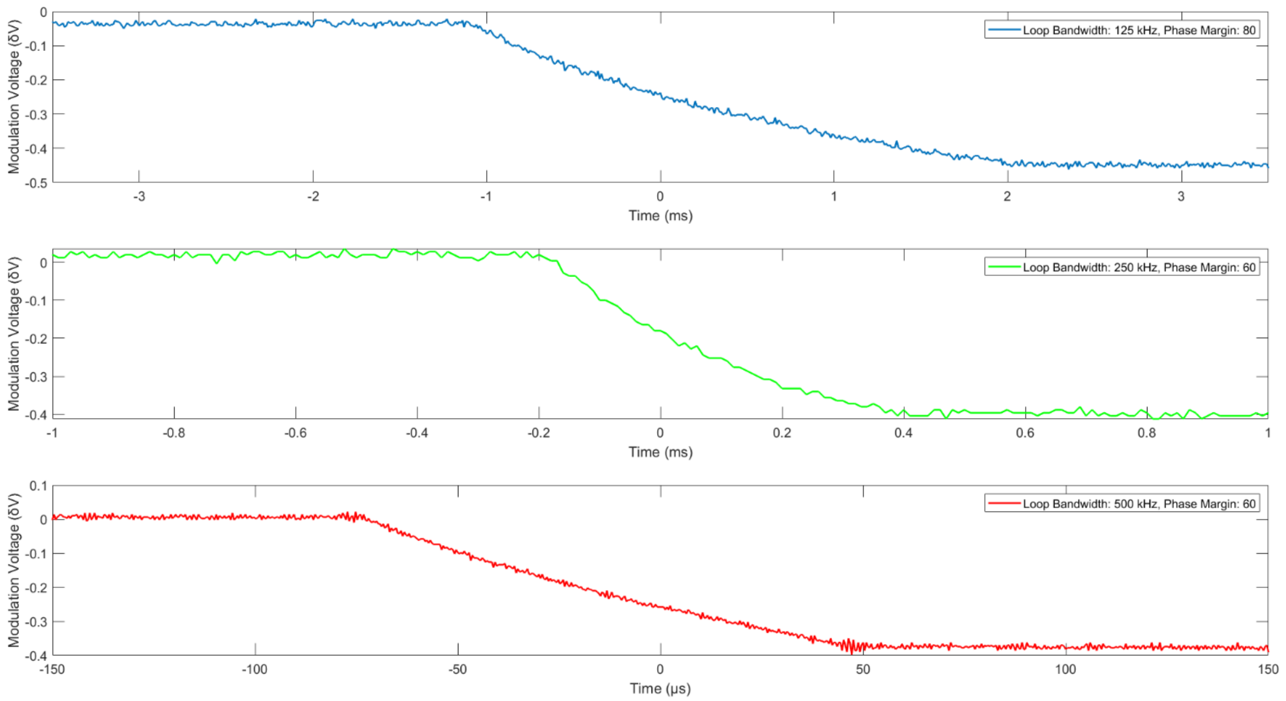

Figure 6.4 Offset frequency step response using OPLL for 2 to 4 GHz step.

6.3 Comparison to NASA IPDA Concept for the ASCENDS Mission

It is worth closely examining the specifications set forth in the ASCENDS mission and the measurements performed to illustrate how those specifications were met by the NASA developed IPDA lidar. The key specifications include the frequency accuracy and precision of the master and slave lasers' absolute frequency, the switching speed between required frequency jumps, and the pulse extinction ratio.

The measurement error budget limited the frequency stability of the lasers to a standard deviation less than 0.23 MHz. While this has been relaxed over time, we will examine how this specification was verified in measurement. First, the frequency stabilities of the free-running and locked absolute and offset frequencies were measured using Allan deviation with a frequency counter. The results are plotted in Fig. 6.5. The main takeaways from this plot are the over ~1000 factor of improvement in the frequency stability for 1 s gate times. The fractional Allan deviation was below 10^{-10} in this case. For gate times of 10 μs and longer, the slave laser stability represented that of the master laser. 10 μs also represents the inverse of the open loop bandwidth. Finally, the offset frequency deviations decreased with increasing gate times, showing that the slave laser deviations were not influenced by the performance of the OPLL but rather represented those deviations of the master laser.

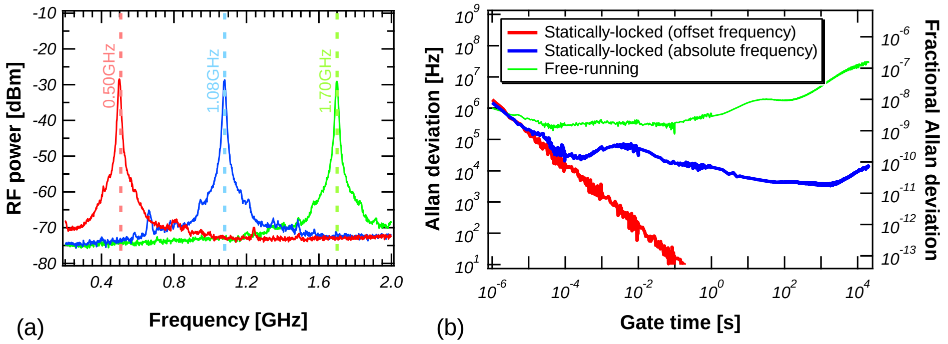

Figure 6.5 Beat notes and Allan variance measurements for NASA IPDA lidar. Reprinted with permission from [1].

For 1 µs pulses that are transmitted periodically every ~ 100 µs, the Allan variance is not the best indicator of absolute frequency stability. If multiple pulses are required to average the frequency standard deviation down to the specified 0.23 MHz limit, then it is important to account for sources of noise that may limit the frequency stability over longer time scales, perhaps tens to hundreds of milliseconds. This may include systematic sources of noise that may cause frequency drift. The purpose of the Allan variance is to remove such sources of frequency error from the measurement. To reintroduce this bias into the measurement, the frequency standard deviation is preferred. To properly measure the absolute frequency stability over multiple pulses, the frequency was first measured over 1 µs gate times. The average and standard deviations were then obtained for multiple pulses separated by the tuning cycle time of approximately 1 ms. The results are plotted in Fig. 6.6 and they show that for dynamically switched frequencies, a standard deviation of 0.23 MHz was met when at least 60 pulse measurements were averaged. These pulses were taken at the end of the cycle to allow as much time as possible for the laser frequency to settle. Furthermore, the standard deviation falls as $1/\sqrt{n}$, indicating that the errors in the frequency measurements were due to uncorrelated white frequency noise.

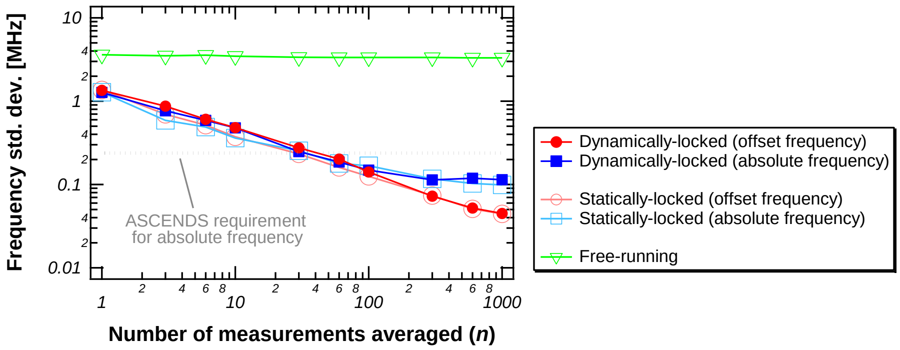

Figure 6.6 Frequency standard deviation of the laser over averaged 1 μs pulses. Reprinted with permission from [1].

Fast switching is required to ensure that the laser frequency has settled to its static level before a pulse is transmitted for sampling of CO_2. Using a DS-DBR laser, the NASA IPDA lidar managed to obtain a frequency switching time of less than 40 μs. The largest hop was 32 GHz and correspondingly had the longest switching time. The fast switching was accomplished using a feedforward signal into the phase section of the DS-DBR, likely based on a look-up-table, and a programmable OPLL. Fast programming was possible and required only 1 μs. Considering the large frequency jumps, the combined feedforward and feedback signals significantly improved the settling times based on reported loop bandwidths (~100 kHz). Because of the large mode-hop free tuning range, feedforward signals were not applied to the front or rear mirrors but would be required for an SG-DBR. Fig. 6.7 shows the frequencies, feedforward, and feedback signals, and programmed offset frequencies. The frequency offsets were monitored using frequency counters. Fig. 6.8 shows close-ups of the smallest and largest frequency jumps. Much more overshoot is visible for the largest frequency jump.

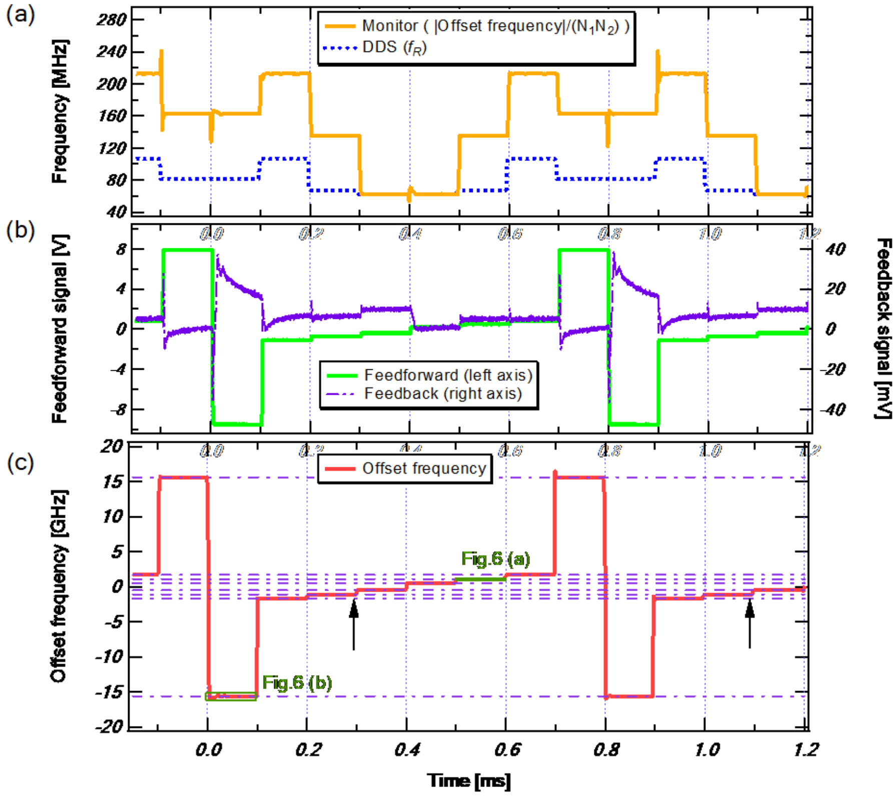

Figure 6.7 Timing responses of feed forward and feedback signals for different frequency steps. Reprinted with permission from [1].

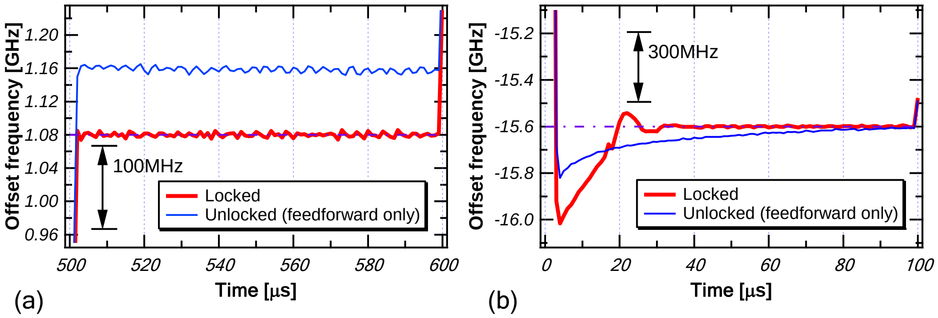

Figure 6.8 Close up of smallest and largest offset frequency switch. Reprinted with permission from [1].

The PIC lidar tested in the lab unfortunately falls short of these specifications but there is much room for improvement. As was demonstrated in Ch. 6.2.3 the best switching time obtained in the lab for a frequency switch from 2 to 4 GHz was 125 µs. The switching time can be improved using much greater loop bandwidths which are possible with integration or by implementation of a switching scheme that utilizes both feedforward and feedback signals into the phase section. The first was not implemented in the lab because of large loop delays in the setup while the latter was not implemented due to the complexity. It is therefore expected that these specifications can be met in future implementations.

Pulse switching in the lab showed degradation in the frequency stability of the PIC. This was identified with a frequency counter during pulse transmission. The degradation in frequency stability is most likely due to poor selection of probes. Network measurements performed to study the coupling between individual probes on the same probe card indicated unintentional coupling of signals onto adjacent traces. In the lab, improvements can be made by using probe cards with GSG connectors on each individual probe. Filtering and matching where possible and better isolation between devices should also help as well. The extinction ratio of the pulses met specifications and the rise and fall times were acceptable as well.

Another area of concern is in the frequency stability of the PIC lidar over short time scales. When the frequency of transmitted pulses was averaged, no reduction in the standard deviation was demonstrated as in Fig. 6.6 over multiple pulses. This can potentially be due to narrow loop bandwidths and consequently the loops are incapable of suppressing strong noise components that are relevant along the time scales of interest. Strong optical feedback may also be a problem. Isolators help reduce feedback from reflections off detector facets although reflections from the lensed fiber still perturb the laser frequency. Backing off from the PIC helps reduce this effect but good packaging of the micro optics is essential. Significant noise pick-up in the lab may also be a problem as well as optical feedback due to defective PIC devices.

References

1. Numata, K., Chen, J. R., & Wu, S. T. (2012). Precision and fast wavelength tuning of a dynamically phase-locked widely-tunable laser. *Optics Express*, *20*(13), 14234. https://doi.org/10.1364/oe.20.014234.

Chapter 7. Summary and Future Work

PICs allow integration of complex optical systems onto a small chip. Integrated functions include lasing, detection, modulation, and amplification. Furthermore, a variety of material platforms, integration techniques, and properties are available that can enable a broad range of applications ranging from quantum and optical communications, computing, sensing and lidar, and metrology. There is seemingly a never-ending list of applications where photonics can offer drastic improvements over conventional techniques and generate brand new technological sectors as well. Why hasn't photonics proliferated in every technological sector known to man? Perhaps the most serious obstacle is that not all photonics material platforms support monolithic integration of a laser, including silicon. This requires externally packaged or co-packaged lasers which raises costs. Other options include hybrid silicon lasers using wafer bonding, heterogenous integration, and heteroepitaxy [1]. The future appears to be bright as much progress has been made in these areas and there is broad recognition that photonics is required to transition from costly bulky optical systems to low C-SWaP photonic substitutes.

7.1 Summary

In this work we developed an IPDA lidar on chip for active sensing of CO_2. First, techniques for laser stabilization were covered. We relied on the frequency modulation technique to stabilize our master laser using an integrated phase modulator. A discussion on design of optical frequency and phase locked loops with actual examples followed. The laser was stabilized to a reference gas cell. Measurements showed more than two orders of magnitude improvement in the master laser stability for 1-second gate times. We also demonstrated locking of the slave laser to the master laser at offsets up to 15 GHz using the OPLL. In this work we relied on off-chip photodetectors for detection of the master-slave beat note. This added significant complexity since more PIC outputs were required for the complete system to work, further emphasizing the advantage of full PIC integration. The slave laser overall stability at an offset of 2 GHz followed the master laser closely. The beat note stability of the two locked lasers was ~300 kHz for 1 second gate times. Finally, an SOA was used to carve out 1 μs pulses with very high extinction ratio. Using this PIC, gas sensing of CO_2 was performed. The setup made use of a second gas cell that was pressurized to ~ 75% peak absorption. After locking the master laser, the slave laser was offset locked at several sampling points on both sides of the absorption line up to 8 GHz for line mapping. A Lorentzian fit to the data showed peak absorptions that matched up well with expectations, although no strict analysis was performed. Instead, this work showed that there were no significant sources of systematic error in the locking frequency due to RAM. Other sources of error, such as variations in output power, can be addressed in post processing or addressed in future fabrication runs. While not a primary focus, basic tuning measurements using both temperature and current showed that the IPDA PIC can be used over a wide range of temperatures by including slow thermal control in the feedback loop.

More work must be done to address shortcomings in the performance of the IPDA PIC lidar. The laser stability was an order of magnitude worse that the lidar developed at NASA Suspected culprits are the narrow loop bandwidths, noise pick-up in the lab, poorly performing probes, and optical feedback off of devices on the PIC, failed devices, and lensed fibers. While pulse generation successfully showed high extinction ratios and acceptable rise and fall times, there were clear indications that the frequency of the slave laser was perturbed. This also may have been due to poorly performing probes. Coupling was detected on adjacent traces using network analysis. To prevent coupling, probes in the lab need to be replaced with GSG probes. Switching speed in the lab was not fast enough to meet specifications either. This is primarily attributed to the limited loop bandwidths but techniques using a combination of feedforward and feedback or greater loop bandwidths should resolve this.

7.2 PIC Assemblies

PIC research at a university is many times limited to optical bench testing. As PIC architectures increase in complexity, more measurement instruments and PIC device drivers such as pattern generators or current sources are needed. As the test setup size increases to accommodate all the necessary equipment so does the length of optical fibers and coaxial cables, and the number of optical and microwave adapters that connect everything together. These add additional sources of reflections, delays, and noise into the measurement setup. Noise due to electromagnetic interference, thermal fluctuations, and mechanical vibrations impact the system test setup and degrade the overall performance of the PIC and measurement results as well. Furthermore, lab equipment is not always optimally suited to drive PIC devices. This can also limit PIC device and system performance.

Packaging the PIC, and careful microwave and thermal design can help. It also allows placement on a PCB and furthermore, circuit designers have access to electronic integrated circuits and components that offer far more flexibility and capabilities than are possible in the lab.

Figure 7.1 shows a prototyping assembly constructed for the IPDA PIC. It includes master and slave laser driver printed circuit boards (PCBs) with thermal control. The current sources were controlled digitally. The phase section drivers also had modulation inputs for interfacing with servo PCBs not shown, and a commercial evaluation board was used for the PLL. Also included was a PCB for high-speed beat note detection. Biasing for this board was provided from beneath the assembly. Interfaces for external equipment was also available to drive the phase modulator and pulse carver. A custom carrier contained the PIC and thermistor. The carrier was then wire bonded to the different PCBs. A thermo electric cooler (TEC) beneath the carrier was used to manage the its temperature.

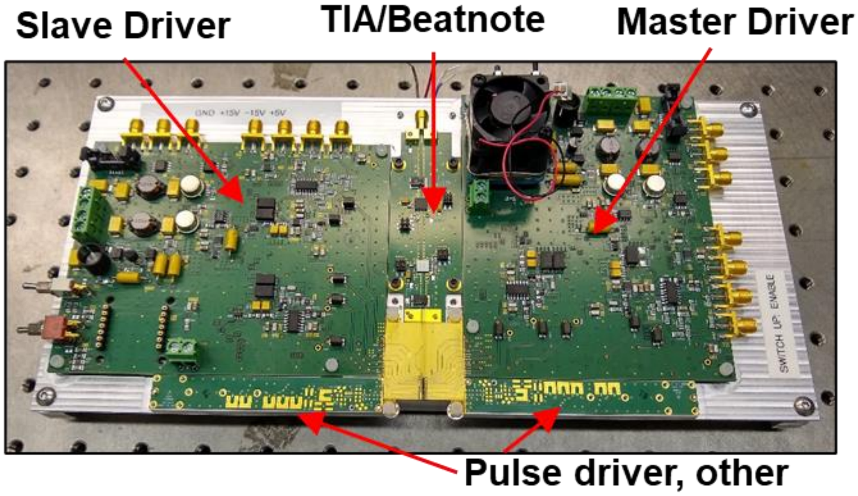

Figure 7.1 IPDA PIC prototyping assembly.

PICs can benefit tremendously from closely placed integrated electronic circuits and packaging. While the prototyping assembly in Fig. 7 was customized for our application, a modular assembly can be constructed in the lab to help overcome lab setup difficulties and can serve as a prototyping platform for a variety of sensitive PICs by simply swapping modular circuits in and out of the platform. For example, one can design a low noise current source PCB block which can be mounted beside the PIC on the assembly platform and wire bonded to the PIC carrier. As the number of circuits grows, and consequently more space would be required, the PCB block can be placed further away. Multi-trace blocks containing multiple traces can then bring the signals to the carriers. Such a PIC prototyping platform can be a powerful tool for test and measurement and also provide a pathway towards compact low C-SWaP PIC module design.

Without monolithic electronic integration beside the photonics, optical control microcontrollers available on the market are instrumental in PIC module miniaturization efforts. These are capable of sourcing current to multiple PIC diodes and have many DACs and ADCs for DSP and interacting with the analog world. If appropriate for the application, PICs and optical microcontrollers can provide significant reduction is C-SWaP.

7.3 A Word on Transimpedance Amplifiers and MMICs

Clever workarounds are required for beat note detection when a conductive substrate is used. In the assembly system that was developed for PIC prototyping, a transimpedance amplifier (TIA) is used to amplify the master-slave beat note which is then processed by the OPLL. The commercial-off-the-shelf (COTS) HMC6590 43 Gbps TIA was selected to amplify the beat note. The HMC6590 was perhaps the only TIA available that met bandwidth requirements and was sold by common electronics suppliers such as digikey. In addition to offering high bandwidth, the HMC6590 has a limiting amplifier and buffer, a differential output to help reduce common mode noise, and a differential swing of 450 mVpp, which is sufficient for directly driving common COTS PLL electronic integrated circuit RF inputs. It furthermore has an input optical sensitivity of -10.5 dBm. Appropriate power budgeting estimates were performed to determine the splitting ratios from the master and slave lasers to meet these requirements. Finally, the TIA is powered by a 3.3V supply which the chip also makes available for reverse biasing the detector through a 50 Ω resistor/capacitor network.

The waveguide PIC detectors rely on electro-optical absorption of light and the responsivity is improved in reverse bias. A basic illustration of a TIA circuit is provided in Fig. 7.1.

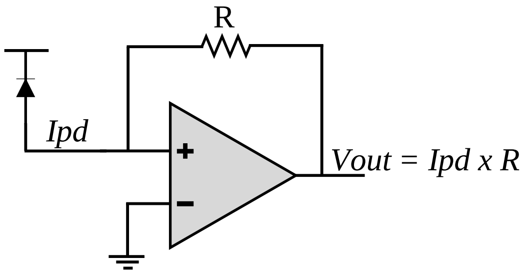

Figure 7.1 Basic transimpedance amplifier circuit.

Many TIAs, such as the HMC6590, require a single 3.3V or similar supply. Internally to the TIA chip, an input DC voltage is typically generated which needs to be considered for reverse biasing of the detector. The HMC6590 generates a 1.2V input voltage which is connected to the detector anode.

In our PIC design we utilized a conductive substrate. Without proper grounding techniques, the TIA circuit would be obsolete, requiring other methods of beat note amplification. The problem and remedy are illustrated in Fig. 7.2.

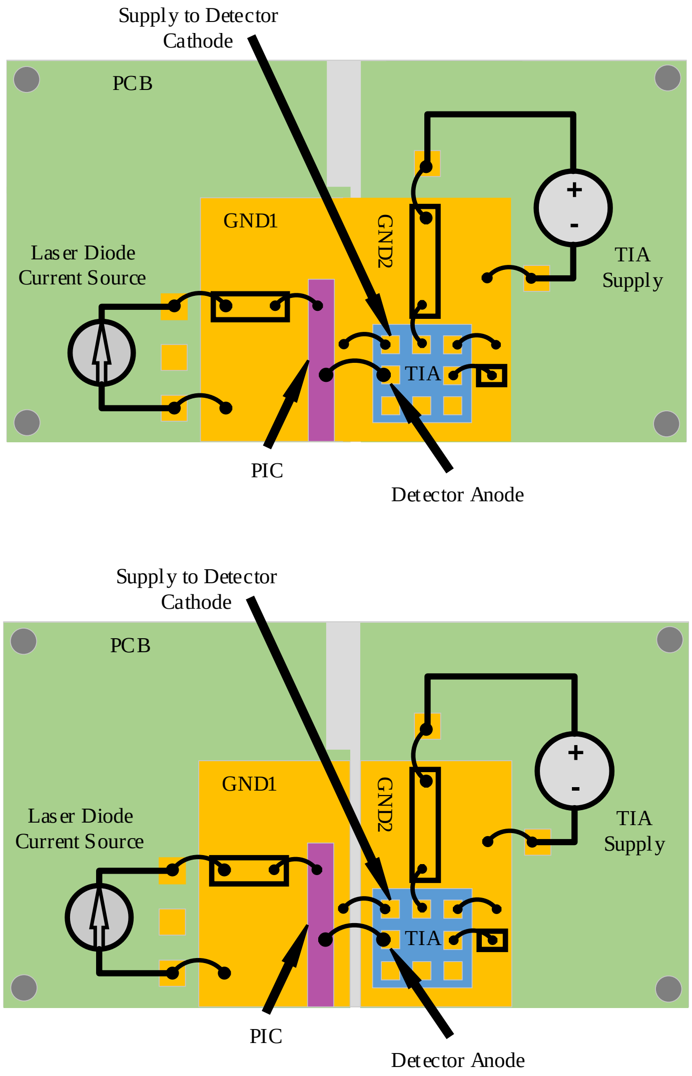

Figure 7.2 Improper and proper grounding techniques for detectors integrated on a conductive substrate with use of a TIA.

In the first configuration, GND1 and GND2 are electrically shorted together. The TIA that is mounted beside the PIC provides the supply to the detector cathode for reverse bias. The detector anode is bonded to the TIA input. The detector cathode is shorted to the conductive substrate which happens to be electrically connected to the same ground as the TIA. Consequently, the TIA supply output is shorted to TIA ground and the circuit will not work. Also, since the single ended input to the TIA is set positive, the detector would be forward biased, and no beat note is detected. This is hypothetical as a TIA with supply shorted to ground would not work in the first place.

This problem is remedied by electrically insulating the PIC and TIA grounds. Current sources connected to laser sections can share GND1 since currents flowing into PIC diode anodes return to their current supply through GND1. This is Kirchhoff's current law. In this configuration, the TIA supply output is electrically is connected to GND1 using a wire bond and insulated from GND 2, thus preventing the short from the first scenario. As far as the TIA circuit is concerned, the entire GND1 plane is set to the supply for reverse biasing of the PIC detector. The current sources for the other PIC sections simply operate relative to this potential and so the connection to the TIA supply output is irrelevant. The detector anode is connected to the TIA input. Any current detected is delivered to the input from the TIA supply since none of that current can flow through the other circuit paths. Instead of a TIA, MMIC amplifiers can be used in a configuration where the PIC and MMIC share grounds. A bias-T is required to reverse bias the detector. This technique is less efficient at extracting detector signals and may be susceptible to instabilities as the detector is not matched to the amplifier.

7.4 Future Work

The IPDA PIC lidar has much room for improvement and optimization and requires additional investigation as well. For example, does pulsing the slave laser with an SOA perturb the stability of the slave laser? Electromagnetic effects and optical chirping may be culprits that need to be addressed using shielding techniques or substitution with other photonic devices. How is the stability affected by other systematic sources of noise, such as electromagnetic coupling from the phase modulator? What effect does the strong thermal crosstalk have on the stability of the lasers. As much as 0.4 nm shift occurs in the master laser when the slave gain section is turned on and set to 150 mA. Can the performance improve by better isolating the PIC devices or laser sections? This would require additional processing steps. Is individual device thermal control beneficial? Are there significant reflections within the PIC and can these influences be mitigated with device or architectural changes? Answers to these questions can be determined with simulations and sound engineering design. Others may require innovation, scouring through journals for answers, and new research.

The IPDA PIC is rich in complexity. The work done here has opened new windows of opportunity, including research into new photonic device design such as low RAM phase modulators. Furthermore, it is easy to see the appeal of transferring this technology to new wavelengths for investigation of other greenhouse gases. New phase modulators and laser fabrication at 1030 nm is underworks in our research group [2]. Integrated gas cells and atomic cladding waveguides can eliminate the bulkiest component of our IPDA lidar; the Herriott gas cell [3]. External cavity SG-DBR lasers integrated on chip with narrow linewidths can enhance precision and help reduce averaging times. Closely related applications can be pursued, including integrated optical clocks for metrology which require a stable lasing reference [4]. Such sources can also be used for comb generation which can enable complex and precise spectroscopic systems on chip [5]. These applications can be addressed using several material platforms. The significant progress in heterogenous integration, for example, allows large scale production of photonics using the well-established infrastructure of the electronics CMOS industry. The low loss waveguides, process resolution, and repeatability along with high index contrasts in SOI, allows design of advanced sensing technologies using narrow linewidth semiconductor lasers and low loss devices in a compact form factor, and the electronics controls can be integrated bedside the PIC for optimal operation [6].

References

1. M. J. R. Heck *et al*., "Hybrid Silicon Photonic Integrated Circuit Technology," in *IEEE Journal of Selected Topics in Quantum Electronics*, vol. 19, no. 4, pp. 6100117-6100117, July-Aug. 2013, Art no. 6100117, doi: 10.1109/JSTQE.2012.2235413.
2. Integrated Photonics Lab, University of California, Santa Barbara. https://web.ece.ucsb.edu/ipl/
3. Stern, L., Desiatov, B., Goykhman, I. *et al.* Nanoscale light–matter interactions in atomic cladding waveguides. *Nat Commun* **4,** 1548 (2013). https://doi.org/10.1038/ncomms2554
4. Udem, T., Holzwarth, R. & Hänsch, T. Optical frequency metrology. *Nature* **416,** 233–237 (2002). https://doi.org/10.1038/416233a
5. Ian Coddington, Nathan Newbury, and William Swann, "Dual-comb spectroscopy," Optica 3, 414-426 (2016)
6. Tran, M. A., Huang, D., & Bowers, J. E. (2019). Tutorial on narrow linewidth tunable semiconductor lasers using Si/III-V heterogeneous integration. *APL Photonics*, *4*(11). https://doi.org/10.1063/1.5124254